

---

# Methods<sup>1</sup>

---

## Expedition 304/305 Scientists<sup>2</sup>

### Chapter contents

<b>Introduction</b> .....	<b>1</b>
<b>Igneous petrology</b> .....	<b>3</b>
<b>Metamorphic petrology</b> .....	<b>7</b>
<b>Structural geology</b> .....	<b>9</b>
<b>Geochemistry</b> .....	<b>12</b>
<b>Paleomagnetism</b> .....	<b>14</b>
<b>Physical properties</b> .....	<b>16</b>
<b>Microbiology</b> .....	<b>21</b>
<b>Downhole measurements</b> .....	<b>23</b>
<b>References</b> .....	<b>28</b>
<b>Figures</b> .....	<b>31</b>
<b>Tables</b> .....	<b>57</b>

### Introduction

This chapter documents the procedures and methods employed in the various shipboard laboratories during Expeditions 304 and 305 of the Integrated Ocean Drilling Program (IODP). This information applies only to shipboard work described in the Expedition Reports section of the Expedition 304/305 *Proceedings of the Integrated Ocean Drilling Program* volume. Methods for shore-based analysis of Expedition 304 and 305 samples and data will be described in individual scientific contributions to be published elsewhere.

### Authorship

All shipboard scientists contributed to the completion of this volume. The separate sections of the chapters were, however, written by teams of scientists as given below (listed alphabetically):

- Expedition summary: Expedition 304/305 Scientists
- Background and objectives: Blackman, John, Ildefonse, Ohara
- Operations: Grigar, Grout, Midgely, Miller, Storms
- Igneous and mantle petrology: Abe, Andal, Brunelli, Charney, Christie, Hansen, Hellebrand, Ishimaru, Johnson, Maeda, Tamura Hasebe, von der Handt
- Metamorphic/Alteration petrology: Abratis, Andreani, Beard, Delacour, Drouin, Frost, Fryer, McCaig, Nozaka
- Structural geology: Escartin, Grimes, Halfpenny, Hayman, Hirose, Hirth, Michibayashi, Suhr
- Geochemistry: Awaji, Godard, Rosner, Yamasaki
- Paleomagnetism: Gee, Morris, Tominaga, Zhao
- Physical properties: Blackman, Harris, Karner, Searle
- Microbiology: Mason, Nakagawa
- Downhole measurements: Delius, Einaudi, Linek

### Numbering of sites, holes, cores, and samples

Drilling sites are numbered consecutively from the first Deep Sea Drilling Project site drilled by the *Glomar Challenger* in 1968. Starting with IODP Expedition 301, the prefix “U” designates sites occupied by the U.S. Implementing Organization (USIO) vessel. At a site, multiple holes can be drilled by removing the drill pipe from the seafloor, moving the ship a short distance, and then drilling a new hole. For all IODP drill sites, a letter suffix distinguishes each hole drilled at the same site. The first hole drilled is assigned the

<sup>1</sup>Expedition 304/305 Scientists, 2006. Methods. In Blackman, D.K., Ildefonse, B., John, B.E., Ohara, Y., Miller, D.J., MacLeod, C.J., and the Expedition 304/305 Scientists. *Proc. IODP, 304/305: College Station TX (Integrated Ocean Drilling Program Management International, Inc.)*. doi:10.2204/iodp.proc.304305.102.2006  
<sup>2</sup>Expedition 304/305 Scientists' addresses.



site number modified by the suffix “A,” the second hole takes the site number and suffix “B,” and so forth. The cored interval is measured in meters below seafloor (mbsf). The depth below seafloor is determined by subtracting the water depth estimated from the initial drill pipe measurement, which gives the length of pipe from the rig floor to the seafloor (measured in meters below rig floor), from the total drill pipe measurement. While on site, ship location over a hole is maintained with respect to a positioning beacon deployed on the seafloor and in active communication with the Nautrinix dynamic positioning (DP) system on the *JOIDES Resolution*. In general, the primary reference for DP was the Global Positioning System (GPS); the beacon reference acts as a backup in the event that GPS is unreliable.

During most IODP cruises, each cored interval is generally 9.5–9.8 m long, which is the length of a core barrel. However, one potential cause of poor recovery in hard rock coring is core jamming in the bit or the throat of the core barrel. Once the opening in the bit is jammed, core may be prevented from entering the core barrel. During Ocean Drilling Program (ODP) hard rock coring missions, a novel coring approach employed to improve recovery was to extract the core barrel at shorter penetration intervals in order to mitigate loss of core when the bit was blocked. Following this strategy, most cored intervals during Expeditions 304 and 305 were reduced to 4.5–5 m (half cores).

Each recovered core is divided into 1.5 m sections that are numbered serially from the top. When full recovery is achieved, the sections are numbered sequentially as recovered, starting with 1 at the top of the core; the last section may be shorter than 1.5 m (Fig. F1). When the recovered core is shorter than the cored interval, the top of the core is equated with the top of the cored interval (in mbsf) by convention to achieve consistency in handling analytical data derived from the cores. All pieces recovered are placed immediately adjacent to each other in the core tray. Samples and descriptions of the cores are designated by distance, measured in centimeters from the top of the section to the top and bottom of each sample or interval. A full identifier for a sample consists of the following information: expedition, site, hole, core number, core type, section number, piece number (for hard rock), and interval in centimeters measured from the top of section. For example, a sample identification of “304-U1309B-2R-1, 30–32 cm” represents a piece of core removed from the interval between 30 and 32 cm below the top of Section 1, Core 2 (R designates that this core was taken with the rotary core barrel [RCB]) of Hole U1309B from Expedition 304 (Fig. F1).

## Core handling

Most cores recovered during Expeditions 304 and 305 were extracted from the core barrel in plastic liners. These liners were carried from the rig floor to the core processing area on the catwalk outside the core laboratory, where they were split into 1.5 m sections.

Liner caps (blue = top; colorless = bottom) were glued with acetone onto liner sections on the catwalk. The 1.5 m sections were transferred to the core splitting room, where the plastic liners were split lengthwise to expose the core. For cores recovered without plastic liners, core pieces were extracted from the core barrel and placed in consecutive order in a split plastic liner. In either case, pieces of the core were pushed together and the length of the core in each core liner was measured to the nearest centimeter; this measurement was entered into the IODP curation data acquisition program as liner length (LL in the database), and the cores were transferred to the core splitting room.

Nearly all pieces of core were marked on the bottom with a red wax pencil to preserve orientation, either before they were extracted from the core barrel or when they were removed from the split core liner. In some cases, the pieces were too small to be oriented with certainty. Therefore, the red wax mark does not universally indicate that the core piece was oriented. Whole-round samples for microbiology were sampled in the core splitting room prior to any other handling using techniques described in “[Microbiology](#).”

Adjacent core pieces that could be fit along fractures were curated as single pieces. A plastic spacer was secured to the split core liner with acetone between individual pieces and/or reconstructed contiguous groups of pieces. These spacers may represent a substantial interval of no recovery. The length of each section of core, including spacers, was entered into the curation database as the curated length. The curated length will commonly differ by a few centimeters from the liner length measured on the catwalk. Subsequently, the cores were marked by a structural geologist or igneous petrologist to indicate a split line, ideally maximizing the expression of dipping structure on the cut face of the core while maintaining representative lithology in both archive and working halves.

Each section was scanned using the shipboard multi-sensor track (MST) (see “[Nondestructive sample experiments](#)” in “Physical properties”), and the outer cylindrical surfaces of the whole-round pieces were scanned with the IODP digital core scanner, using the split line marking for registration. Each whole-round core was scanned two or three times, with the

core rotated by 180° or 120°, respectively, between each scan. The digital images from these scans can be merged to form an unwrapped image of the surface of the whole-round core.

Each piece of core was then split into archive and working halves, with the positions of plastic spacers between pieces maintained in both halves. Pieces are numbered sequentially from the top of each section beginning with number 1; reconstructed groups of pieces are assigned the same number but are lettered consecutively. Pieces are labeled only on the outer cylindrical surfaces of the core. If the piece is oriented with respect to the way up, an arrow was added to the label pointing to the top of the section.

The archive half of each core was described, and observations were recorded on IODP templates and spreadsheets developed by the shipboard scientific party (for details, see individual disciplinary sections in this chapter). Digital images of the dry cut face of the archive halves were captured with the IODP digital imaging system. Archive-half sections were also passed through the cryogenic magnetometer for magnetic remanence measurements.

Finally, the archive half was photographed using black-and-white and color film. Digital color close-up images were taken of particular features for illustrations in the summary of each site, as requested by individual scientists. The working half of the core was sampled for both shipboard characterization of cores and shore-based microbiological studies. Samples were routinely taken for shipboard physical properties (minicore or ~9 cm<sup>3</sup> cube), paleomagnetic (minicore or ~9 cm<sup>3</sup> cube), thin section (billet or slab), and geochemical analyses (billet or quarter round) as described in the sections below. Each extracted sample was logged into the sampling database program by the location and the name of the investigator receiving the sample or by the type of shipboard sample. Records of all removed samples are kept by the curator at IODP. The extracted samples were sealed in plastic vials, cubes, or bags and labeled.

Following the shipboard initial scientific measurements and sampling, both halves of cores were shrink-wrapped in plastic to prevent rock pieces from moving out of sequence during transit. The working and archive halves of cores were then put into labeled plastic tubes, sealed, and transferred to cold-storage space aboard the drilling vessel. At the end of Expedition 305, the cores from both expeditions were transferred from the ship to cold storage at the IODP Gulf Coast Repository in College Station, Texas (USA). After a joint postcruise sampling party for Expeditions 304 and 305, the cores were

transferred for permanent storage to the IODP repository at the University of Bremen (Germany).

### Hard rock core descriptions

Hard rock petrographic observations made during Expeditions 304 and 305 are stored in both written and electronic media. All descriptions and measurements were made on the archive halves of the cores, except where otherwise noted. A summary of macroscopic features observed in the cores is presented in visual core description (VCD) forms (Fig. F2). In the VCD forms, individual piece numbers are noted along the left-hand side of the core image. In the column labeled Orientation, arrows indicate pieces large enough to be oriented with respect to the top of the core. The location of shipboard samples are noted in the column labeled Shipboard Studies. Complete macroscopic descriptions and measurements are available for each site in spreadsheet form (see “[Supplementary material](#)”). For details on observations recorded in the spreadsheets, the reader is referred to the disciplinary sections in this chapter. Complete microscopic descriptions on petrographic thin sections are available for each site (see “[Core descriptions](#)”).

### Sediment descriptions

A few sediment cores were collected during Expedition 304 in pursuit of our objective of documenting the upper surface of the massif. Because these cores were collected with rotary coring systems, all of them show moderate to pervasive drilling disturbance. For all but the single extended core barrel core, virtually no lithostratigraphy can be determined from these cores, as they are soupy, unconsolidated, drilling-reworked slurry. The sediment components have been described on standard IODP VCD barrel sheets. Only three classes of materials have been distinguished (Fig. F3): calcareous ooze, conglomerate, and basalts. The basalts have more complete descriptions in the hard rock VCD forms. Microbiological samples taken onboard from the sediments are noted in the Sample column with the symbol MB. Colors described are estimated from Munsell color charts.

### Igneous petrology

As during ODP Legs 176 and 209, measurements were performed by the entire igneous petrology team working in tandem. For consistency, qualitative measurements (especially the selection of igneous contacts) were made by the entire team.

Igneous units were defined on the basis of primary igneous rock types and textures. Mineral modes were visually estimated. In many cases, several subintervals with subtle centimeter to few centimeter gradational to sharp changes in grain size and/or mode were grouped into a single lithologic unit. The subtle variations within a unit are described in the text of the hard rock VCDs. Mineral habits, igneous structures, and igneous fabrics were also recorded, as well as the nature of igneous contacts. Observations were recorded in spreadsheets for each lithologic unit in the core. Details of the individual measurements are given below.

### Rock classification

Igneous rocks were classified on the basis of abundance, grain size, and texture of their primary minerals based on the International Union of Geological Sciences (IUGS) system (Streckeisen, 1974; Le Maitre, 1989; Le Bas and Streckeisen, 1991) (Fig. F4). Plutonic rock names were assigned on the basis of primary phases present prior to alteration. For pervasively altered rocks, the term “primary assemblage” is used to refer to the estimated prealteration mineral assemblage. Minor modifications to the IUGS system were made to subdivide the rock types more accurately on the basis of significant differences rather than arbitrary cutoffs based on the abundance of a single mineral. We have attempted to follow as closely as possible the descriptions from Leg 209 (Kelemen, Kikawa, Miller, et al., 2004) to allow comparison of these records.

Basalts were subdivided according to the presence or absence of glass, grain size, and phenocryst content. If present, phenocrysts were put as modifiers in front of the rock name with a hyphen in between, according to their abundance. In the IUGS classification, “basalt” is defined on the basis of mineral mode or composition; grain sizes are variable. Because the basalts are commonly aphyric and very fine grained to aphanitic, mode determination was not feasible, so composition has been used to identify basalts. Following IUGS classification, basalts plot in a field on a SiO<sub>2</sub>-total alkali (Na<sub>2</sub>O + K<sub>2</sub>O) diagram (TAS) defined by SiO<sub>2</sub> and total alkali coordinates 45, 0; 45, 5; 52, 0; and 52, 5 (Le Bas and Streckeisen, 1991). “Diabase” is an intrusive basaltic rock emplaced as dikes or sills and characterized by subophitic to ophitic texture of plagioclase laths and augite. Diabase occasionally displays an aphanitic to very fine grained chilled margin (grain size <<1 mm) and a fine-grained (<1 mm) interior. Even in intervals of glassy basaltic composition rocks, if chilled margins or intrusive contacts were recognized the rocks were classified as diabase.

Description of the gabbros follows that of Leg 176 (Dick, Natland, Miller, et al., 1999), where the modifier “disseminated oxide” is used when the abundance of Fe-Ti oxide is 1%–2% and the modifier “oxide” is used when the abundance is >2%. If the olivine content ranges between 1% and 5%, then “olivine-bearing” is the modifier, and if it exceeds 5%, the rock is called olivine gabbro. Gabbros with orthopyroxene content between 1% and 5% are called orthopyroxene-bearing gabbro, and samples with >5% orthopyroxene are called gabbro-norite. The term “troctolitic gabbro” is used to describe olivine gabbros with 5%–15% clinopyroxene, and the rock name troctolite is used for rocks with <5% clinopyroxene. “Olivine-rich troctolite” is a rock that contains >70% olivine and relatively low modal plagioclase and clinopyroxene. Olivine-rich troctolite commonly contains subhedral to subrounded olivine and interstitial to poikilitic plagioclase and clinopyroxene in variable proportions. The term “leucocratic” is used to indicate high proportions of plagioclase. “Anorthositic” is used for gabbros with >80% plagioclase. The modifier “micro-” is used to distinguish gabbroic rocks with a dominant grain size of <1 mm (e.g., microgabbro, microtroctolite, and microgabbro-norite).

Leucocratic rocks with >20% quartz and <1% K-feldspar (a restricted part of the tonalite field of the IUGS system) are called trondhjemites in keeping with previous usage in the ocean crust literature.

Where alteration in ultramafic rocks is so extensive that estimation of the primary phase assemblages is not possible, the rock is called serpentinite. If, in primary assemblages, pseudomorphs and textures can be recognized in ultramafic samples, even though they are partially or completely replaced, the rock name used is based on the reconstructed primary assemblage and is termed serpentinitized (i.e., serpentinitized dunite).

On the hard rock VCDs, the rock names as described above are given at the top of each interval description; the IUGS names calculated from the mode are given in the text. Symbol swatches used in the VCDs are shown in Figure F5. If a mafic rock exhibits the effects of dynamic metamorphism such that the assemblage consists of secondary hydrous minerals that completely obliterate the protolith mineralogy and texture or if the rock is made up of recrystallized primary minerals such that the original igneous protolith cannot be recognized, the appropriate metamorphic rock names are used. The methods for describing the metamorphic and structural petrology of the core are outlined in subsequent sections of this chapter.

## Primary minerals

The primary rock-forming minerals recovered are olivine, orthopyroxene, clinopyroxene, spinel, Fe-Ti oxide, plagioclase, and amphibole. The following data are recorded on the VCDs (see “[Core descriptions](#)”):

- Visually estimated modal percent of the primary minerals
- Grain size
- Average crystal size for each mineral phase
- Mineral shape: equant, subequant, tabular, and elongated
- Mineral habit: euhedral, subhedral, anhedral, and interstitial

Accessory phases are also noted, and the above five classes of observations are collected. The modal percentage of each mineral includes both the fresh and altered parts of the rocks interpreted to represent that mineral.

Five major classes of rock (peridotite, pyroxenite, gabbro, diabase, and basalt) are delineated on the basis of their igneous texture. Textures are defined on the basis of grain size, grain shape and habit, preferred mineral orientation, and mineral proportions. The dominant grain size for all plutonic rocks is recorded as fine grained (<1 mm), medium grained (1–5 mm), coarse grained (5–30 mm), or pegmatitic (>30 mm).

## Igneous textures

We use the following textural terms: “equigranular,” “inequigranular,” and “intergranular” (only visible in thin sections). Inequigranular textures may be further described as seriate (continuous range of crystal sizes) or poikilitic (relatively large crystals of one mineral, enclosing smaller crystals of one or more other minerals, chadacrysts).

The terms “euhedral,” “subhedral,” “anhedral,” and “interstitial” are used to describe the shapes of crystals interpreted to preserve their igneous morphology. Crystal shapes are divided into four classes:

- Equant (aspect ratio = <1:2)
- Subequant (aspect ratio = 1:2 to 1:3)
- Tabular (aspect ratio = 1:3 to 1:5)
- Elongate (aspect ratio = >1:5)

Spinel occurs in various shapes that are divided into three categories:

- Equant: the shape is equidimensional with flat and/or curved surfaces.
- Interstitial: a transitional category between vermicular and equant. The outer surfaces of these spinel grains are often concave outward and

have thin tips departing from the corner of the grain.

- Vermicular: has intricate shape forming symplectic intergrowths with pyroxenes and/or olivine.

Igneous fabrics that are distinguished include “lamination” and “lineation” for rocks exhibiting a preferred orientation of mineral grains, “clusters” for mineral aggregates, and “schlieren” for lenses of igneous minerals.

The textural distinction between diabase and microgabbro is based on the presence or absence of subophitic or ophitic textures.

For basaltic rocks, the proportions and characters of phenocrysts, grain sizes, and vesicles define the following textures.

Phenocrysts are described for each mineral according to their abundance. The classifications for basalts are as follows:

- Aphyric (<1% phenocrysts)
- Sparsely phyric (1%–2% phenocrysts)
- Moderately phyric (2%–10% phenocrysts)
- Highly phyric (>10% phenocrysts)

Vesicularity is described according to the abundance, size, and shape (sphericity and angularity) of the vesicles. The subdivision was made according to the following scale:

- Nonvesicular (<1% vesicles)
- Sparsely vesicular (1%–5% vesicles)
- Moderately vesicular (5%–20% vesicles)
- Highly vesicular (>20% vesicles)

Groundmass crystallinity was classified according to the following scale:

- Aphanitic (individual grains cannot be distinguished)
- Microcrystalline (groundmass can be seen but not identified)
- Fine grained (grains <1 mm but can be identified)
- Medium grained (>1 mm grain sizes)

## Oxide and sulfide minerals

The abundance of primary Fe-Ti oxide and sulfide in the core is visually estimated.

Textures of oxide and sulfide minerals are described in terms of the habit of the mineral and its relationship with adjacent minerals. Oxide habits in hand sample are divided into the following categories:

- Disseminated (scattered grain to grain clusters with no pronounced fabric)
- Interstitial network (oxides that occur interstitial to the silicates)

Oxide shapes in hand sample are divided into the following categories: euhedral, anhedral, angular aggregates, amoeboidal aggregates, and interstitial lenses. “Euhedral” and “anhedral” are used when it appears that isolated individual grains are present.

Relative sulfide abundance in hand specimen is visually estimated using a binocular microscope.

### Igneous structures

Igneous structures noted in the core description include layering, gradational grain size variations, gradational modal variations, gradational textural variations, and breccias. “Layering” is used to describe planar changes in grain size, mode, or texture within a unit. Grain size variations are described as normal if the coarser part was at the bottom and as reversed if the coarser part was at the top. Modal variations are described as normal if mafic minerals are more abundant at the bottom and as reversed if mafic minerals are more abundant at the top.

### Dikes/Veins

The term “dike” refers to any crosscutting feature that formed by injection of magma and/or juvenile fluids, and the word “vein” describes epigenetic mineralized fractures. Veins are described in both “**Igneous petrology**” and “**Metamorphic petrology**.”

### Contacts between lithologic intervals

The most common types of contacts are those without chilled margins. These are planar, curved, irregular, interpenetrative, sutured, or gradational. “Sutured” refers to contacts where individual mineral grains are interlocking across the contact. In many cases, contacts are obscured by subsolidus or subgrain deformation and metamorphism; they are called “sheared” if an interval with deformation fabric is in contact with an undeformed interval, “foliated” if both intervals have deformation fabrics, or “tectonic” if the contact appears to be the result of faulting. Indistinct contacts are also described as “diffuse” in some cases.

### Thin section description

Thin sections of igneous rocks were examined to complement and refine the hand-specimen observations. In general, the same types of data are collected from thin sections as from hand specimens, and a similar terminology is used. All data are recorded in the thin section spreadsheet (see “**Core descriptions**”) and summarized in IODP-format thin-section descriptions. Crystal sizes are measured using a micrometer scale. The presence of inclusions, overgrowths, and zonation is noted, and the apparent or-

der of crystallization is suggested in the Comments section for samples with appropriate textural relationships. The presence and relative abundance of accessory minerals such as oxides, sulfides, apatite, and zircon are noted. Abundant modal orthopyroxene was also observed in thin section in many gabbroic rocks but was not readily identified in hand sample. Thus, many rocks identified as gabbro in hand sample were subsequently classified as gabbronorite after thin section examination.

### Electron beam analysis

A binocular microscope equipped with an electron beam energy-dispersive X-ray spectrometer (miniprobe) was brought on board for Expeditions 304 and 305 and used for mineral identification and characterization. The same system was used at sea during a survey cruise and proved to be a valuable aid in sample characterization (E. Hellebrand, pers. comm., 2005).

The miniprobe system consists of a binocular microscope equipped with a standard cold cathode electron source manufactured by Cambridge Image Technology Ltd., a vacuum chamber, and a silicon drift detector (Fig. F6). The silicon drift detector is a state-of-the-art high-resolution X-ray detector and is cooled by an internal Peltier element (no liquid nitrogen required). It can therefore operate at room temperature and gives excellent performance even at very high count rates. The particular detector technology was derived from the development of the Mars APXS spectrometer for the Sojourner and Pathfinder missions. In connection with a thin beryllium entrance window (8  $\mu\text{m}$ ), it guarantees a wide energy response to incoming radiation. The silicon drift detector in the packaged configuration is suitable for X-rays in the energy range between 1 and 30 keV. Hardware control and data analysis are performed by an energy dispersive system (EDS) computer with EMRA (version 10.4). The spectral resolution of the EDS corresponds to that of an scanning electron microscope and lies, in average, at 180 eV.

The sample chamber can hold thin sections as well as grain mounts. Samples do not require polishing or coating, as is as needed for standard electron microprobe analysis, before analysis.

An internal Ge standard is used for calibration. Measurements were performed using the following parameters:

- Current = 100  $\mu\text{A}$
- Voltage = 20 kV
- Beam diameter = 100  $\mu\text{m}$
- Measurement time = 100 s

A minimum of ~10,000 gross counts is required to maintain a good analysis.

The main use of the miniprobe onboard was to identify minerals in ship-made thin sections. In addition, some spinels from peridotites from Hole 1309B were measured to obtain their Cr# (molar Cr/[Cr + Al]), an indicator of the degree of melting (Hellebrand et al., 2001). Spinel compositions obtained from the miniprobe do not yield true values but need an additional external correction. A well-known set of homogeneous spinels from abyssal peridotites, measured on the Jeol 8900 microprobe of the University of Mainz (Germany), was used for reference (Fig. F7). These spinels cover the variational range of spinel Cr# in abyssal peridotites. There is a good linear correlation ( $R^2 = 0.90$ ) between the analyzed values and reference values. Based on this linear correlation, the obtained Cr numbers were corrected as

$$\text{Cr\#} = 0.9594 \times \text{Cr\# (miniprobe)} - 012.833.$$

## Metamorphic petrology

Metamorphic characteristics of the drill core were determined using VCDs (macroscopic and mesoscopic), microscopic thin section descriptions, and X-ray diffraction (XRD) analyses. In this report, the terms “metamorphism,” “alteration,” and “hydration” are used loosely and interchangeably without making implications about open- versus closed-system behavior. The term “metasomatism” will apply to rocks, such as the tremolite-chlorite schists, the composition of which have clearly changed during metamorphism. Hydration reactions rarely involve the simple addition of H<sub>2</sub>O. At the level of this study, however, we are incapable of detecting minor changes in bulk composition, and we will therefore consider hydration reactions to be mostly related to the addition of H<sub>2</sub>O.

For each entry into any table, the following information was recorded: leg, site, hole, core number, core type, section number, piece number(s) (consecutively downhole), and position in the section. All metamorphic descriptions and measurements were made on the archive halves of the cores, except where otherwise noted. The metamorphic petrology team worked together during the same shift to minimize measurement inconsistencies. Each member of the team was responsible for making a specific set of observations throughout the entire core, but in the initial phase of each cruise, members worked together to make maximum use of the varied experiences of the team. For definitions of terms used in the VCDs and logs, see Tables T1 and T2.

## Visual core descriptions

The VCDs (Fig. F2) provide information (on intervals) on the extent of replacement of igneous minerals by secondary minerals, as well as the nature and approximate modes of secondary mineral assemblages. Except for simple cases, quantification of individual mineral modes was only possible where thin section or XRD data were available. Where several pieces showed similar characteristics, secondary mineral modes were assigned to the whole group on the basis of thin section or XRD analysis. More detailed information on an interval basis is presented in the alteration logs (see “[Supplementary material](#)”), which were used to generate the summary information in the VCDs. Total alteration intensity was classified as shown in Figure F8 and entered graphically into the VCD (Fig. F2).

The VCDs record overprinting alteration relationships and any association between alteration and deformation fabrics. The presence of characteristic textures (vein halos, pseudomorphs, alteration zones, corona textures, and porphyroblasts) and the lithological controls on alteration are noted. The presence, approximate abundance, and mineralogy of veins were recorded on the VCDs, with more detailed information on an interval basis given in the vein log (see “[Supplementary material](#)”).

## Alteration log

The alteration log was used to describe alteration assemblages and textures on an interval basis. The intervals on this log do not necessarily correspond to the lithologic intervals defined by the igneous team. Alteration assemblages were described by color and estimated mineralogy and given a numerical code (refined by thin section and XRD study; see Table T3). A distinction was made between overprinting alteration assemblages and assemblages localized by preexisting lithology changes. For example, a core of serpentinized dunite containing a gabbro dike altered to a chlorite-tremolite assemblage would be described as three discrete intervals on three rows in the log. On the other hand, a core of serpentinized dunite containing a subinterval with vein halos would be described using two rows: one long interval of serpentinized dunite and a shorter subinterval containing the overprinting vein halo assemblage. For Expedition 305, this type of observation was given as a percent and vein data would generally be logged separately unless the vein had an extensive halo. In the same way, overprinting zones of breccia, cataclasite, or ductile shear containing new alteration assemblages or textures were recorded as subintervals. The total alteration percentage recorded is an estimate of the percentage of that interval af-

ected by the assemblage at the time of formation (i.e., a long interval might be recorded as 100% serpentine, whereas a subinterval might contain 20% vein halos of overprinting talc).

The alteration log was used to record the presence or absence of textures (pervasive alteration, pseudomorphs, coronas, foliation, clasts, halos around clasts or veins, and the approximate percentage of vein material in the interval). During Expedition 305, the approximate percent of vein material was recorded in the vein log. Approximate mineral proportions and the possible identity of unidentified mineral phases were recorded and refined following thin section observation and/or XRD analysis. Where pseudomorphic textures are present, the suggested primary and secondary phases were noted as comments. Pervasively serpentinized rocks with unknown protolith are named “serpentinite.” If the nature of the protolith can be established, the adjective “serpentinized” is added to the rock name. This estimated alteration intensity is added to the rock name (e.g., completely serpentinized harzburgite, highly altered metagabbro, etc.).

### Vein log

During Expedition 304, a combined vein log was recorded in conjunction with the structural geology team (see “[Supplementary material](#)”). Veins and vein sets were recorded on an interval basis, and vein-free intervals were also noted. Where several vein types were present in an interval, these were numbered and data were recorded on separate rows. In the metamorphic/alteration part of the vein log, we recorded vein color and vein textures using a series of codes (Fig. [F9](#)). Textures were recorded in terms of vein shapes (straight, sigmoidal, irregular, pull-apart, and fault vein), connectivities (isolated, single, branched, and network), textures (massive, cross-fiber, slip-fiber, vuggy, and polycrystalline), and structures (simple, composite, banded, haloed, and intravenous). Any vein that did not fit into the classification scheme was entered as a separate code (9) and described in a comment. The length and width of each vein, as well as its orientation, were measured by the structural geology team. The percent volume of each vein type within a piece or interval was estimated visually. Acronyms used in the alteration and vein logs and in the thin section description forms are listed in Table [T1](#). Table [T4](#) lists a classification of vein types that was developed in light of experience in Hole U1309B. This was used in the vein log for Hole U1309D in a “vein type” column but not in the Hole U1309B vein log. Minor changes were also made in the vein mineralogy columns between Cores 304-U1309D-1R to 22R and

Cores 304-U1309D-23R to 78R. Hence, two separate vein log spreadsheets for the uppermost 400 m of Hole U1309D are archived (see “[Supplementary material](#)”).

During Expedition 304, a separate log was also made of the intensity of vein-related alteration, together with the relationship between this and breccia zones and late magmatic leucocratic dikelets (see vein alteration logs in “[Supplementary material](#)”). In this log, the lithology, interval, and approximate percent of the interval consisting of veins and altered vein halos was estimated, concentrating on greenschist-facies veins (including talc-tremolite veins in ultramafic rocks but not hornblende veins or fracture-controlled serpentine/prehnite alteration). This log, as well as the alteration log (see “[Supplementary material](#)”) was used to create alteration-depth diagrams.

During Expedition 305, the vein log (see “[Supplementary material](#)”) was recorded independently of the structural geology team and no vein alteration log was recorded. Classifications used in the vein log were the same as for Expedition 304 with the exception of the vein types, where a simpler scheme was adopted (Table [T4](#)). The percent volume of each vein type within a piece or interval was calculated from width and length data on Expedition 305 only.

### Thin section descriptions

Thin section descriptions were made using the standard IODP template (see “Thin Sections” for all sites). Stable mineral parageneses were noted, as were textural features of minerals indicating overprinting events (e.g., coronas, overgrowths, and pseudomorphs). Secondary mineral assemblages and replacement relations to primary phases were described, and secondary modes and, where possible, grain sizes were estimated visually. The nature of minor and trace phases (carbonates, sulfides, and oxides) and the extent of Cr spinel alteration could rarely be established by visual core description. In some cases, phases were identified using a microscope-mounted electron beam energy-dispersive X-ray spectrometer (miniprobe) supplied by E. Hellebrand. See “[Electron beam analysis](#)” in “Igneous petrology” for a description. The modal estimates allowed characterization of the intensity of alteration and aided in establishing the accuracy of the macroscopic and microscopic visual estimates of the extent of alteration. Whole thin section images were used to guide microtextural studies, and for Hole U1309B they were then compiled with photomicrographs into annotated photo sheets (see “[Supplementary material](#)”).

## X-ray diffraction

Phase identification in selected samples of whole-rock shipboard powders and metamorphic vein material was aided by XRD analyses using a Philips model PW1729 X-ray diffractometer with  $\text{CuK}_\alpha$  radiation (Ni filter). Each sample was freeze-dried, crushed, and mounted with random orientation in an aluminum sample holder. Instrument conditions were as follows:

- Voltage = 40 kV
- Current = 35 mA
- Goniometer scan (bulk samples) =  $2^\circ\text{--}70^\circ 2\theta$
- Step size =  $0.02^\circ 2\theta$
- Scan speed =  $1.2^\circ 2\theta/\text{min}$
- Count time = 1 s

Peak intensities were converted to values appropriate for a fixed slit width. An interactive software package (MacDiff version 4.2.5 PPC) was used to identify the primary minerals (public domain software is available from [www.pangaea.de/Software](http://www.pangaea.de/Software)). Identifications were based on multiple peak matches, using the mineral database provided with MacDiff. Relative abundances reported in this volume (trace, minor, and major components) are useful for general characterization but are not precise.

## Structural geology

Expeditions 304 and 305 generally followed the same conventions for structural studies in order to maintain compatibility of the data. The conventions adopted during Expedition 304 were based on previous “hard rock” drilling programs (e.g., ODP Legs 118, 131, 140, 147, 153, 176, 179, and 209). Several minor changes in nomenclature and procedure were adopted during Expedition 305. These changes are described below. Because no peridotite was found during Expedition 305, its note was mostly excluded. Where procedures followed directly from previous cruises, references to the appropriate ODP *Initial Reports* “Explanatory Notes” chapters are given.

### Overview of macroscopic core descriptions

Whole cores were oriented for cutting prior to curation. Cores were marked to maximize dip on planar structures so that the dominant structure dips toward  $270^\circ$  in the core reference frame (i.e., toward the right looking down at the cut surface of the archive half of the core). Where no obvious structures were present, cores were marked to maximize contiguity with adjacent core pieces. The sign convention for the core follows the paleomagnetic conventions

of a right-hand rule with +z vertical and down the core (Fig. F10).

All descriptions and structural measurements during Expeditions 304 and 305 were made on the archive half of the core. Following procedures described in the Leg 153 *Initial Reports* volume (Shipboard Scientific Party, 1995), data were entered into a VCD form (Figs. F2, F11) used in conjunction with two spreadsheet logs (see “[Supplementary material](#)”). The structural sketches are intended to illustrate the most representative structures and crosscutting relationships in a core section; in addition, a brief general description of the structures is printed on the VCD form (see “[Supplementary material](#)”). During Expedition 304, paper copies of spreadsheet forms were used for recording specific structures and measurements during core description. Separate spreadsheets were used to record structural data on the following

- Alteration veins
- Brittle structures: breccias, faults, joints, drilling-induced fractures, serpentine foliation, cataclastic fabric intensity
- Crystal-plastic deformation: mylonitic foliation, sense of shear
- Igneous structures: magmatic foliation, compositional layering, igneous contacts

During Expedition 305, specific structures and measurements during core description were directly typed into spreadsheet forms. Separate spreadsheets were used to record structural data on the following:

- Brittle structures: breccias, faults, joints, drilling-induced fractures, serpentine foliation, cataclastic fabric intensity, alteration veins
- Magmatic and crystal-plastic structures: magmatic foliation, compositional layering, igneous contacts, crystal-plastic foliation, sense of shear

The description and orientation of all features were recorded using curated depth so that “structural intervals” could be correlated with lithologic core descriptions. The spreadsheets were organized to record six separate types of measurements using the deformation intensity scales summarized in Figure F12. During both Expeditions 304 and 305, the structural geologists worked together during the same shift to minimize measurement inconsistencies. During Expedition 304, each member of the team was responsible for making a specific set of observations throughout the entire core (e.g., characterization of crystal-plastic fabric intensity). During Expedition 305, the structural geologists were divided into two teams: one was responsible for high-temperature structures including both magmatic and crystal-plastic deformation, and the other was responsible for

low-temperature structures including veins, cataclasis, serpentine foliations, and so on. Each team was responsible for making a specific set of observations throughout the entire core (e.g., characterization of crystal-plastic fabric intensity).

### Nomenclature

We used feature identifiers for structures similar to those outlined by the Leg 153 Shipboard Scientific Party (1995). Modifications to this scheme are shown in the comments checklist (Table T5). Where brittle fabrics overprint crystal-plastic fabrics or deformation was “semibrittle,” a note was made as “brittle-plastic” and documented in the magmatic and crystal-plastic structures spreadsheet (see “[Supplementary material](#)”).

The shorthand notation for structural units was as follows (more detail in Table T5):

- Brittle structures:
  - Vein (V): hydrothermal (Vh), microfault with fibrous minerals (Vf), cataclasis accommodated (Vc)
  - Breccia (B): hydrothermal breccia (Bh), cataclastic breccia (Bc)
  - Fault (F): fault zone (FZ)
  - Foliation (S): serpentine foliation (S or Ss)
- Magmatic and crystal-plastic structures:
  - Vein (V): magmatic vein (Vm)
  - Foliation (S): magmatic foliation (Sm), crystal-plastic foliation (Sp), brittle-plastic foliation (Bp)
  - Alteration (A): alteration front (Af)
  - Contacts (c): igneous contact (Ic)

### Structural measurements

Structural features were recorded in centimeters from the top of each core section. Depth was defined as the point where the structure intersects the center of the cut face of the archive half of the core (Fig. F10) or, if the feature does not appear in the center of the core, the depth of the centroid of the feature projected to the center of the core. Where they occur, crosscutting relationships were described with core section depth. Apparent fault displacements of planar markers were recorded as they appeared on the cut face of the archive half of the core. Displacements observed on the vertical core cut face were treated as dip-slip components of movement and labeled in spreadsheets as either normal or reversed for faults inclined  $<90^\circ$ ; their displacement in millimeters was also recorded. Shear sense indicators were also marked on the spreadsheets. For vertical faults, displacements were recorded as up or down (e.g., west side up or east side down [+y is east]). Offset fea-

tures visible on the upper and lower surfaces of core pieces (+z is upper side) were treated as strike-slip components of movement and marked either sinistral or dextral. Displacements were measured between offset markers displaced parallel to the trace of the fault. Slickenside and/or slickenfiber orientation trend and plunge measurements or the trend and plunge direction of the slip line between offset linear markers were incorporated wherever possible to determine dip-slip, oblique-slip, or strike-slip components. The structures were oriented with respect to the core reference frame; the convention that was used for the core reference frame (Fig. F10) is shown at the top of the comments box in the structural data spreadsheets (see “[Supplementary material](#)”).

Planar structures were oriented using the techniques outlined during Leg 176 (Shipboard Scientific Party, 1999). Apparent dips in the cut plane of the archive half were recorded as two-digit numbers (between  $00^\circ$  and  $90^\circ$ ) with apparent-dip azimuth either as  $090^\circ$  or  $270^\circ$  (Fig. F10). A second apparent dip was recorded in a different orientation with different apparent-dip azimuths (usually either  $000^\circ$  or  $180^\circ$ ). The two apparent dips and their azimuths were used to calculate the true dip and strike direction with respect to the core reference frame. These calculations were performed using a macro routine within each spreadsheet (see “[Supplementary material](#)”).

The true dip and strike directions of the samples were reoriented using available paleomagnetic declinations to rotate the measurements to a common alignment. The orientation of this common alignment was chosen to have an azimuth of zero, but this alignment does not necessarily correspond to true north because of the effects of tectonic rotation on the orientation of the magnetic declination direction. The data were plotted on lower-hemisphere stereographic projections using the shareware of R. Allmendinger ([www.geo.cornell.edu/geology/faculty/RWA/RWA.html](http://www.geo.cornell.edu/geology/faculty/RWA/RWA.html)) and the careware of D. Mainprice ([www.dstu.univ-montp2.fr/TEC-TONOPHY/index.html](http://www.dstu.univ-montp2.fr/TEC-TONOPHY/index.html)).

### Fabric intensities

A semiquantitative scale of deformation and alteration fabric intensities was used by the shipboard structural geologists during core description (e.g., Cannat et al., 1991; Dick et al., 1991). These scales, shown in Figure F12, were modified from the deformation scales used during Legs 176 (Shipboard Scientific Party, 1999) and 209 (Shipboard Scientific Party, 2004). Where possible, we assigned specific values to intensity estimates (e.g., vein spacing or matrix percentage in a cataclastic zone). For some categories, however, classification is difficult (e.g.,

the intensity of any crystal-plastic fabric), in which case we used the previously adopted qualitative estimates of intensity based on hand-specimen and thin-section observations. We documented six distinct types of fabric intensity measurements (Fig. F12):

- Magmatic (Mf): presence and intensity of any shape-preferred orientation of magmatic phases. Four levels, from no shape-preferred orientation (0) to strong shape-preferred orientation (3), were used.
- Crystal-plastic (CPf): six levels of deformation intensity were used, ranging from a lack of any crystal-plastic fabric (0), through three stages of foliation and porphyroblast development (1–3), to mylonitic and ultramylonitic fabrics (4–5). The textural criterion used for gabbroic rocks, on which this was based, was modified slightly for peridotites. Occasionally, it proved difficult to differentiate between crystal-plastic and cataclastic deformation in relatively high strain shear zones based on hand-specimen observations only. In this case, we introduced a new classification: brittle-plastic foliations (Bp).
- Cataclastic (Cf): six levels of deformation intensity were used with fabrics categorized depending on the percentage of matrix present within each cataclastic zone. Thin section descriptions, wherever available, significantly aided this categorization.
- Joints (J: fractures without displacement): four levels of joint density were used, depending on the average frequency of joints across a 10 cm depth interval along the long axis of the core. Joints were distinguished from faults (cataclastic features) by the lack of any identifiable offset. Some sections of the core contained small subhorizontal microfractures commonly related to unloading accompanying drilling. The same scale as for joints (0–3) was used for the density of these drilling-induced features.
- Veins (V): six levels of vein density were used, depending on the average frequency of veins across a 10 cm depth interval along the long axis of the core. Alteration veins are those which contain metamorphic phases. In some cases, these may have originally been igneous, but no primary phases or their characteristic pseudomorphs were recognized. Magmatic veins are compositionally distinct mineral segregations that may be concordant or discordant.
- Serpentine foliation (Ss or S): formation of strong planar fabrics may occur during serpentization by development of closely spaced subparallel veins termed ribbon texture (O’Hanley, 1996). The

texture is characterized by anastomosing, commonly cross-fiber, replacement serpentine veins. In general, the veins wrap around relict or pseudo-morphed pyroxene grains with little evidence of shear offset. This texture may parallel preexisting crystal-plastic foliation, and its intensity may reflect stress state or the presence of a preexisting fabric in the rock. The strength of serpentine foliation is rated on a scale from 0 (massive, no foliation) to 3 (strongly foliated). If more than one obvious serpentine foliation was present, the orientation and intensity of all fabrics were recorded.

### Thin section descriptions

Thin sections were examined to characterize the microstructural aspects of important mesoscopic structures in the core. Classes of information that were obtained include deformation mechanisms on a mineral-by-mineral basis, kinematic indicators, crystallographic (where obvious) and shape fabrics, qualitative estimates of the degree of crystallographic preferred orientation, syn- and postkinematic alteration, and the relative timing of microstructures. The orientation of thin sections relative to the deformation fabrics and core axes is noted in the comments section of the spreadsheet. Thin sections were oriented, where possible, in the core reference frame described in **“Structural measurements.”** A large variety of microstructures occur in gabbros (see “Igneous Petrology,” p. 12, and “Structural Geology,” p. 54, in Shipboard Scientific Party, 1999). For the purposes of entering data into spreadsheets, a number of textural types characterized by specific microstructural styles were used based on the Leg 153 and 176 descriptions (Table T6). There is a superposition of different microstructures or deformation mechanisms attributable to different stages of cooling. Thus, the physical state of the material during fabric development may span the transition from hyper-solidus to subsolidus. Igneous fabrics defined entirely by minerals with no crystal-plastic deformation microstructures are termed magmatic. We used four intensity categories:

- 0 = absent
- 1 = questionable
- 2 = weak
- 3 = strong

Where local crystal-plastic fabrics are produced in the presence of melt (e.g., Hirth and Kohlstedt, 1995; Bouchez et al., 1992; Means and Park, 1994; Nicolas and Ildefonse, 1996), we term the physical state “crystal plastic ± melt.” Where fabric development is produced entirely by dislocation creep, we use the term “crystal plastic” to define the physical state of the rock. For crystal-plastic fabrics, we used six categories:

- 0 = absent
- 1 = only local nests of neoblasts
- 2 = ~10% neoblasts
- 3 = 40%–90% neoblasts
- 4 = mylonitic with rare porphyroclasts left or other independent evidence for high strain in rocks with no mylonitic appearance
- 5 = ultramylonitic

In addition, during Expedition 305, we estimated relative stress levels based on neoblast size:

- 0 = no neoblasts
- 1 = neoblast size >200  $\mu\text{m}$
- 2 = a typical range of neoblasts (50–250  $\mu\text{m}$ )
- 3 = neoblast size <100  $\mu\text{m}$

A table with thin section intensities and short comments (30405STR.XLS) is available in [“Supplementary material.”](#) For a description of the methods for calculating averages from logged intervals, including MatLab calculations, see [“Supplementary material.”](#)

## Geochemistry

During Expeditions 304 and 305, we performed chemical analyses of samples selected by the shipboard scientific party using inductively coupled plasma–atomic emission spectroscopy (ICP–AES) and gas chromatography (GC). Various rock types, including basalt, diabase, and gabbroic and ultramafic rocks, were analyzed for major oxide and selected trace element concentrations. Sampling and analytical procedures were adapted from those developed during ODP Legs 147, 153, 176, 187, 197, 203, and 209, and the overall strategy was described in ODP *Technical Note 29* by Murray et al. (2000). The shipboard analytical facilities are reviewed in the Leg 147 and 187 ODP *Initial Reports* volumes (Shipboard Scientific Party, 1993, 2001). The ICP–AES was first used during Leg 187, and additional details on hard rock analytical procedures are given in the Leg 197 and Leg 209 *Initial Reports* volumes (Shipboard Scientific Party, 2002, 2004).

### ICP–AES analyses of major and trace elements

#### Sample preparation

Selected representative samples were first cut with a diamond-impregnated saw blade and wet-ground on a diamond abrasive wheel to remove surface contamination. Samples were washed in an ultrasonic bath containing methanol for ~10 min, followed by three consecutive ~10 min washes in an ultrasonic bath containing nanopure deionized water. Samples were then dried for ~12 h in an oven at 110°C. The

cleaned whole-rock samples (ideally ~20 cm<sup>3</sup> in size) were reduced to fragments <1 cm in diameter by crushing them between two disks of Delrin plastic in a hydraulic press or in a percussion crusher, followed by grinding for ~5 min in a Spex 8510 shatterbox with a tungsten carbide barrel. Approximately 1 g of sample powder was weighed on a Scientech balance and ignited at 1025°C for 4 h to determine weight loss on ignition (LOI).

Aliquots of 100  $\pm$  0.5 mg of the ignited whole-rock powders were mixed with 400  $\pm$  0.5 mg of lithium metaborate (LiBO<sub>2</sub>) flux that had been preweighed on shore. All samples and standards were weighed on the Cahn Electrobalance under computer control. Weighing errors are conservatively estimated to be  $\pm$ 0.01 mg.

Mixtures of flux and rock powders were fused in Pt–Au crucibles at 1050°C for 5 min in a Bead Sampler NT-2100. Cooled beads were transferred to 125 mL polypropylene bottles and dissolved in 50 mL of 2.3M nitric acid (HNO<sub>3</sub>) by shaking with a Burrell bottle shaker for 1 h. After dissolution of the glass bead, all of the solution was filtered to 0.45  $\mu\text{m}$  into a clean 60 mL wide-mouth polypropylene bottle. Next, 2.5 mL of this solution was pipetted to a plastic vial and diluted with 17.5 mL of 2.3M HNO<sub>3</sub> to bring the total volume to 20 mL. This solution-to-sample dilution, used for major and trace elements, is 4000. Dilutions were conducted using a Brinkman digital dispenser (50 mL).

#### Analysis

Major and trace element concentrations of powder samples were determined with the JY2000 Ultracore ICP–AES. The JY2000 sequentially measures characteristic emission intensities (with wavelengths between ~100 and 800 nm). We routinely ran two element menus: major elements (P, Si, Mn, Fe, Mg, Ti, Ca, Al, Na, and K [in order as measured in the sequence]) and trace elements (Co, Ni, Cr, V, Cu, Zr, Sc, Y, Sr, and Ba [in order as measured in the sequence]). Certified international rock reference materials, calibration and drift solutions, and chemical procedure blanks were included with the unknown samples for each sample run. The elements analyzed, emission lines used, limits of detection, and specific analytical conditions during Expeditions 304 and 305 are provided in Table T7. Detection limits were calculated as being three times the positive blank intensity transferred (using procedure blanks of Runs 1–12). This method to calculate the limit of detection results in a very conservative estimate for the analytical capability for low concentrations.

The JY2000 plasma was ignited 30 min before each run to allow the instrument to warm up and stabi-

lize. After the warm-up period, a zero-order search was performed to check the mechanical zero of the diffraction grating. After the zero-order search, the mechanical step positions of emission lines were tuned by automatically searching with a 0.002 nm window across each emission peak using standard reference material BHVO-2 prepared in 2.3M HNO<sub>3</sub>. During the initial setup, an emission profile was collected for each peak, using BHVO-2, to determine peak-to-background intensities and to set the locations of background points for each element. The JY2000 software uses these background locations to calculate the net intensity for each emission line. The photomultiplier voltage was optimized by automatically adjusting the gain for each element using the standard with the highest concentration for that element (either BHVO-2 or JP-1). Before each run, a profile of BHVO-2 was collected to assess the performance of the instrument from day to day. A typical analytical session for 12 samples lasted ~6–7 h, depending on the chosen element menu (major or trace) and the number of replicate analyses.

All ICP-AES data presented in the site chapter reports were acquired using the Gaussian analytical mode (mode 2) of the Windows JY2000 software (version 5.01). During Expedition 304, this mode was used to fit a Gaussian curve to 5 points, each measured for 1 s across a peak, and during Expedition 305, it was used to fit a Gaussian curve to 7 points, each measured for 0.5 s, across a peak. The fit was then integrated to determine the area under the curve. This mode requires about a factor of 3 more analysis time compared to simply measuring a single peak intensity, but it leads to considerable improvement in analytical precision (Shipboard Scientific Party, 2001). We used the concentric nebulizer for the JY2000 because it delivers a finer aerosol to the plasma and results in a more stable signal (Shipboard Scientific Party, 2001). Use of this nebulizer requires filtering the solutions, as well as somewhat greater dilution factors to reduce clogging.

In order to determine the optimum analysis conditions for elements in the various rock types sampled, three different nebulizers were used during Expedition 304 and their results were compared: a modified Babington glass nebulizer (V-Groove), a Burgener polymer Mira Mist nebulizer (Miramist), and a concentric glass nebulizer (Meinhard). The Meinhard and Miramist nebulizers deliver a finer aerosol to the plasma and result in a more stable signal. Use of these nebulizers requires filtering the solutions, and high dilution factors are needed to reduce clogging. Salting and clogging nevertheless occurred during ICP-AES runs, causing interference with the gas flow and nebulization pattern. Over a single set of

analyses, the Miramist nebulizer exhibited reduced clogging and salting, but an inability to effectively remove deposits precluded its further use. We used the Meinhard for the JY2000 for most of the analyses during Expedition 304 and all the Expedition 305 analyses. During Expeditions 304 and 305, the instrument performance and stability were best when using shorter elemental menus for each run, operating at 4000-fold dilution, and running major and trace elements as separate analytical routines.

The ICP-AES runs included duplicates of the three certified rock reference materials, JP-1, BIR-1, and JA-3, uniformly distributed over the run. To monitor the sensitivity of the instrument, eight drift standards (BHVO-2) were measured at least every fifth position and used for a drift correction. During Expedition 305, for the analysis of Cr and Ni, the BHVO-2 drift standard was spiked with artificial Cr and Ni standards (SPEX; 1000 ppm in 2% HNO<sub>3</sub>) to achieve a concentration of 2 ppm Cr and 0.7 ppm Ni. A procedure blank solution, derived from a LiBO<sub>2</sub> fusion without a sample, was measured twice, at the beginning and the end of the run. In between samples and standards, a 2.3N HNO<sub>3</sub> wash solution was run for 90 s to avoid cross contamination. A typical run of 30 positions included 2 blanks, 7 drift standards, 9 certified rock standards (primary and secondary), and 12 unknowns. Certified international rock reference materials (see below) were used to test analytical accuracy and reproducibility of the obtained data. ROA-3, a pyroxenite from the Ronda ultramafic massif (Remaïdi, 1993), Sample 305-U1309D-171R-4, 18–30 cm, a gabbro sampled during Expedition 305, and BAS-140, a shipboard diabase standard (Sparks and Zuleger, 1995; Bach et al., 1996), were used as secondary standards during ultramafic rock, gabbro, and basalt analyses, respectively.

### Data reduction

Following each analytical session, the raw intensities were transferred to a data file and data reduction was completed using a spreadsheet to ensure proper control over standardization and drift correction. Once transferred, the average raw net intensities, derived from three single values, were recalculated if the precision indicated analytical outliers, which are usually related to the harsh environment in which the instrument was operated. Intensities were then corrected for the procedural blank. A drift correction was then applied to each element by linear interpolation between the drift-monitoring solutions run before and after a particular batch of samples. The interpolation factor for each sample is based on the time of the analysis. Following blank subtraction and drift correction, concentrations for each sample

were calculated from the average intensity per unit concentration for the standards JP-1, BIR-1, and JA-3 (Geological Survey of Japan, 2003; U.S. Geological Survey, 2003). A blank was also included in the regression, with both its intensity and concentration set to zero.

Tables **T8** and **T9** show the analytical uncertainties based on international rock reference materials and samples during Expeditions 304 and 305, respectively. During Expedition 304, estimates of accuracy and precision for major and trace element analyses were based on replicate analyses of ROA-3, DTS-1, BHVO-2, BAS-140, and BIR-1 run as unknowns. During Expedition 305, they were based on replicate analyses of three international reference materials (JB-3, JGb-1, and DTS-1) (Geological Survey of Japan, 2003; U.S. Geological Survey, 2003) and Sample 305-U1309D-171R-4, 18–30 cm. Repeatability of major element measurements was typically >5% (1 relative standard deviation [RSD]), except for phosphorous. Trace element analyses are typically repeatable within 5% (1 RSD), except for phosphorous, cobalt, copper, and some values near the detection limit (see Table **T7** for instrument detection limits).

### Gas chromatography

To more fully investigate LOI for each sample, GC separation of sample volatiles was carried out using a Carlo Erba NA 1500 CHS analyzer, in which the respective gaseous oxides of C and H were quantitatively determined by a thermal conductivity detector following the procedure developed during Leg 209. The sample introduction system has a vertically mounted quartz tube containing small pellets of reduced Cu separated by a small amount of quartz wool from tungstic anhydride, which acts as a catalyst. Samples were dropped into the tube in tin boats and heated at 1010°C in the presence of oxygen for ~75 s. During this time, nitrogen, hydrogen, carbon, and sulfur released from the sample are oxidized and swept into the GC using a helium carrier gas. The sulfur from sulfide minerals is oxidized to SO<sub>2</sub>, and SO<sub>3</sub> is released from any sulfate minerals present in the sample. Aliquots of sulfanilamide (C<sub>6</sub>H<sub>8</sub>N<sub>2</sub>O<sub>5</sub>S) weighing between 0.5 and 2.5 mg were used for primary calibration of the instrument. A single sample analysis required ~12 min. During this time, signal intensity at the detector was continuously recorded, and N, C, H, and S separated by the GC were measured sequentially at ~60, 120, 320, and 465 s. Following blank subtraction, concentrations for each sample were calculated from the integrated peak areas of the respective gases relative to those for the standard using a linear regression. The blank was included in the regression.

Sample analyses were performed on rock powder dried at 1100°C for 12 h. Sample sizes were typically 5–12 mg. The certified international rock reference material JP-1 (Imai et al., 1995; Geological Survey of Japan, 2003) and the internal laboratory standard 147 895D-10W (Puchelt et al., 1996) were routinely measured to monitor analytical accuracy and reproducibility. Typical analytical sessions included multiple analyses of each of these standard rocks and triplicates of each unknown sample. Results of the GC analyses for BAS-140 and JP-1 during Expedition 304 are presented in Table **T10**. Based on 12 runs, the reproducibility of JP-1 ( $N = 48$  for CO<sub>2</sub>;  $N = 49$  for H<sub>2</sub>O) and 147 895D-10W ( $N = 35$  for CO<sub>2</sub>;  $N = 44$  for H<sub>2</sub>O) was better than 6.5% for CO<sub>2</sub> and better than 4.0% for H<sub>2</sub>O during Expedition 305. The average CO<sub>2</sub> and H<sub>2</sub>O concentrations obtained for JP-1 and 147 895D-10W overlap published values (Imai et al., 1995; Puchelt et al., 1996; Geological Survey of Japan, 2003) within 2% and 4%, respectively. Detection limits taken from Expedition 304, calculated as three times the standard deviation of all the blank analyses, are 0.04 wt% for CO<sub>2</sub> and 0.15 wt% for H<sub>2</sub>O. In comparing the GC volatile analyses to the LOI results, it is also important to bear in mind that conversion of Fe<sup>2+</sup> to Fe<sup>3+</sup> during ignition may produce a gain in weight that is 11.1% of the percentage of ferrous Fe contained in the sample. This can lead to LOI analyses that are less than the volatile concentrations determined by the GC analysis.

Complete sample analyses are given in the CHEM-DATA.XLS file (see “**Supplementary material**”).

### Paleomagnetism

Paleomagnetic and rock magnetic investigations during Expeditions 304 and 305 were primarily designed to (1) determine the characteristic remanence directions for use in tectonic studies, (2) assess the orientation and significance of magnetic fabrics, and (3) evaluate whether the recovered materials constitute a suitable source for marine magnetic anomalies. To accomplish these goals, paleomagnetic measurements were performed on discrete minicore and cube samples and, where practical, on continuous pieces of the archive halves. The azimuths of core samples recovered by rotary drilling are unknown. All magnetic data are therefore reported relative to the following core coordinates: +x (north on plots) is into the face of the working half of the core, +y (east on plots) points toward the right side of the face of the working half, and +z is down (see Fig. **F10**).

The remanence of archive halves was measured using a pass-through 2G Enterprises direct-current Superconducting Quantum Interference Device (DC-

SQUID) rock magnetometer (model 760R). The magnetometer is equipped with an inline alternating-field (AF) demagnetizer (2G model 2G600) that can apply peak fields as high as 80 mT. Both the magnetometer and AF demagnetizer are interfaced with a computer and are controlled by the 2G Long Core software (Core Logic, version Leg207.3). All remanence data during Expedition 304 were corrected for baseline drift. During Expedition 305, this option in the Core Logic program was inadvertently deselected and, therefore, most remanence measurements were not corrected for baseline drift.

With strongly magnetized materials, the maximum intensity that can be reliably measured is limited by the slow rate of the sensors (i.e., the number of flux counts must return to zero after the measurement). At the slowest track velocity (1 cm/s), it was possible to measure archive halves with a magnetization as high as  $\sim 10$  A/m. Where even this slowest measurement speed still resulted in residual counts, the data were nonetheless archived because they provide some indication of the magnetization. During Expedition 304, archive halves were measured at variable track velocities (typically 1 cm/s for the initial steps and increased velocities up to 10 cm/s after the remanence had been sufficiently demagnetized). During Expedition 305, archive halves were measured at a constant velocity of 2 cm/s. Although both methods minimize the number of residual flux counts, some core sections had residual flux counts. All data were nonetheless archived because they provide some indication of the magnetization. Some caution is therefore warranted in using the archive half core data from strongly magnetized intervals.

The response functions of the SQUID sensors have a full width of  $\sim 10$  cm at half height so that data within 5 cm of piece boundaries or voids are significantly affected by edge effects. To minimize such spurious data, during Expedition 304 we did not perform measurements within 3–4 cm of a piece end. The data from Expedition 305 included some measurements near piece ends that were removed during reprocessing of the data at the postcruise meeting. Although this approach means that no data are collected for pieces smaller than  $\sim 7$  cm, the time saving allows more detailed measurement or more demagnetization steps elsewhere. Archive halves were typically measured at an interval of 2 cm. This sampling interval coincides with that used on the MST (see “[Physical properties](#)”) so that susceptibility and remanence data may easily be compared. A standard 2.5 cm diameter minicore sample or a  $\sim 9$  cm<sup>3</sup> cube (physical property samples) was generally taken from each 4.5 m cored interval for shipboard study. These

discrete samples were chosen to be representative of the lithology and alteration mineralogy, and an effort was made to utilize samples for which geochemical and physical properties were also measured. The remanence of discrete samples was also measured using the 2G SQUID magnetometer. Because remanent intensities may vary by several orders of magnitude, all discrete samples were spaced 34 cm apart to effectively eliminate any contamination of one measurement from the signal of a neighboring sample. As noted in the Leg 209 “Explanatory Notes” chapter (Shipboard Scientific Party, 2004), the SQUID sensors and sample tray are not perfectly aligned. A variety of discrete samples were measured in multiple positions to establish the angular difference between these coordinate systems, following the procedures described in the Leg 209 *Initial Reports* volume (Shipboard Scientific Party, 2004). A counterclockwise rotation of  $\sim 7^\circ$  about the z-axis produced a small improvement in the clustering of remanence directions of discrete samples measured in three positions (such that the magnetization component parallel to each of the sample coordinate axes was measured once with each SQUID sensor). However, we elected not to apply this correction for the following reasons: (1) the mean direction of magnetization of the discrete samples calculated from the three-position data was not significantly different from that obtained prior to rotation of the tray, (2) declinations of archive half data are unconstrained and are therefore not affected by rotation about the z-axis, and (3) no directional standards were available to directly test the accuracy of the above rotation. The three-position measurement scheme effectively corrects for the angular difference in SQUID sensor and sample tray coordinate systems and was therefore adopted for all thermally demagnetized and most AF-demagnetized discrete samples during Expedition 304. Many AF-demagnetized samples during Expedition 305 were also measured using this protocol.

Discrete samples were subjected to stepwise AF demagnetization using a DTech (model D-2000) AF demagnetizer capable of peak fields up to 180 mT. At peak fields  $>40$  mT, samples were typically demagnetized and measured twice (once after demagnetization along the sample +x-, +y-, and +z-directions and again after demagnetization along the -x-, -y-, and -z-directions) to identify and compensate for any bias field in the demagnetizing coil. Many samples, particularly during Expedition 305, were thermally demagnetized by the Schonstedt Thermal Specimen Demagnetizer (model TSD-1). Sufficient stepwise AF or thermal demagnetizations were performed to isolate characteristic remanent magnetization components and to quantify magnetic over-

prints. Characteristic directions were fit using principal component analysis (Kirschvink, 1980).

In addition to standard paleomagnetic measurements, the anisotropy of magnetic susceptibility (MS) was determined for most discrete samples using the Kappabridge KLY-2 (Geofyzika Brno) and a 15-position measuring scheme. The susceptibility tensor and associated eigenvectors and eigenvalues were calculated offline following the method of Hext (1963). All bulk susceptibility values (as well as remanent intensities) reported for discrete samples from Expedition 304 have been corrected for the true cylindrical or cubic sample volume. During Expedition 305, remanent magnetization and volume susceptibilities are based on a nominal core volume of 10 cm<sup>3</sup>. For a small number of samples, the anisotropy of anhysteretic remanent magnetization (ARM) was also determined. For each of the sample axial directions (i.e., +x, +y, and +z and -x, -y, and -z), the remanence after a baseline AF demagnetization step (parallel to the subsequent ARM direction) was measured and subtracted from the axial ARM. The remanence anisotropy tensor was then calculated in a manner analogous to that used for the susceptibility tensor.

## Physical properties

Shipboard measurements of physical properties were used to characterize recovered rocks for correlating cored material with downhole logging data and interpreting broader scale geophysical and geological data.

After recovery, the cores were allowed to come to approximately room temperature (22°–25°C), and then MS, noncontact electrical resistivity (NCR), gamma ray attenuation (GRA) bulk density, and natural gamma radiation (NGR) were measured in a series of nondestructive tests on whole cores in split liners in the MST. The bulk of Expedition 304 and 305 cores were collected with the RCB. RCB cores of hard rock are rarely full diameter, so GRA density, MS, and NGR, being rock volume dependent, are underestimated. No corrections have been applied to correct for volume variations. *P*-wave velocity (using the *P*-wave logger) was not measured on the MST, which requires full-diameter core and adequate coupling to the liner for velocity to be measured effectively. Thermal conductivity was measured nondestructively on the archive half of split core pieces. Measurements of *P*-wave velocity, bulk and grain density, and porosity were made mostly on 1 inch diameter minicores (Expedition 304) and ~9 cm<sup>3</sup> cubes (Expedition 305) cut from the working half of the split core. When appropriate, these samples were also used for paleomagnetic measurements. The samples

chosen for physical property measurements were generally representative of the main lithologic units and avoided veins, large phenocrysts, and so on. However, some end-member lithologies were selected for measurement. All the physical property methods except for electrical resistivity measurement are described by Blum (1997).

## Nondestructive sample experiments

NCR, MS, and NGR measurements were made on the MST. At the start of Expedition 304, it was thought that resistivity and susceptibility could not be measured simultaneously, so they were measured on separate runs for Hole U1309B and the upper 130 m of Hole U1309D. Below 130 m in Hole U1309D and during Expedition 304, NCR and MS were measured concurrently. During Expedition 305, NCR, MS, NGR, and GRA were all measured. The MST limitation was actually found to be a function of the number of instruments (a maximum of four) that can be connected to the Integrated Measurements System data acquisition program at any one time. It should be noted that the calibrations assumed for the logged MST measurements of MS, GRA, and NGR assume normal full-diameter RCB core, so although the use of nonstandard sample geometries for other core types will give useful relative data, these will not be absolute measurements and will need to be corrected prior to comparison with measurements from other core types and laboratories. At present, NCR data are logged as instrument output in volts but are stored in the database in millivolts. Similarly, MS data are stored in instrument units (IU). Although major voids were skipped, it was impractical to avoid measuring small or partly broken rock pieces. In these cases, the measurements were not properly calibrated and should be ignored. Although it is appreciated that GRA density has little quantitative value during hard rock drilling expeditions, it nevertheless is a useful guide to defining density trend. GRA density also has a practical application, in that rapid decreases in GRA density can be used to map the location of breaks along the core. MST data were sampled at discrete intervals, with sampling intervals and NGR count times chosen to optimize the resolution of the data in the time available to run each section through the device (Table T11).

## Electrical resistivity

Resistivity was measured using a noncontact inductive instrument, purpose-built for the MST by Geotek. The instrument transmits a high-frequency electromagnetic signal from one coil near the sample. This induces currents in a conducting sample, which in turn produces a secondary electromagnetic

field that is detected by a receiver coil, also near the sample. A matched pair of transmitter and receiver coils points away from the sample and provides a null reference. The instrument measures the difference in signal received at the sample and reference coils. This difference in signal is a function of the resistivity of the sample. The instrument is rated to measure resistivity in the range of 0.1–10  $\Omega\cdot\text{m}$ . Apparently useful measurements to  $>10^5 \Omega\cdot\text{m}$  were obtained, but these high values are poorly calibrated. The indication of a variation in resistivity is reliable in these cases, but the measured magnitude of the change cannot be used for interpretation.

The Geotek instrument, originally fixed to the bench with Velcro, showed improved accuracy after a more permanent attachment with bolts. The instrument's automatic zeroing was checked at the beginning of each run.

Calibration of the NCR at the beginning of Expedition 304 was conducted by measuring 13–15 cm lengths of core liner filled with several different but known concentrations of NaCl solution in water, ranging from 0.35 ppt (0.006 mol/L) to 35 ppt (0.599 mol/L). The resistivities of these standards were obtained from data provided by Geotek (Figs. F13, F14). The resulting calibration formula is

$$R = 0.0638 V^{-1.1806},$$

where  $R$  is resistivity in ohm-meters and  $V$  is instrument output in volts. This formula was used for both Expeditions 304 and 305. Note that, at present, only the raw voltage values (mV) are logged in the IODP database, although for this report, the NCR data are presented in SI units based on the formula shown above. It is sometimes more intuitive to consider the reciprocal of resistivity, which is conductivity (NCC), measured in Siemens per meter (S/m).

The manufacturer, Geotek, estimates the spatial resolution of the NCR as ~2 cm. However, note that Figure F13 shows that the sensor has to be between 4 and 8 cm from the end of the sample before the full resistivity is measured; therefore, resistivity measured on pieces shorter than ~10 cm will be overestimated. NCR was measured every 2 cm along the core.

Except in cases where a rock contains large quantities of conducting minerals (mostly metal oxides and sulfides), electrical resistivity is determined by the amount and conductivity of the pore fluids in the rock, the geometry of the pore space, and the degree of alteration (e.g., Ildefonse and Pezard, 2001). As such, the degree of saturation with seawater is critical. Normally, resistivity was measured on the MST ~2 h after the core came on board (the delay being the time required for core curation), and in this time,

the core can lose a significant proportion of its pore water. This dependency was investigated during drilling Hole U1309D by measuring one interval (Core 304-U1309D-38R, second uncurated liner; eventually Section 2 and part of Section 3) ~15 min after coming on board and again ~2.5 h later, after curation. The results (Fig. F15) show broadly the same trends but with differences in signal level that are summarized in Table T12. The nonlinearity of the relation between volts and resistivity and the fact that a few measurements in the 2.7 h run are quite low lead to a large standard deviation in resistivity. To reduce the large resistivity standard deviation, the test was repeated on two long pieces of core sections (Core 304-U1309D-36R-1 [Pieces 2 and 3]) from Hole U1309D lithologic Unit 88, oxide-bearing gabbros, which were relatively conductive. The working and archive halves were put together (and held in place by elastic bands) and then were remeasured dry and after saturation in seawater for periods from 2.5 to 17.7 h. The results were inconclusive (Fig. F16), and, therefore, the absolute values of conductivity should be considered “apparent” and not a direct measure of the rock properties.

### Magnetic susceptibility

Magnetic susceptibility,  $k$ , is a dimensionless measure of the degree to which material can be magnetized in an external magnetic field:

$$k = M/H,$$

where  $M$  is the magnetization induced in the material by an external field of strength  $H$ . MS is sensitive to variations in the type and concentration of magnetic grains in rocks and is therefore an indicator of compositional variations.

The MST includes a Bartington susceptibility meter (model MS2C) with an 8 cm internal diameter loop sensor, which corresponds to a coil diameter of 88 mm, and operates at a frequency of 0.565 kHz with an AF intensity of 80 A/m (Bartington Instruments, Ltd., 1995). The instrument output is in volume-specific IU. For a core diameter of 66 mm and a coil diameter of 88 mm, the correction factor is 1.48 [transforming volume-specific IU to absolute SI units ( $\times 10^{-5}$ )] (Blum, 1997). Note that because RCB and other coring procedures yield core with diameters <66 mm, the IODP database stores MS in IU.

The instrument is automatically zeroed before the sample is introduced, and a control measurement is made at the end of each run to enable correction for an assumed linear drift. The instrument can be calibrated using a standard sample of known susceptibility (e.g., a sample of known magnetite content) (Fig. F17). During Expeditions 304 and 305, RCB cores

were sampled at 2.0 cm intervals. Measurement precision is  $2 \times 10^{-6}$  SI, and along-core resolution is  $\sim 4$  cm (Fig. F17). Note that susceptibility measured on pieces shorter than  $\sim 8$  cm is underestimated.

On the Bartington MS2C sensor, all readings  $>10,000$  IU lose the most significant digit, so the signal appears to fall discontinuously to a low value or “wrap around.” As a result, intervals where  $k$  values appear to approach 0.1 and then fall rapidly should be examined and used with care. For example, Section 304-U1309D-36R-1 in Unit 88 (oxide gabbros) shows a noisy signal, rapidly varying from very low to full range (Fig. F18). However, application of an arbitrary additive constant of either 10,000 IU or 20,000 IU (one or two times full range) makes the susceptibility signal much less noisy and better correlated with the electrical conductivity signal. In principle, it is not possible to determine a priori the additive factor to reconstruct the MS reliably. Although Figure F18 summarizes the MS problem and offers a possible solution, no attempt was made to routinely correct the MS data shown in this report or in the IODP database.

As stated above, for sufficiently small rock pieces, the measured susceptibility amplitude will be inaccurate and should be ignored.

Another instrument, the MS2E1 point sensor, is also available for measuring susceptibility on split core (on the archive MST [AMST]) (Blum, 1997). This apparently has the same characteristics as the Bartington MS2F (Bartington Instruments, Ltd., 1995) but has almost 1 order of magnitude better spatial resolution ( $<1$  cm) than the MS2C loop sensor (4 cm) on the MST. The point susceptibility track automatically scans the core profile with a laser to sense voids, but simply observing the operation of the device indicates that, often, core spacers are measured, so care should be taken in selecting AMST data for use or comparison with the MS data. Samples were measured on the point sensor every 2 cm along the core.

MS was measured both on the MST (MS2C sensor) and on the AMST (MS2E1 point sensor). The results from the two sensors are moderately well correlated, but the MS2E1 produced values  $\sim 70\%$  lower than those of the MS2C (Fig. F19), confirming that the approximate volume correction for the MST is often valid for hard-rock core. MS was also compared with the MS of discrete samples measured using the MS2E1 point sensor with values measured on the Kappabridge susceptibility meter in the paleomagnetism laboratory (Fig. F20). These show a good correlation with a slope of 0.57. Note that, according to the manufacturer, the MS2E1 sensor will read  $\sim 0.5$  times the true susceptibility when placed against a flat surface, or 1.0 times the susceptibility “when

buried up to the shoulder” (Bartington Instruments, Ltd., 1995).

For this report and in the VCDs (Fig. F2), only MST data from the MS2C sensor are displayed.

### Natural gamma radiation

NGR was logged on the MST using a 30 s counting period at 10 cm intervals. The NGR sensor was built by ODP in 1993 and uses four NaI scintillation counters arranged at  $90^\circ$  to each other in a plane normal to the core axis. Activity was measured in total counts per second with no attempt to determine energy spectra. At background level, a count at 30 cps measured over a 30 s period gives a statistical error of  $\sim 3\%$ . The device was calibrated for zero background by measuring a core liner filled with distilled water. Initial software problems with NGR data logging (a Y2K program bug that had only just manifested itself) resulted in no NGR measurements being made during Expedition 304 on Hole U1309B or Cores 304-U1309D-1R to 22R. However, if Expedition 305 is an indication, the NGR measurements never significantly exceeded background levels.

### Thermal conductivity

Thermal conductivity was measured on the archive half of the split core. This was achieved by transient heating of the sample with a known heating power generated from a source with finite radius and assumed infinite length and infinite thermal conductivity (in practice, a 7 cm long needle). The needle probe method was used in half-space mode (Vacquier, 1985) to measure thermal conductivity in pieces of the split core taken from the archive half. The increase in temperature with time was measured using the TK04 system described by Blum (1997), and the best-fit parameters to this curve are automatically determined by the instrument, leading to an estimate of the thermal conductivity. In theory, the changing temperature should be logged for an infinite time. In practice, by fitting different portions of the curve, a series of estimates of the equilibration time is obtained together with the corresponding thermal conductivity. The minimum equilibration time and maximum standard deviation for acceptable curve fits are set to 10,000 s and  $0.003$  W/(m·K). Four separate runs are made on each sample, and the mean is logged. The standard deviations between the four measurements were typically  $\sim 0.1$  W/(m·K). The instrument performs a self-test at the beginning of each measurement and does not need calibration. Precision has been estimated as 2%, with an accuracy of 5% (Blum, 1997).

Samples were taken at irregularly spaced intervals (typically  $\sim 1$ – $3$  samples per core, or average intervals

of 1.5–3 m), depending on the availability of pieces long enough to be measured without edge effects (more than ~10 cm) and on the degree of lithologic variability. Samples needed to be quite smooth to ensure adequate contact with the heating needle; in practice, this usually meant removing any visible saw marks, and this was achieved by grinding and polishing the rock using 120 gauge silicon carbide powder. Samples were allowed to equilibrate to room temperature for at least 4 h, and then they and the sensor needle were equilibrated together in a seawater bath (enclosed within a cooler during Expedition 305) for at least 15 min prior to measurement. Isolation of the samples and sensor needle in the cooler eliminated the effect of rapid but small temperature changes introduced by the laboratory air conditioning, opening of nearby bulkhead doors, and people walking past the experiment. The instrument measures the thermal drift and will not begin a heating run until sufficient thermal equilibrium is attained. Measurements were made at room pressure and temperature and were not corrected for in situ conditions.

Thermal conductivity is an intrinsic tensor material property that depends on porosity, density, mineral composition, and fabric. Most known single-crystal thermal diffusivities are anisotropic (e.g., Kobayashi, 1974; Tommasi et al., 2002). Therefore, thermal conductivity might be expected to be anisotropic if the samples are monomineralic or if the sample is dominated by a fabric. To test for thermal conductivity anisotropy, Hole U1309B archive pieces were analyzed by taking three measurements on the cut face: one ( $k_0$ ) parallel to the core and two ( $k_1$  and  $k_2$ ) at angles of approximately  $\pm 35^\circ$  to the core axis (Fig. F21), these being the largest angles that can be achieved without encountering serious edge effects. An estimate of the anisotropy of thermal conductivity is then defined as

$$[\max(k_0, k_1, k_2) - \min(k_0, k_1, k_2)] / \text{mean}(k_0, k_1, k_2),$$

irrespective of which component was maximum. The same definition was used during Leg 209 (Shipboard Scientific Party, 2004). Note that this is only an apparent anisotropy, as it is not based on orthogonal measurements.

Each of the measurements made at  $0^\circ$  and  $\pm 35^\circ$  to the core axis consisted of four measurements (as described above) that were averaged to obtain a single data point. The standard deviation for these four measurements, averaged over all the Hole U1309B data points, is 0.08–0.09 W/(m·K), and only two data points (both in apparently isotropic basalts) had individual standard deviations  $>0.12$  W/(m·K). The maximum difference between the  $0^\circ$ ,  $+35^\circ$ , and  $-35^\circ$  measurements, averaged over all the Hole U1309B

data points, is 0.1 W/(m·K). It was concluded that, during Expedition 304, it was not possible to detect any significant anisotropy of thermal conductivity within the precision of the measurements. Thus, for Hole U1309D, measurements were made with the needle probe parallel to the core axis. Exceptions were made when the sample was too short or when it was necessary to avoid features such as veins. Rarely, when a strong lineation or foliation was present, measurements would be made as nearly parallel and perpendicular to that direction as possible.

Thermal conductivity has also been measured on gabbros and peridotites recovered from Legs 118 (Robinson, Von Herzen, et al., 1989), 147 (Gillis, Mevel, Allan, et al., 1993), 153 (Cannat, Karson, Miller, et al., 1995), 176 (Dick, Natland, Miller, et al., 1999), and 209 (Kelemen, Kikawa, Miller, et al., 2004). Except for Legs 176 and 209, these data were acquired with the Thermcon-85 system, which was replaced on board the *JOIDES Resolution* by the TK04 system in 1996 (ODP Leg 168). The latter probably gives more accurate and more consistent results, as the new measurement technique is less user-dependent than the older one (Blum, 1997).

### Discrete sample experiments

Minicores (Expedition 304) and cubes (Expedition 305) were cut from the working halves of split cores. As with thermal conductivity measurements, material was taken at irregular intervals in an attempt to sample variations in the characteristic or representative core lithology. Their precise positions depended on the suitability of core, attempting to avoid extremely brittle zones. The average sampling rate was ~1–2 samples per core. After cutting, the samples were saturated for 24 h under a vacuum of  $-100$  kPa. The saturated samples were then removed and wet weighed, and velocities were measured. The wet volumes of the cube samples were estimated using a caliper to measure the length of each side to 0.01 cm. Using a caliper to define wet volume for Expedition 305 cubes translated to an error of  $0.018 \pm 0.001$  g/cm<sup>3</sup>. Samples were then placed into a dry oven at  $105^\circ \pm 5^\circ\text{C}$  for another 24 h period. After removal from the oven, samples were placed in a desiccator and allowed to cool to room temperature. Finally, dry weight and dry volume were measured.

### P-wave velocity

The *P*-wave sensor (PWS3) (Hamilton Frame method) was used to measure velocities in discrete samples of the materials recovered during Expeditions 304 and 305. For Expedition 304, samples were usually 1 inch diameter minicores from the working half of the split core, drilled along the x-axis of the

core normal to the split face, although occasionally, irregularly shaped pieces were used where a minicore could not be taken. For Expedition 305, cubes cut from the working half of the split were used for horizontal (x- and y-direction) and vertical (z-direction) *P*-wave velocity, porosity, and density measurements.

The PWS3 is a modified and updated version of the classic Hamilton Frame velocimeter, designed with one transducer fixed and the other mounted on an adjustable screw. The PWS3 is mounted vertically to measure velocities perpendicular to the core axis by placing the sample on the lower transducer and bringing the upper transducer into direct contact with the upper surface. Transducer separation was measured by a digital caliper attached to the transducers. At the beginning of Expedition 304, the lower transducer head was not adequately attached to the bottom mounting, so the mount was reinforced following the completion of Hole U1309B. Hole U1309B samples were remeasured and showed an average increase in velocity of  $0.2 \pm 0.2$  km/s. The new values are used in this report and included in the database.

Traveltime was determined automatically using shipboard software that picked the time when the observed waveform exceeded a preset proportion of the maximum background amplitude. However, the picked time was visually seen to be later than would normally be picked by hand (Fig. F22). The arrival time was initially picked manually, but this approach was eventually abandoned for the automatic method to maintain consistency between operators. The automatic method was used for all the Expedition 304 and 305 velocity measurements reported and entered into the IODP database.

For Expedition 304, to ensure that the measured sample length corresponded accurately to the path traveled by the acoustic pulse, the end of each minicore farthest from the split face was first ground flat and parallel to the opposite face using 120 gauge silicon carbide grit with the aid of a purpose-made handheld frame. Early measurements made without this step showed poor accuracy and repeatability. When the sample was placed between the PWS3 transducers, distilled water was applied between the top and bottom of the sample and transducer heads to improve acoustic coupling (i.e., the impedance match) between the transducer and the sample. For Expedition 305 cube samples, no polishing or silicon grit was used but deionized water was used to achieve a better coupling with the transducers.

The instrument was calibrated in port and at various times throughout the expedition by measuring traveltimes over samples of different thicknesses and

known velocity and determining the measured velocity by linear regression. The estimated precision is  $\sim 0.1$  km/s.

*P*-wave anisotropy between the average horizontal and vertical velocities and horizontal anisotropy were calculated using

$$[\text{mean}(V_x, V_y) - V_z] / \text{mean}(V_x, V_y, V_z)$$

and

$$(V_x - V_y) / \text{mean}(V_x, V_y),$$

respectively, where *x*, *y*, and *z* are the standard core coordinate axes,  $V_x$  and  $V_y$  are the transverse core velocities, and  $V_z$  is the longitudinal core velocity. During Expedition 304, it proved difficult either to reliably measure velocities along the minicore axis or to accurately cut cubes with sufficiently parallel faces. The parallel-blade rock saw was serviced and blades were replaced for successful cube preparation during Expedition 305. The PWS3 was used to measure each direction (*x*, *y*, and *z*) of the cubes, which were marked during sampling with an arrow pointing up-core in the *z*-direction on the *x*-direction face.

### Porosity and density

The samples used for velocity measurements were also used to estimate bulk density, grain density, and porosity from the wet weights, dry weights, and dry volumes of the samples. The density and porosity values were determined automatically by IODP programs that convert the mass and volume measurements using the method described below. Results were then uploaded to the database.

Sample mass was determined to a precision of  $\pm 0.001$  g using two Scientech electronic balances. The balances are equipped with a computer averaging system that compensates for the motion of the ship. The sample mass on one balance is counterbalanced by a known mass on the adjacent balance. The balances were calibrated in port prior to each expedition by weighing known masses. Continuing problems with the weight measurement forced recalibration of the balances to be done at sea.

The volumes of chips, minicores, and cubes were determined using a five-cell Quantachrome helium-displacement pycnometer with a nominal precision of  $\pm 0.01$  cm<sup>3</sup>. Calibration was maintained by including a standard reference sphere in one of the operating cells for each run and cycling it sequentially between the cells for successive runs. The cell volumes were recalibrated if the measured volume of the standard was not within 0.02 cm<sup>3</sup> of the known volume of the standard. Early in Expedition 304, it was found that Cell 4 did not operate correctly, and all subsequent runs were made without this cell. During Expedition 305, due to technical difficulties, the

computer-compatible pycnometer had to be replaced by an older, manual pycnometer calibrated for use with medium-sized cells (as opposed to the beaker-compatible cells used for Expedition 304).

Wet weight was determined on samples that had been saturated in seawater under vacuum for 24 h. Samples were lightly patted dry on paper towels to remove excess water adhering to the surface before weighing. Dry weight and pycnometer volume measurements were then made after the samples had been oven dried for 24 h and allowed to cool in a desiccator. A potential problem with this drying temperature is that, in addition to interstitial water, chemically bound water in some clay minerals can be lost, leading to porosity errors up to 20% (Blum, 1997). This is not considered to be a problem for the gabbros, troctolites, and diabases recovered during Expeditions 304 and 305.

### Water content

Water content, as a fraction of total mass or as a ratio of water mass to solid mass, is determined by standard methods of the American Society for Testing and Materials designation 2216 (ASTM, 1989). Sample saturation in seawater was done under vacuum for a 24 h period. The total water-saturated mass ( $M_b$ ) and dry mass ( $M_d$ ) are measured using the electronic balance as described above, and the difference is the uncorrected water mass. Measured wet and dry masses are corrected for salt assuming a pore water salinity ( $s$ ) of 0.035 (Boyce, 1976). The water contents expressed as a percentage of the wet mass or the dry mass ( $W_b$  and  $W_s$ , respectively) are given by

$$W_b (\%) = 100[(M_b - M_d)/([1 - s]M_b)]$$

and

$$W_s (\%) = 100[(M_b - M_d)/(M_d - sM_b)].$$

### Bulk density

Bulk density ( $b$ ) is the density of the saturated sample,

$$b = M_b/V_b,$$

where  $M_b$  = the total water-saturated mass and  $V_b$  = the total sample volume. The latter is estimated either from the dimensions of the sample or from the volume of the dry sample ( $V_d$ ) measured in a helium gas pycnometer and the volume of the pore fluid ( $V_{pw}$ ):

$$V_b = V_d + V_{pw}.$$

### Grain density

Grain density ( $g$ ) is determined from the dry mass and dry volume measurements. Both mass and vol-

ume must be corrected for the salt content of the pore fluid:

$$g = (M_d - M_{salt})/(V_d - M_{salt}/salt),$$

where  $M_d$  = the dry mass of the sample (in grams),  $salt$  = the density of salt (2.257 g/cm), and

$$M_{salt} = s(M_b - M_d)/(1 - s)$$

is the mass of salt in the pore fluid.

$M_{pw}$  is the salt-corrected mass of the seawater:

$$M_{pw} = (M_b - M_d)/(1 - s),$$

and the density of the pore fluid, which is assumed to be seawater, is  $pw = 1.024$  g/cm.

Then the volume of pore water is

$$V_{pw} = M_{pw}/pw = (M_b - M_d)/(1 - s)pw.$$

Alternatively, the grain density is calculated from the wet and dry masses ( $M_b$  and  $M_d$ ) and the sample volume ( $V_b$ ) is calculated from the measured dimensions of a minicore or cube sample:

$$g = (M_d - M_{salt})/[(1 - s)pw/(M_b - M_d)].$$

### Porosity

Porosity ( $\phi$ ) is the ratio of pore water volume to total volume and can be calculated from fluid density, grain density, and bulk density of the material:

$$\phi = 100[(g - b)/(g - w)],$$

where

$g$  = the grain density,

$b$  = the bulk density, and

$w$  = the fluid density.

### Dry density

The dry density ( $d$ ) is the ratio of the dry mass ( $M_d$ ) to the total volume ( $V_b$ ). The dry density is calculated from the corrected water content ( $W_d$ ) and porosity ( $\phi$ ):

$$d = (\phi/W_d)w.$$

## Microbiology

An analysis of the microbial populations present in the subsurface biosphere at Atlantis Massif was undertaken during Expeditions 304 and 305. The goal for these microbiological analyses is to characterize the endolithic microbes associated with the oceanic core complex via culture-dependent and culture-independent methodologies. Throughout each expedition, an effort was made to establish a culture collection of microbes that interact with the various lithologies recovered. Upon completion of both expeditions, molecular analyses will be carried out on cultures, as well as on rock samples, to identify

the microbes present in the various igneous rock samples from Atlantis Massif.

### Sampling procedures

Upon arrival in the core laboratory, a section of the core was evaluated as a potential microbiological sample by visual inspection with minimal handling using ethanol-rinsed gloves. The core segment of interest was putatively identified, photographed, and placed in a sterile plastic bag. The core was then transferred to an anaerobic hood, where all subsequent manipulations were performed.

### Contamination

To determine the extent of contamination from drilling fluid, 0.5  $\mu\text{m}$  fluorescent microspheres (Expeditions 304 and 305) and perfluorocarbon tracer (PFT; Expedition 304 only) were deployed with each core barrel intended for microbiological sampling (for details, see Smith et al., 2000). PFT was metered into the drilling fluid during coring operations, and samples were collected from the outside of the core to ensure delivery of the tracer and from the inside of the core to determine the extent of PFT infiltration into the sample. To determine whether the PFT reached the core, the surface of the whole-rock piece (~10 cm) was washed with filtered seawater. This rinse water was then placed into a vial and immediately sealed. Subsamples from the exterior and interior of each rock sample were crushed, placed into a vial, and immediately sealed.

Fluorescent beads were deployed in a plastic bag wedged into the core catcher that likely ruptured as the first cored material entered the core barrel. Beads on the outside of the core indicate dispersion of the microspheres on the external portion of the core; beads detected on the interior of the core indicate the presence of permeable pathways in excess of 0.5  $\mu\text{m}$  in width, suggesting that contamination of the interior of the core may have occurred.

Each core collected was rinsed, and this rinse water was then assessed via microscopy (Zeiss Axiophot) to ensure that microspheres were dispersed. Contamination of the interior of the core was determined by the presence or absence of microspheres.

To further constrain the degree of contamination of cores, water samples were obtained using a sterile Water Sampling Temperature Probe (WSTP). The WSTP water collection device was initially flushed with distilled water and then sterilized with a (10% v/v) bleach solution that remained in the tool for 0.5 h. The tool was then rinsed with nanopure water. Approximately 5 mL of seawater was collected and immediately frozen at  $-80^{\circ}\text{C}$ . A comparison of sea-

water microorganisms present in the water samples to the microbes identified via a molecular analysis in the interior portions of core samples will determine the extent of contamination by seawater microorganisms.

### Cultivation experiments

#### Expedition 304

Anaerobic cultivation experiments targeted a broad physiological spectrum of chemoautotrophic and chemoorganotrophic microorganisms that may utilize energy sources from the deep oceanic crust. To verify that microspheres were dispersed during drilling operations, the exterior of the core (~10 cm) was washed with 50 mL of filtered seawater. Seawater remaining on the exterior of the rock surface was removed with paper. The core sample, which was wrapped in plastic, was split by means of a hydraulic rock splitter. The interior portions of the core were then crushed using a sterile mortar and pestle, and ~1  $\text{cm}^3$  of sample was used as the inoculum. Each culture bottle contained 10 mL of media to enrich for chemoautotrophic microbes. Following inoculation culture, vessels were sealed with butyl rubber stoppers.

For sediment samples, ~0.5 mL of sediment was used as the inoculum in three different types of anaerobic media: methanogen enrichment media, sulfate-reducing bacteria media, and media to enrich for organic-matter-utilizing microbes. The culture bottles for methanogen enrichment media and sulfate-reducing bacteria media were incubated at  $5^{\circ}$ ,  $37^{\circ}$ ,  $65^{\circ}$ , and  $85^{\circ}\text{C}$ . The culture bottles for the enrichment of organic-matter-utilizing microbes were incubated at  $37^{\circ}$  and  $65^{\circ}\text{C}$ . Cell counts of in situ cell densities as well as determination of cell densities in cultures were performed with 4',6-diamidino-2'-phenylindole-dihydrochloride, a nucleic acid stain.

Molecular studies based on 16S ribosomal ribonucleic acid gene sequence information, including polymerase chain reaction amplification, will be part of a postcruise research program. In addition, on-shore investigations will address the potential metabolic activity of microbial populations and micro-scale observations of sulfide, phosphate, graphite, and stable isotope compositions to determine the impact of biomineralization.

#### Expedition 305

In the anaerobic hood, the core was first rinsed with 300 mL of nanopure water to collect a sample from the exterior of the core to confirm that microspheres were dispersed during drilling. The core sample was then broken into two sections using a hydraulic rock

splitter with sterile blades. One section of the core sample was immediately frozen at  $-80^{\circ}\text{C}$  for shore-based molecular analysis. The exterior portions of the remaining core section were removed, and interior pieces, manipulated with sterile forceps, were crushed using a sterile mortar and pestle.

Approximately  $2\text{ cm}^3$  of sample was used as the inoculum in four different types of anaerobic media: artificial seawater media amended with nitrate, artificial seawater amended with lactate and overpressured with hydrogen, natural seawater with no amendments, and methanogen enrichment media. Cultures were established in anaerobic culture tubes, and all media, except for methanogen enrichment media, contained 5 g of sterile fine-fraction olivine derived from crushed dunite. Samples from the depths of 400–800 mbsf were incubated at  $20^{\circ}$  and  $30^{\circ}\text{C}$ . The sample from 400 mbsf was also incubated at  $50^{\circ}\text{C}$ . Samples from the depths of 900–1100 mbsf were incubated at  $30^{\circ}$  and  $60^{\circ}\text{C}$ . Finally, samples from the depths of 1200–1400 mbsf were incubated at  $60^{\circ}$  and  $90^{\circ}\text{C}$ .

Approximately  $5\text{ cm}^3$  of inner core material from several samples was placed in 25 mL of sterile artificial seawater media. A 50  $\mu\text{L}$  aliquot of this was spread onto marine agar 2216, R2A agar, artificial seawater, and natural seawater agar plates. Plates were incubated at  $30^{\circ}\text{C}$  and monitored for colony formation.

Following inoculations, 6 mL of paraformaldehyde (4% w/v) and 600  $\mu\text{L}$  of sodium pyrophosphate (0.1M) were added to the remaining interior core material, which was then agitated for 3 h on a vortexer to detach cells from rock material. After vortexing, samples were stored for 12 h at  $4^{\circ}\text{C}$  and subsequently stained with a 0.2  $\mu\text{m}$  filter-sterilized acridine orange (0.01% w/v) solution that absorbs wavelengths of 440–480 nm. Samples were then filtered onto a 0.2  $\mu\text{m}$  filter and examined using epifluorescence microscopy and brightfield illumination to determine in situ cell densities.

Samples inoculated with core material were monitored for growth via change in liquid media turbidity. An increase in turbidity of liquid media is a potential indicator for an increase in cell density. Cultures that appeared more turbid with time were subsampled (240  $\mu\text{L}$ /sample) and fixed with 50  $\mu\text{L}$  of 0.2  $\mu\text{m}$  filter-sterilized 10% paraformaldehyde. Samples were then stained with 15  $\mu\text{L}$  of acridine orange and examined using epifluorescence microscopy.

## Downhole measurements

Downhole wireline logs are spatially continuous records of the in situ physical, chemical, and struc-

tural properties of the formation penetrated by a borehole. They provide information on a scale that is intermediate between laboratory measurements on core samples and geophysical surveys. The logs are recorded rapidly using a variety of probes or sondes combined into tool strings (Table T13). These tool strings are lowered downhole on a heave-compensated electrical wireline and raised at a constant speed (typically 250–300 m/h) to provide continuous simultaneous measurements of various properties as a function of depth. During Expeditions 304 and 305, a main objective of the wireline logging program was to orient faults, fractures, deformation features, and any obvious petrologic boundaries using borehole imaging techniques. Borehole images may then help orient core pieces or sections if the core recovery is sufficiently high. In addition to defining structural features, the logging program also attempts to establish lithologic or physical properties boundaries, as interpreted from logging tool response characteristics as a function of depth, determine serpentinization and/or alteration patterns in basalts and gabbroic and ultramafic rocks, and produce direct correlations with discrete laboratory measurements on the recovered core.

### Tool string configurations and geophysical measurements

Individual logging tools were joined together into tool strings so that several measurements could be made during each logging run (Table T13). The tool strings were lowered to the bottom of the borehole on a wireline cable, and data were logged as the tool string was pulled back up the hole. Repeat runs were made to improve coverage and document the precision of logging data. During Expeditions 304 and 305, up to five different tool strings were deployed (Fig. F23):

- The triple combination tool string, which consists of the Hostile Environment Spectral Gamma Ray Sonde (HNGS), the Dual LateroLog (DLL) tool, the Hostile Environment Litho-Density Sonde (HLDS), and the Accelerator Porosity Sonde (APS) (the Lamont-Doherty Earth Observatory [LDEO] high-resolution Temperature/Acceleration/Pressure [TAP] tool is attached at the bottom of this tool string);
- The Formation MicroScanner (FMS)-sonic tool string, which consists of the FMS, the General Purpose Inclinator Tool (GPIT), the Scintillation Gamma Ray Tool (SGT), and the Dipole Sonic Imager (DSI) tool
- The Ultrasonic Borehole Imager (UBI) tool string, which also includes the GPIT and the SGT

- The three-component Well Seismic Tool (WST-3)
- The Goettingen Borehole Magnetometer (GBM; third-party magnetometer)

The properties measured by each tool, the sample intervals used, and the vertical resolutions are summarized in Tables T13 and T14. Explanations of tool name acronyms and their measurement units are summarized in Table T14. More detailed descriptions of individual logging tools and their geological applications can be found in Ellis (1987), Goldberg (1997), Rider (1996), Schlumberger (1989, 1994), Serra (1984, 1986, 1989), and the LDEO-Borehole Research Group (LDEO-BRG) Wireline Logging Services Guide (1994).

### Natural gamma radiation

Two gamma ray tools were used to measure and characterize natural radioactivity in the formation: the HNGS and the SGT. The HNGS measures the NGR from isotopes of potassium, thorium, and uranium using five-window spectroscopy to determine concentrations of radioactive potassium (in weight percent), thorium (in parts per million), and uranium (in parts per million). The HNGS uses two bismuth germanate scintillation detectors for gamma ray detection with full spectral processing. Corrections to the HNGS log account for variability in borehole size and borehole potassium concentrations. All of these effects are corrected at LDEO-BRG during the expedition. The HNGS also provides a measure of the total gamma ray emission (in American Petroleum Institute [gAPI] units) and the uranium-free or computed gamma ray (in gAPI units). The SGT uses a sodium iodide (NaI) scintillation detector to measure the total natural gamma ray emission, combining the spectral contributions of potassium, uranium, and thorium concentrations in the formation. The SGT is not a spectral tool but provides high-resolution total gamma ray data for depth correlation between logging strings. It is included in the FMS-sonic and UBI tool strings to provide a reference log to correlate depth between different logging runs.

### Density

Density is measured with the HLDS, which consists of a radioactive cesium ( $^{137}\text{Cs}$ ) gamma ray source (622 keV) and far and near gamma ray detectors mounted on a shielded skid, which is pressed against the borehole wall by a hydraulically activated eccentricizing arm (Fig. F23). Gamma rays emitted by the source experience both Compton scattering and photoelectric absorption. Compton scattering involves the transfer of energy from gamma rays to the electrons in the formation via elastic collision. The

number of scattered gamma rays that reach the detectors is directly related to the number of electrons in the formation, which is a function of the bulk density. The HLDS measures the photoelectric effect factor (PEFL) caused by absorption of low-energy gamma rays. Photoelectric absorption occurs when gamma ray energies drop to <150 keV after being repeatedly scattered by electrons in the formation. Because the PEFL depends on the atomic number of the elements in the formation, it is less sensitive to the porosity than the density measurement is. Coupling between the tool and borehole wall is essential for good HLDS logs. Poor contact results in underestimation of density values.

### Neutron porosity

The APS consists of a minitron neutron generator that produces fast neutrons (14.4 MeV) and five neutron detectors (four epithermal and one thermal) positioned at different spacing along the tool. The tool is pressed against the borehole wall by an eccentricizing bow-spring. Emitted high-energy (fast) neutrons are slowed by collisions with atoms, and the amount of energy lost per collision depends on the relative mass of the nucleus with which the neutron collides. Significant energy loss occurs when the neutron strikes a nucleus of equal mass, such as hydrogen. Degrading to thermal energies (0.025 eV), the neutrons are captured by the nuclei of silicon, chlorine, boron, and other elements, resulting in a gamma ray emission. The neutron detectors record both the numbers of neutrons arriving at various distances from the source and the neutron arrival times; these are combined to estimate formation porosity. However, in igneous and altered rocks, in addition to water in pore spaces or fractures, bound hydrogen may also be present in alteration minerals such as clays; therefore, neutron logs may overestimate the porosity. The pulsing of the neutron source provides the measurement of the thermal neutron capture cross section ( $\Sigma$ ) in capture units (cu). This is a useful indicator for the presence of elements of high thermal neutron capture cross section such as boron, chloride, and rare earth elements (Serra 1984).

### Electrical resistivity

The DLL tool provides two resistivity measurements with different depths of investigation: deep and shallow. In both devices, a 61 cm thick current beam is forced horizontally into the formation by using focusing (also called bucking) currents. Two monitoring electrodes are part of the loop that adjusts the focusing currents so that there is no current flow in the borehole between the two electrodes. For the deep laterolog (LLD) measurement, both measuring and

focusing currents return to a remote electrode on the sea surface; this configuration greatly improves the depth of investigations and reduces the effect of borehole and adjacent formation conductivity. In the shallow laterolog (LLS) measurement, the return electrodes that measure the focusing currents are located on the sonde; therefore, the current sheet retains focus over a shorter distance than the LLD. Because of high resistivity expected in an igneous environment, the DLL is recommended over the Dual Induction Tool (DIT), as the DLL tool response ranges from 0.2 to 40,000  $\Omega\cdot\text{m}$ , whereas the DIT response range is 0.2–2,000  $\Omega\cdot\text{m}$ . Fracture porosity can be estimated from the separation between the LLD and LLS measurements, based on the observation that the former is sensitive to the presence of horizontal conductive fractures only, whereas the latter responds to both horizontal and vertical conductive structures.

Because the solid constituents of rocks are essentially infinitely resistive relative to the pore fluids, resistivity is controlled mainly by the nature of the pore fluids, porosity, and permeability. Rock-forming minerals are mostly silicates having a high resistivity ( $10^6$ – $10^{14}$   $\Omega\cdot\text{m}$ ), but when the rock matrix contains conductive minerals (clays and Ti-Fe oxide in gabbros), electrical conduction via electronic processes may be appreciable, as oxides reach resistivity of  $10^{-6}$   $\Omega\cdot\text{m}$  (Olhoeft, 1981; Guéguen and Palciauskas, 1992).

### Temperature/Acceleration/Pressure

The TAP tool is deployed in low-resolution memory mode (4 Hz for accelerometry data and 1 Hz for temperature and pressure), with the data being stored in the tool and then downloaded after the logging run is completed. Temperatures determined using the TAP tool are not necessarily the in situ formation temperatures because water circulation during drilling can disturb temperature conditions in the borehole. From the downhole temperature gradient, however, abrupt temperature changes can be identified that may represent localized fluid flow into the borehole, indicating fluid pathways, fracturing, and/or changes in permeability at lithologic boundaries.

### Acoustic velocities

The DSI tool employs a combination of monopole and dipole transducers to make accurate measurements of sonic wave propagation in a wide variety of formations. The omnidirectional source generates compressional, shear, and Stoneley waves in hard formations. The configuration of the DSI tool also allows recording of both inline and cross-line dipole waveforms. In hard rocks, the dipole sources can re-

sult in a better or equivalent estimate of shear wave velocity to that from a monopole source. These combined modes can be used to estimate shear wave splitting caused by preferred mineral and/or structural orientation in consolidated formations. A low-frequency (80 Hz) source enables Stoneley waveforms to be generated as well. The DSI tool measures the transit times between sonic transmitters and an array of eight receiver groups with 15 cm spacing along the tool, each consisting of four orthogonal elements that are aligned with the dipole transmitters. During acquisition, the output from these 32 individual elements is differenced or summed appropriately to produce inline and cross-line dipole signals or monopole-equivalent (compressional and Stoneley) waveforms, depending on the operation modes. Preliminary processing of DSI data estimates monopole and dipole mode velocities using waveform correlation of the digital signals recorded at each receiver. In most instances, the shear wave data should be reprocessed postcruise to correct for dispersion, which is caused by the variation of sound velocity with frequency.

### High-resolution electrical images

The FMS provides high-resolution electrical-resistivity-based images of borehole walls (Fig. F24). The tool has four orthogonal arms (pads), each containing 16 microelectrodes, or “buttons,” which are pressed against the borehole wall during recording. The electrodes are arranged in two diagonally offset rows of eight electrodes each, spaced  $\sim 2.5$  mm apart. A focused current is emitted from the four pads into the formation, with a return electrode near the top of the tool. Array buttons on each of the pads measure the current intensity variations. The FMS image is sensitive to structure within  $\sim 25$  cm of the borehole wall and has a vertical resolution of 5 mm with coverage of 22% of the borehole wall on a given pass where the borehole is in gauge. FMS logging commonly includes two passes, the images of which are merged to improve borehole wall coverage. The pads must be firmly pressed against the borehole wall to produce reliable FMS images. In holes with a diameter  $>38$  cm (15 inches), the pad contact will be inconsistent and the FMS images can be blurred. The maximum borehole deviation where good data can be recorded with this tool is  $10^\circ$  from vertical. Irregular borehole walls will also adversely affect the images, as contact with the wall is poor. FMS images are oriented to magnetic north using the GPIT. Processing transforms these measurements of the micro-resistivity variations of the formation into continuous, spatially oriented, and high-resolution images that mimic geologic structures behind the borehole

walls. This allows the dip and azimuth of geologic features intersecting the hole to be measured from the processed FMS image. FMS images can be used to visually compare logs with core to ascertain the orientations of layers and fracture patterns. FMS images are particularly useful for mapping structural features, dip determination, detailed core-logging correlation, positioning of core sections with poor recovery, and stress distribution. FMS images have proved to be particularly valuable in the interpretation of volcanic stratigraphy (Ayadi et al., 1998; Lovell et al., 1998; Brewer et al., 1999; Barr et al., 2002) and gabbroic structure (Haggas et al., 2001; Miller et al., 2003) during ODP legs. Further interpretation of FMS images in combination with other logging data and core imaging will be carried out postcruise.

Preliminary structural analysis of the FMS images was completed on board. Conventionally, structural analysis of FMS images is achieved by fitting sinusoidal curves on the unwrapped borehole image. Each planar structure intersecting the borehole wall corresponds to a sinusoid on the FMS images and is indicated by a color distinction. As the borehole image orientation was known, we extracted the azimuth and dip of each plane. The plane azimuth is determined by picking the inflexion point of the sinusoid where the amplitude is half the peak value ( $H$ ). The dip is calculated as  $\tan^{-1}(H/D)$ , with  $D$  being the borehole diameter. FMS data processing and analysis were completed with Geoframe (version 4.0.4.1), Schlumberger software that allows interactive display and analysis of the oriented images.

### Ultrasonic borehole images

The UBI features a high-resolution transducer that provides acoustic images of the borehole wall. The transducer emits ultrasonic pulses at a frequency of 250 or 500 kHz (low and high resolution, respectively), which are reflected at the borehole wall and then received by the same transducer. The amplitude and traveltime of the reflected signal are determined (Fig. F25). A continuous rotation of the transducer and the upward motion of the tool produce a complete map of the borehole wall. The amplitude depends on the reflection coefficient of the borehole fluid/rock interface, the position of the UBI tool in the borehole, the shape of the borehole, and the roughness of the borehole wall. Changes in the borehole wall roughness (e.g., at fractures intersecting the borehole) are responsible for the modulation of the reflected signal; therefore, fractures or other variations in the character of the drilled rocks can be recognized in the amplitude image. The recorded travel-time image gives detailed information about the shape of the borehole, which allows calculation of

one caliper value of the borehole from each recorded traveltime. Amplitude and traveltime are recorded together with a reference to magnetic north by means of a magnetometer (GPIT), permitting the orientation of images. If features (e.g., fractures) recognized in the core are observed in the UBI images, orientation of the core is possible. The UBI orientated images can also be used to measure stress in the borehole through identification of borehole breakouts and slip along fault surfaces penetrated by the borehole (i.e., Paillet and Kim, 1987). In an isotropic, linearly elastic rock subjected to an anisotropic stress field, drilling a subvertical borehole causes breakouts in the direction of the minimum principal horizontal stress (Bell and Gough, 1983).

### Accelerometry and magnetic field measurement

Downhole magnetic field measurements were made with the GPIT. The GPIT is included in the FMS and UBI tool string to calculate tool acceleration and orientation during logging. Tool orientation is defined by three parameters: tool deviation, tool azimuth, and relative bearing. The GPIT utilizes a three-axis inclinometer and a three-axis fluxgate magnetometer to record the orientation of the FMS and UBI images as the magnetometer records the magnetic field components ( $F_x$ ,  $F_y$ , and  $F_z$ ). Corrections for cable stretching, tool sticking, and/or ship heave using acceleration data ( $A_x$ ,  $A_y$ , and  $A_z$ ) allow precise determinations of logging depths.

### Well Seismic Tool

The WST-3 is used to produce a zero-offset vertical seismic profile and/or check shots in the borehole. The WST-3 consists of a three-axis geophone used to record the full waveform of acoustic waves generated by a seismic source positioned just below the sea surface. During Expedition 305, an 80 inch<sup>3</sup> generator-injector air gun, positioned at a water depth of ~2 m with a borehole offset of 50 m on the port side of the *JOIDES Resolution*, was used as the seismic source. The WST-3 was clamped against the borehole wall at 30 to 50 m intervals, and the air gun was typically fired between 5 and 15 times at each station. The recorded waveforms were stacked, and a one-way traveltime was determined from the median of the first breaks for each station, thus providing check shots for calibration of the integrated transit time calculated from sonic logs. Check shot calibration is required for the core-seismic correlation because  $P$ -wave velocities derived from the sonic log may differ significantly from true formation velocity because of (1) frequency dispersion (the sonic tool operates at 10–20 kHz, but seismic data are in the 50–200 Hz

range), (2) difference in travel paths between well seismic and surface seismic surveys, and (3) borehole effects caused by formation alterations (Schlumberger, 1989). In addition, sonic logs cannot be measured through pipe, so traveltime down to the uppermost logging point has to be estimated by other means.

### Goettingen Borehole Magnetometer

The GBM tool was designed and developed in 1989 by the Geophysical Institute of the University of Goettingen, Germany (Fig. F26). The tool consists of three fluxgate sensors that log the horizontal ( $x$  and  $y$ ) and vertical ( $z$ ) components of the magnetic flux density. The tool is equipped with three angular rate sensors to monitor the spin history around the horizontal axes  $x$  and  $y$ , as well as the vertical tool axis  $z$ , and records inclinometer variations around the  $x$ - and  $y$ -axes during a logging run. The tool connects directly to the Schlumberger cable head. The housing is made of low-magnetic monel and is not affected by pressure and temperature up to 70 MPa at 100°C. A 300 lb low-magnetic sinker bar was added on top of the magnetometer for faster deployment.

The three LITEF miniature fiber-optic rate sensors provide angular rate output. They have a small volume and low weight and require little power (2 VA). Free from gravity-induced errors and with no moving parts, the sensor is insensitive to shock and vibration. Each rate sensor is an unconventional gyro because it does not have a spinning wheel. It detects and measures angular rates by measuring the frequency difference between two contrarotating light beams. The light source is a superluminescent diode. Its broad spectrum provides light with short coherence length to keep the undesirable backscattering effects in the optical path to sufficiently low levels. The beam is polarized, split, and phase modulated. The output light travels through a 110 m long fiber coil. The light travels to the detector, which converts the light into an electronic output signal. When the gyro is at rest, the two beams have identical frequencies. When the gyro is subjected to an angular turning rate around an axis perpendicular to the plane of the two beams, one beam then has a greater optical path length and the other beam has a shorter optical path length. Therefore, the two resonant frequencies change and the frequency differential is measured by optical means, resulting in a digital output. Readings are output at 1 Hz. The angular rate is a function of time sampled with 5 Hz and the accumulated angle. The angular rate measured by the sensor is influenced by the Earth's rotation, which depends on the latitude ( $\Phi$ ) and varies from 15.04°/h at the poles to 0°/h at the equator. From equator to pole, Earth's

measured rotation increases by  $\sin(\phi)$ . To obtain the rotation rate about an inertial system, the effect of Earth's rotation must be eliminated. If the rotation rate around each axis is known, the orientation of the tool can be derived as a function of depth from the rotation history. The maximum operation temperature for the fiber optic gyros is given at 71°C.

### Logging operations

In preparation for logging, the borehole is flushed with freshwater. The tool strings are then lowered downhole during sequential runs. The tool strings are pulled uphole at constant speed (typically at 250–300 m/h) to provide continuous measurements as a function of depth of several properties simultaneously. Each tool string also contains a telemetry cartridge, facilitating communication from the tools along a double-armored seven-conductor wireline cable to the computer van on the drillship.

Two wireline heave compensation systems were used during Expeditions 304 and 305. The LDEO-BRG wireline heave compensator (WHC) is employed to minimize the effect of ship's heave on the tool position in the borehole. As the ship heaves, an accelerometer located near the ship's center of gravity senses the movement and feeds the accelerometry data, in real time, to the WHC. The WHC responds by hydraulically moving the compensator's heave to decouple the movement of the ship from the tool string in the borehole. The second heave compensation system operates via a hydraulic pump, which controls the motion of a wireline drum. This system also uses data from ship three-axis accelerometers to correct for tool motion at the drum. Ultrasonic transducers are used to measure the radius of the drum to calculate tangential velocity and obtain an estimate of the tool speed downhole. The data are processed in the acquisition system and correlated with the compensated depth.

Data for each wireline logging run were recorded, stored digitally, and monitored in real time using the Schlumberger MAXIS 500 system located in the new Offshore Service Unit-F-model Modular Configuration MAXIS Electrical Capstan Capable (OSU-FMEC) winch unit. The OSU-FMEC is a full backup system to the main Schlumberger minimum configuration MAXIS system previously used for ODP logging operations. During Expedition 304, the OSU-FMEC unit was used as the primary acquisition system because we were using both heave compensator units.

### Wireline logging data quality

Logging data quality may be seriously degraded by changes in the hole diameter. Deep-investigation

measurements such as resistivity and sonic velocity are less sensitive to borehole conditions. Nuclear measurements (density and neutron porosity) are more sensitive to borehole diameter variability because of their shallower depth of investigation and the effect of drilling fluid volume on neutron porosity and GRA density. Corrections can be applied to the original data in order to reduce these effects. HNGS and SGT data provide a depth correlation between logging runs, but logs from different tool strings may still have minor depth mismatches caused by either cable stretch or ship heave during recording.

### Logging data flow and processing

Data for each wireline logging run were recorded and stored digitally and monitored in real time using the Schlumberger MAXIS 500 system. After logging was completed in each hole, data were transferred to the shipboard downhole measurements laboratory for preliminary processing and interpretation. FMS and UBI image data were interpreted using Schlumberger's Geoframe software package. Logging data were also transmitted to shore for processing. Shore-based data processing consisted of (1) depth-shifting all logs relative to a common datum (i.e., in mbsf), (2) corrections specific to individual tools, and (3) quality control and rejection of unrealistic or spurious values. Once processed onshore, the data were transmitted back to the ship, providing final processed logging results during the expedition. Data in ASCII are available directly from the IODP-USIO, Science Services, LDEO Web site at [iodp.ldeo.columbia.edu/DATA/IODP/index.html](http://iodp.ldeo.columbia.edu/DATA/IODP/index.html). GBM logging data were recorded in real time, and raw data were sent to Goettingen for shore-based postcruise processing.

## References

- ASTM, 1989. *Annual Book of ASTM Standards for Soil and Rock: Building Stones* (Vol. 4.08): *Geotextiles*: Philadelphia (Am. Soc. Testing and Mater.).
- Ayadi, M., Pezard, P.A., Laverne, C., and Bronner, G., 1998. Multi-scalar structure at DSDP/ODP Site 504, Costa Rica Rift, I: stratigraphy of eruptive products and accretion processes. In Harvey, P.K., and Lovell, M.A. (Eds.), *Core-Log Integration*. Geol. Soc. Spec. Publ., 136:297–310.
- Bach, W., Erzinger, J., Alt, J.C., and Teagle, D.A.H., 1996. Chemistry of the lower sheeted dike complex, Hole 504B (Leg 148): influence of magmatic differentiation and hydrothermal alteration. In Alt, J.C., Kinoshita, H., Stokking, L.B., and Michael, P.J. (Eds.), *Proc. ODP, Sci. Results*, 148: College Station, TX (Ocean Drilling Program), 39–55.
- Barr, S.R., Revillon, S., Brewer, T.S., Harvey, P.K., and Tarney, J., 2002. Determining the inputs to the Mariana subduction factory: using core-log integration to reconstruct basement lithology at ODP Hole 801C. *Geochem., Geophys., Geosyst.*, 3. doi:10.1029/2001GC000255
- Bartington Instruments, Ltd., 1995. *Operation Manual for MS2 Magnetic Susceptibility System*: Oxford (Bartington Instruments, Ltd.).
- Bell, J.S., and Gough, D.I., 1983. The use of borehole break-outs in the study of crustal stress. In Zoback, M.D., and Haimson, B.C. (Eds.), *Hydraulic Fracturing Stress Measurements*: Washington (National Academy Press), 201–209.
- Blum, P., 1997. Physical properties handbook: a guide to the shipboard measurement of physical properties of deep-sea cores. *ODP Tech. Note*, 26 [Online]. Available from World Wide Web: <<http://www-odp.tamu.edu/publications/tnotes/tn26/INDEX.HTM>>.
- Bouchez, J.L., Delas, C., Gleizes, G., Nedelec, A., and Cuney, M., 1992. Submagmatic microfractures in granites. *Geology*, 20:35–38. doi:10.1130/0091-7613(1992)020<0035:SMIG>2.3.CO;2
- Boyce, R.E., 1976. Definitions and laboratory techniques of compressional sound velocity parameters and wet-water content, wet-bulk density, and porosity parameters by gravimetric and gamma-ray attenuation techniques. In Schlanger, S.O., Jackson, E.D., et al., *Init. Repts. DSDP*, 33: Washington (U.S. Govt. Printing Office), 931–958.
- Brewer, T.S., Harvey, P.K., Lovell, M.A., Haggas, S., Pezard, P.A., and Goldberg, D., 1999. Borehole images of the ocean crust: case histories from the Ocean Drilling Program. In Lovell, M.A., Williamson, and Harvey, P.K. (Eds.), *Borehole Images: Application and Case Histories*. Geol. Soc. Spec. Publ., 159:283–294.
- Cannat, M., Karson, J.A., Miller, D.J., et al., 1995. *Proc. ODP, Init. Repts.*, 153: College Station, TX (Ocean Drilling Program).
- Cannat, M., Mével, C., and Stakes, D., 1991. Normal ductile shear zones at an oceanic spreading ridge: tectonic evolution of Site 735 gabbros (southwest Indian Ocean). In Von Herzen, R.P., Robinson, P.T., et al., *Proc. ODP, Sci. Results*, 118: College Station, TX (Ocean Drilling Program), 415–429.
- Dick, H.J.B., Meyer, P.S., Bloomer, S., Kirby, S., Stakes, D., and Mawer, C., 1991. Lithostratigraphic evolution of an in-situ section of oceanic Layer 3. In Von Herzen, R.P., Robinson, P.T., et al., *Proc. ODP, Sci. Results*, 118: College Station, TX (Ocean Drilling Program), 439–538.
- Dick, H.J.B., Natland, J.H., Miller, D.J., et al., 1999. *Proc. ODP, Init. Repts.*, 176: College Station, TX (Ocean Drilling Program). [HTML]
- Ellis, D.V., 1987. *Well Logging for Earth Scientists*: New York (Elsevier).
- Geological Survey of Japan, 2003. GSJ Geochemical Reference Sample Database. Available from World Wide Web: <<http://www.aist.go.jp/RIODB/geostand/>>.
- Gillis, K., Mével, C., Allan, J., et al., 1993. *Proc. ODP, Init. Repts.*, 147: College Station, TX (Ocean Drilling Program).

- Goldberg, D., 1997. The role of downhole measurements in marine geology and geophysics. *Rev. Geophys.*, 35:315–342. doi:10.1029/97RG00221
- Guéguen, Y., and Palciauskas, V., 1992. *Introduction à la physique des roches*: Paris (Hermann).
- Haggas, S., Brewer, T.S., Harvey, P.K., and Iturrino, G., 2001. Relocating and orienting cores by the integration of electrical and optical images: a case study from Ocean Drilling Program Hole 735B. *J. Geol. Soc. (London, U. K.)*, 158:615–623.
- Hellebrand, E., Snow, J.E., Dick, H.J.B., and Hofmann, A.W., 2001. Coupled major and trace elements as indicators of the extent of melting in mid-ocean-ridge peridotites. *Nature (London, U. K.)*, 410:677–681. doi:10.1038/35070546
- Hext, G., 1963. The estimation of second-order tensors, with related tests and designs. *Biometrika*, 50:353–375.
- Hirth, G., and Kohlstedt, D.L., 1995. Experimental constraints on the dynamics of the partially molten upper mantle: deformation in the diffusion creep regime. *J. Geophys. Res.*, 100:15,441–15,450. doi:10.1029/95JB01292
- Ildefonse, B., and Pezard, P., 2001. Electrical properties of slow-spreading ridge gabbros from ODP Site 735, Southwest Indian Ridge. *Tectonophysics*, 330:69–92. doi:10.1016/S0040-1951(00)00220-1
- Imai, N., Terashima, S., Itoh, S., and Ando, A., 1995. 1994 compilation of analytical data for minor and trace elements in seventeen GSJ geochemical reference samples: igneous rock series. *Geostand. Newsl.*, 19:135–213.
- Kelemen, P.B., Kikawa, E., Miller, D.J., et al., 2004. *Proc. ODP, Init. Repts.*, 209 [CD-ROM]. Available from: Ocean Drilling Program, Texas A&M University, College Station TX 77845-9547, USA. [HTML]
- Kirschvink, J.L., 1980. The least-squares line and plane and the analysis of palaeomagnetic data. *Geophys. J. R. Astron. Soc.*, 62:699–718.
- Kobayashi, Y., 1974. Anisotropy of thermal diffusivity in olivine, pyroxene and dunite. *J. Phys. Earth*, 22:35–373.
- Kretz, R., 1983. Symbols for rock-forming minerals. *Am. Mineral.*, 68:277–279.
- Lamont-Doherty Earth Observatory-Borehole Research Group, 1994. *Wireline Logging Services Guide* [Online]. Available from World Wide Web: <<http://www.ldeo.columbia.edu/BRG/ODP/LOGGING/>>.
- Le Bas, M.J., and Streckeisen, A.L., 1991. The IUGS systematics of igneous rocks. *J. Geol. Soc. (London, U. K.)*, 148:825–833.
- Le Maitre, R.W., 1989. *A Classification of Igneous Rocks and Glossary of Terms*: Oxford (IUGS, Blackwell).
- Lovell, M.A., Harvey, P.K., Brewer, T.S., Williams, C., Jackson, P.D., and Williamson, G., 1998. Application of FMS images in the Ocean Drilling Program: an overview. In Cramp, A., MacLeod, C.J., Lee, S.V., and Jones, E.J.W. (Eds.), *Geological Evolution of Ocean Basins: Results from the Ocean Drilling Program*. Geol. Soc. Spec. Publ., 131:287–303.
- Means, W.D., and Park, Y., 1994. New experimental approach to understanding igneous texture. *Geology*, 22:323–326. doi:10.1130/0091-7613(1994)022<0323:NEATUI>2.3.CO;2
- Miller, D.J., Iturrino, G.J., and McGuire, J.C., 2003. Core-log correlations in oceanic basement from Hole 1105A on the Southwest Indian Ridge. In Casey, J.F., and Miller, D.J. (Eds.), *Proc. ODP, Sci. Results*, 179 [Online]. Available from World Wide Web: <[http://www-odp.tamu.edu/publications/179\\_SR/chap\\_03/chap\\_03.htm](http://www-odp.tamu.edu/publications/179_SR/chap_03/chap_03.htm)>.
- Murray, R.W., Miller, D.J., and Kryc, K.A., 2000. Analysis of major and trace elements in rocks, sediments, and interstitial waters by inductively coupled plasma-atomic emission spectrometry (ICP-AES). *ODP Tech. Note*, 29 [Online]. Available from World Wide Web: <<http://www-odp.tamu.edu/publications/tnotes/tn29/INDEX.HTM>>.
- Nicolas, A., and Ildefonse, B., 1996. Flow mechanisms and viscosity in basaltic magma chambers. *Geophys. Res. Lett.*, 23:2013–2016. doi:10.1029/96GL02073
- O’Hanley, D.S., 1996. Serpentinites: records of tectonic and petrological history. *Oxford Monogr. Geol. Geophys.*, Vol. 34.
- Olhoef, G.R., 1981. Electrical properties of rocks. In Tou-loukian, Y.S., Judd, W.R., and Roy, R.F. (Eds.), *Physical Properties of Rocks and Minerals*: New York (McGraw-Hill), 257–330.
- Paillet, F.L., and Kim, H., 1987. Character and distribution of borehole breakouts and their relationship to in situ stresses in deep Columbia River basalts. *J. Geophys. Res.*, 92:6223–6234.
- Puchelt, H., Malpas, J., Falloon, T., Pedersen, R., Eckhardt, J.-D., and Allan, J.F., 1996. *Data report: Ultramafic reference material from Core 147-895D-10W*. In Mével, C., Gillis, K.M., Allan, J.F., and Meyer, P.S. (Eds.), *Proc. ODP, Sci. Results*, 147: College Station, TX (Ocean Drilling Program), 493–496.
- Remaïdi, M., 1993. Etude géochimique de l’association harzburgite, dunite et pyroxénite de l’Arroyo de la Cala (Massif de Ronda, Espagne) [Ph.D. thesis]. Université Montpellier 2, Montpellier, France.
- Rider, M.H., 1996. *The Geological Interpretation of Well Logs* (2nd ed.): Caithness (Whittles Publishing).
- Robinson, P.T., Von Herzen, R., et al., 1989. *Proc. ODP, Init. Repts.*, 118: College Station, TX (Ocean Drilling Program).
- Schlumberger, 1989. *Log Interpretation Principles/Applications*: Houston (Schlumberger Educ. Services), SMP-7017.
- Schlumberger, 1994. *Log Interpretation Charts: Sugarland*, TX (Schlumberger Wireline and Testing), SMP-7006.
- Serra, O., 1984. *Fundamentals of Well-Log Interpretation* (Vol. 1): *The Acquisition of Logging Data*: Dev. Pet. Sci., 15A: Amsterdam (Elsevier).
- Serra, O., 1986. *Fundamentals of Well-Log Interpretation* (Vol. 2): *The Interpretation of Logging Data*. Dev. Pet. Sci., 15B: Amsterdam (Elsevier).
- Serra, O., 1989. *Formation MicroScanner Image Interpretation*: Houston (Schlumberger Educ. Services), SMP-7028.

- Shipboard Scientific Party, 1992. Explanatory notes. In Dick, H.J.B., Erzinger, J., Stokking, L.B., et al., *Proc. ODP, Init. Repts.*, 140: College Station, TX (Ocean Drilling Program), 5–33.
- Shipboard Scientific Party, 1993. Explanatory notes. In Gillis, K., Mével, C., Allan, J., et al., *Proc. ODP, Init. Repts.*, 147: College Station, TX (Ocean Drilling Program), 15–42.
- Shipboard Scientific Party, 1995. Explanatory notes. In Cannat, M., Karson, J.A., Miller, D.J., et al., *Proc. ODP, Init. Repts.*, 153: College Station, TX (Ocean Drilling Program), 15–42.
- Shipboard Scientific Party, 1999. Explanatory notes. In Dick, H.J.B., Natland, J.H., Miller, D.J., et al., *Proc. ODP, Init. Repts.*, 176, 1–42 [CD-ROM]. Available from: Ocean Drilling Program, Texas A&M University, College Station, TX 77845-9547, U.S.A. [HTML]
- Shipboard Scientific Party, 2001. Explanatory notes. In Christie, D.M., Pedersen, R.B., Miller, D.J., et al., *Proc. ODP, Init. Repts.*, 187, 1–42 [CD-ROM]. Available from: Ocean Drilling Program, Texas A&M University, College Station TX 77845-9547, USA. [HTML]
- Shipboard Scientific Party, 2002. Explanatory notes. In Tarduno, J.A., Duncan, R.A., Scholl, D.W., et al., *Proc. ODP, Init. Repts.*, 197, 1–89 [CD-ROM]. Available from: Ocean Drilling Program, Texas A&M University, College Station TX 77845-9547, USA. [HTML]
- Shipboard Scientific Party, 2004. Explanatory notes. In Kelemen, P.B., Kikawa, E., Miller, D.J., et al., *Proc. ODP, Init. Repts.*, 209, 1–75 [CD-ROM]. Available from: Ocean Drilling Program, Texas A&M University, College Station TX 77845-9547, USA. [HTML]
- Smith, D.C., Spivack, A.J., Fisk, M.R., Haveman, S.A., Staudigel, H., and ODP Leg 185 Shipboard Scientific Party, 2000. Methods for quantifying potential microbial contamination during deep ocean coring. *ODP Tech. Note*, 28 [Online]. Available from World Wide Web: <<http://www-odp.tamu.edu/publications/tnotes/tn28/INDEX.HTM>>.
- Sparks, J.W., and Zuleger, E., 1995. *Data report: Chemical analyses of the Leg 140 reference sample.* In Erzinger, J., Becker, K., Dick, H.J.B., Stokking, L.B. (Eds.), *Proc. ODP, Sci. Results*, 137/140: College Station, TX (Ocean Drilling Program), 353–355.
- Streckeisen, A., 1974. Classification and nomenclature of plutonic rocks. *Geol. Rundsch.*, 63:773–786.
- Tommasi, A., Gibert, B., Seipold, U., and Mainprice, D., 2002. Anisotropy of thermal diffusivity in the upper mantle. *Nature (London, U. K.)*, 411:783–786. doi:10.1038/35081046
- United States Geological Survey, 2003. U.S. Geological Survey geochemical reference materials and certificates [Online]. Available from World Wide Web: <[http://minerals.cr.usgs.gov/geo\\_chem\\_stand](http://minerals.cr.usgs.gov/geo_chem_stand)>.
- Vacquier, V., 1985. The measurement of thermal conductivity of solids with a transient linear heat source on the plane surface of a poorly conducting body. *Earth Planet. Sci. Lett.*, 74:275–279. doi:10.1016/0012-821X(85)90027-5

**Publication:** 3 June 2006  
**MS 304305-102**

**Figure F1.** Illustration of Integrated Ocean Drilling Program (IODP) labeling scheme used for holes, cores, and sections. mbsl = meters below sea level, mbsf = meters below seafloor.

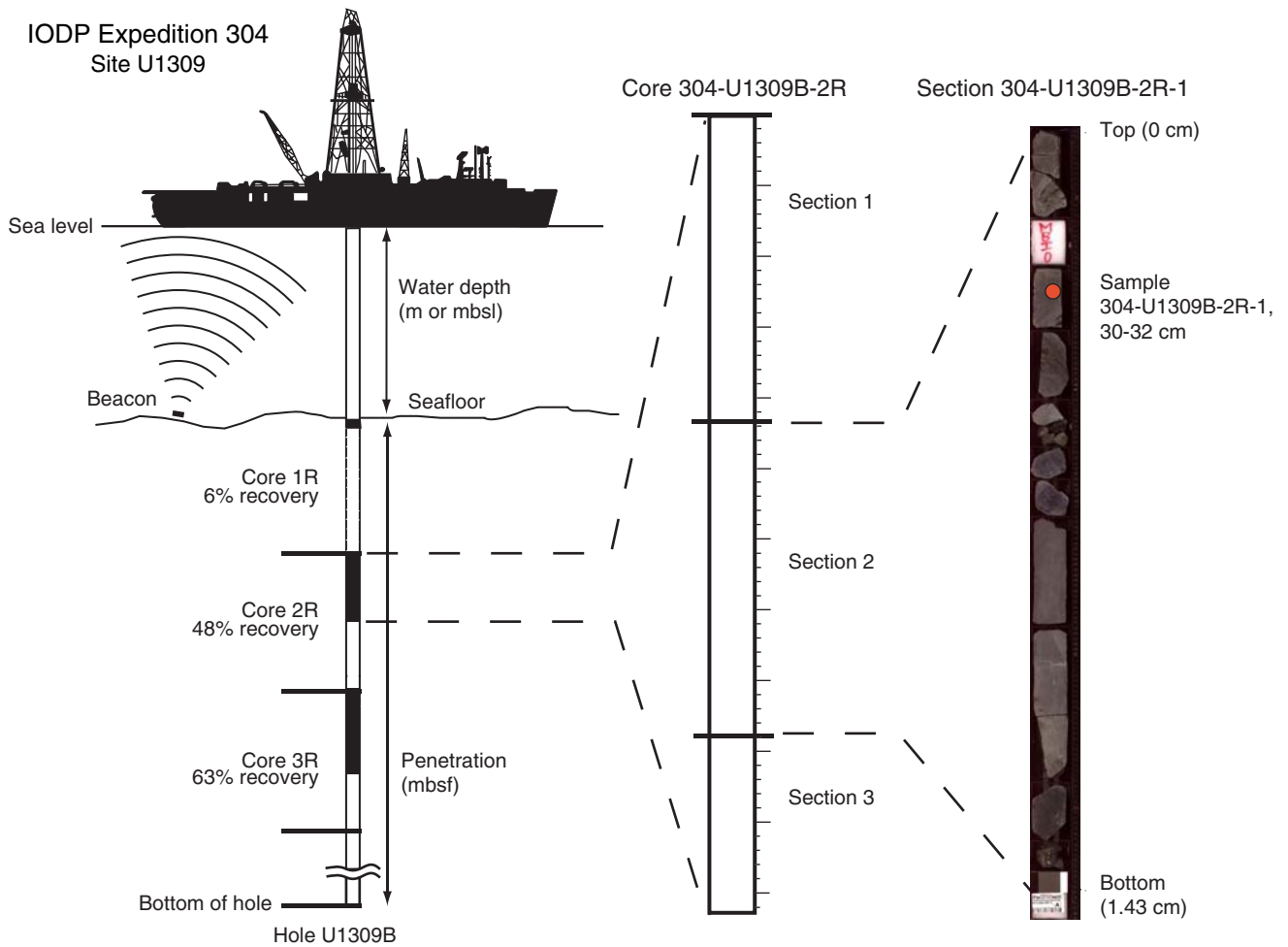


**Figure F2.** Example of a VCD log sheet. Abbreviations used in “Shipboard Studies” column are Ph = close-up photograph, TSB = thin section, ICP = bulk chemical analysis, XRD = X-ray diffraction, PP = physical properties, PMAG = paleomagnetism, CHR = samples of basaltic glass for shore-based analysis.

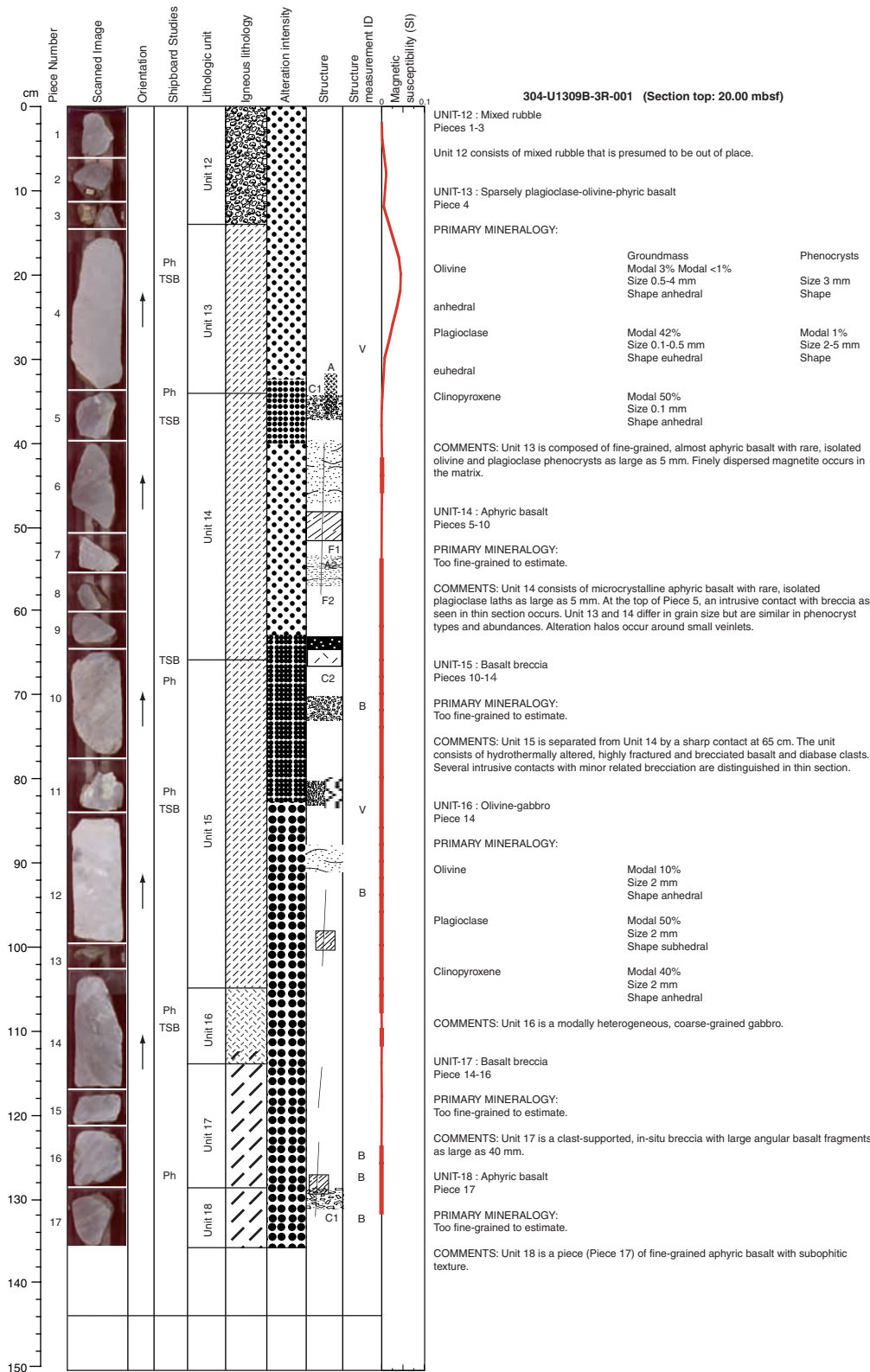


Figure F3. Patterns used in sediment VCD forms.

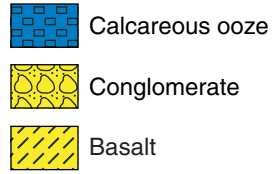


Figure F4. Modal classification scheme for plutonic igneous rocks, after Streckeisen (1974).

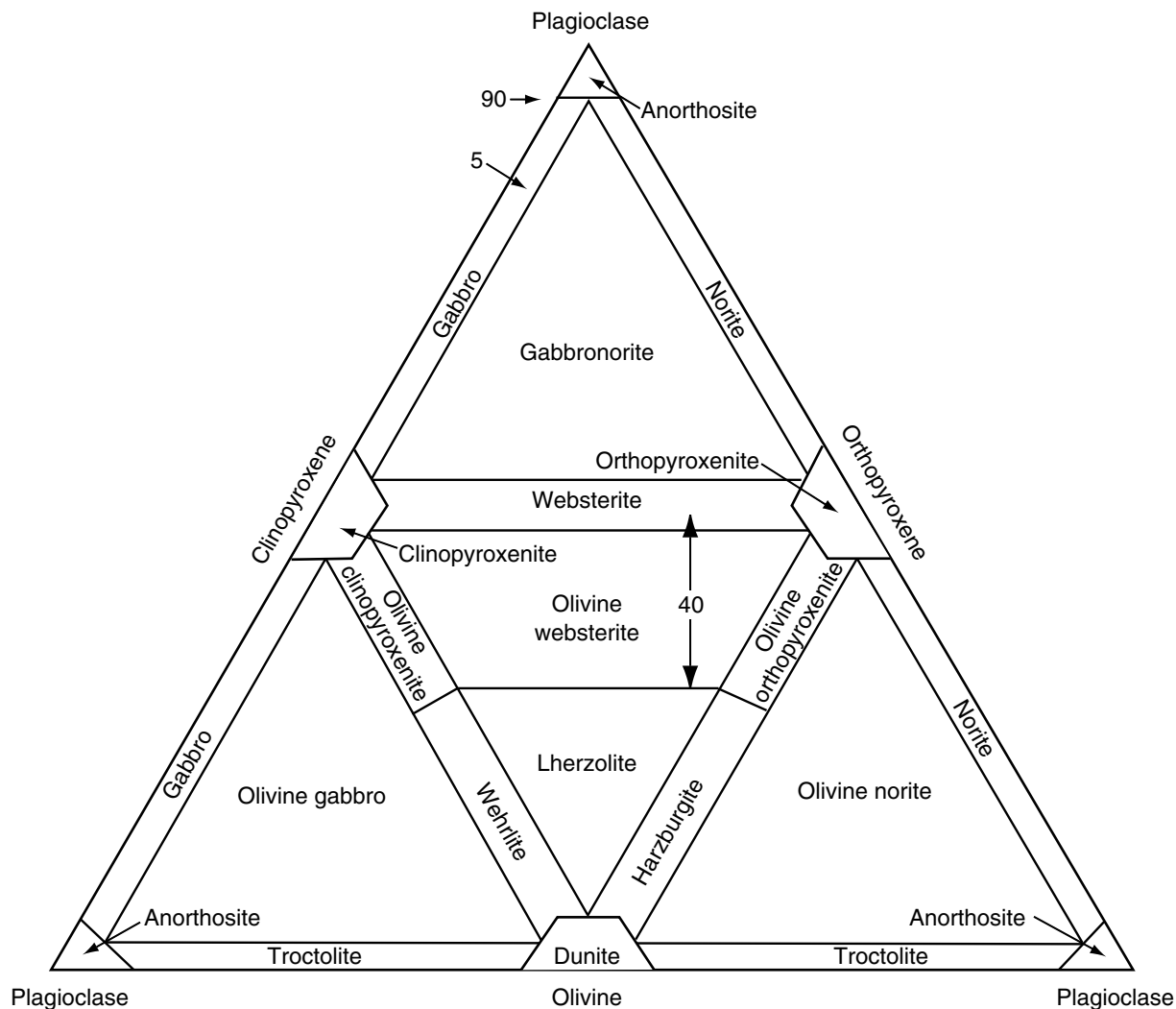


Figure F5. Igneous lithology swatches used in barrel sheets (VCDs).

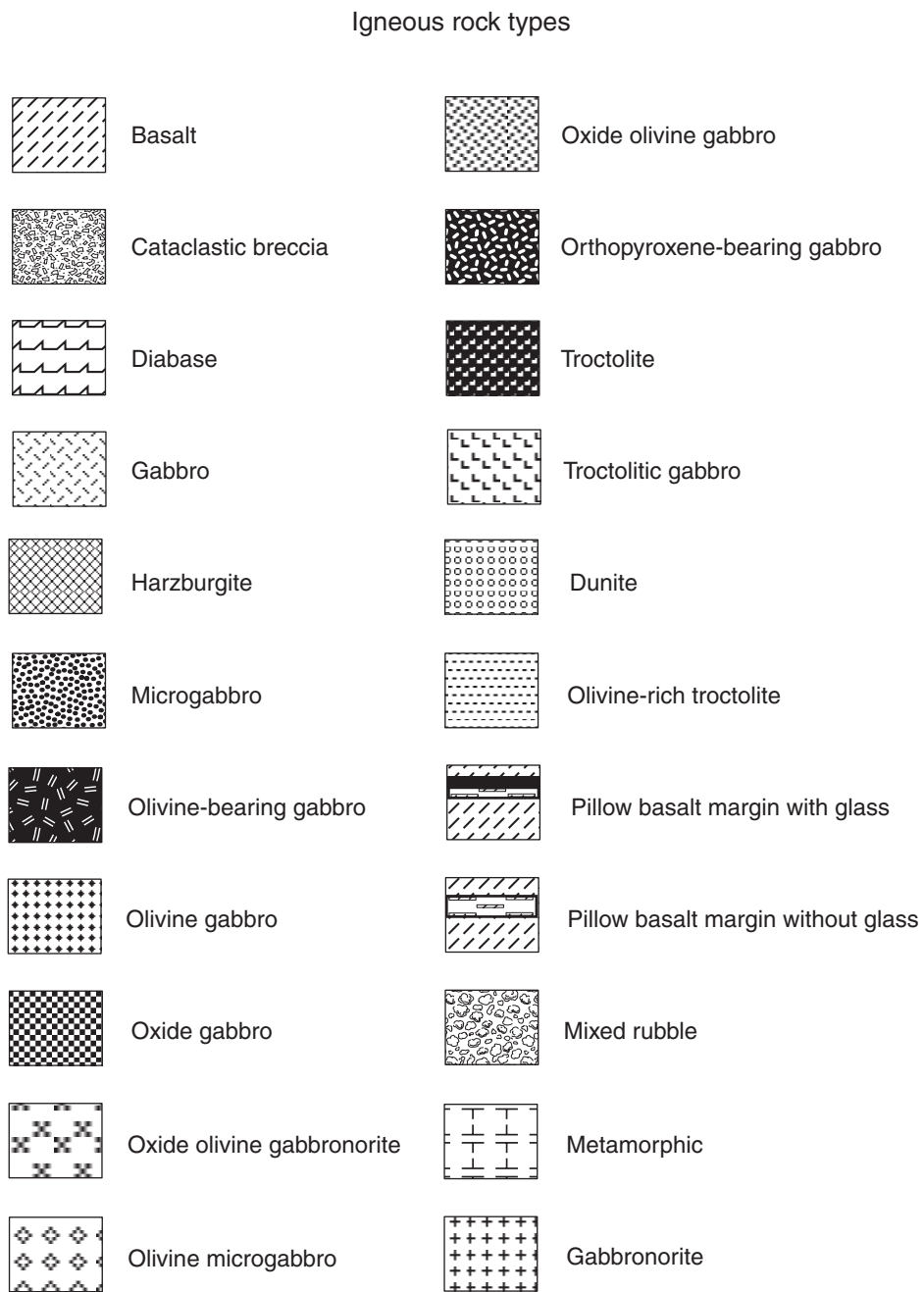


Figure F6. Cambridge Image Technology Ltd. MK5 analytical miniprobe top plate and control unit.



**Figure F7.** Correlation of spinel Cr# ( $\text{Cr}/[\text{Cr} + \text{Al}]$ ) measured by electron microprobe analysis (EPMA) and miniprobe. Cr# were calculated from miniprobe data as  $\text{Cr\#(true)} = 0.9594 \times \text{Cr\#(miniprobe)} - 12.833$ .

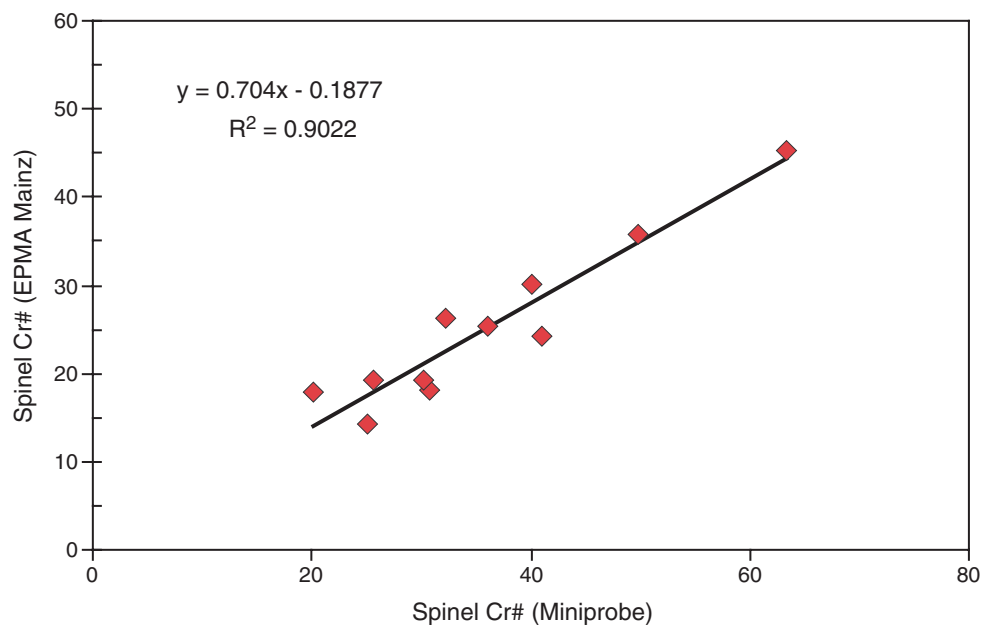


Figure F8. Codes used to denote alteration intensity in the VCD stratigraphic columns.

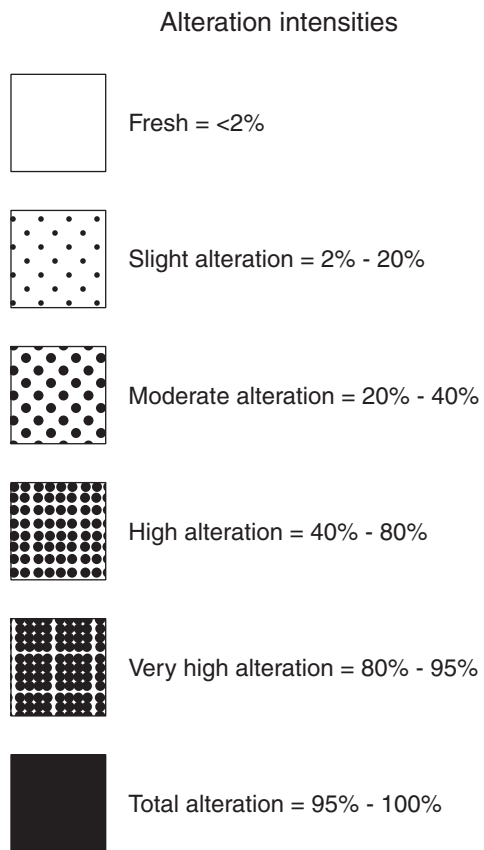
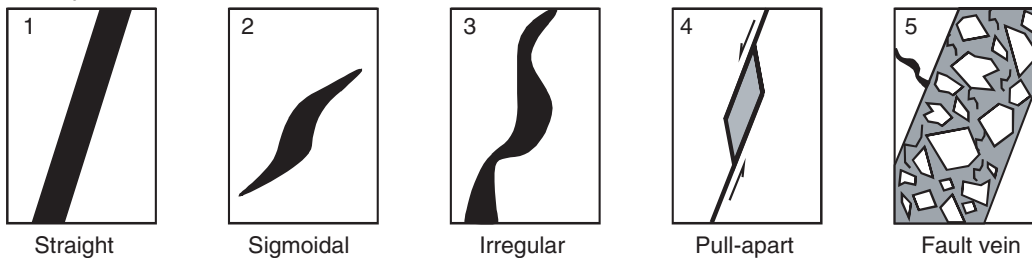
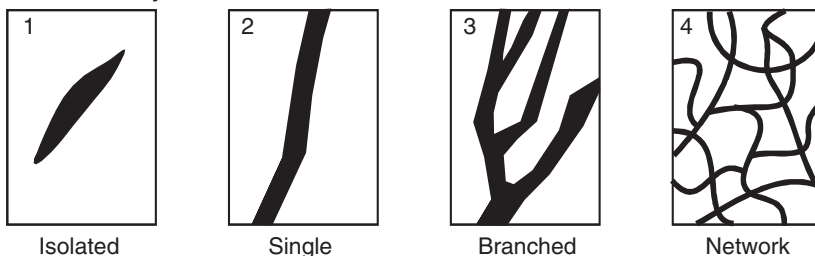


Figure F9. Vein classifications used in the vein log.

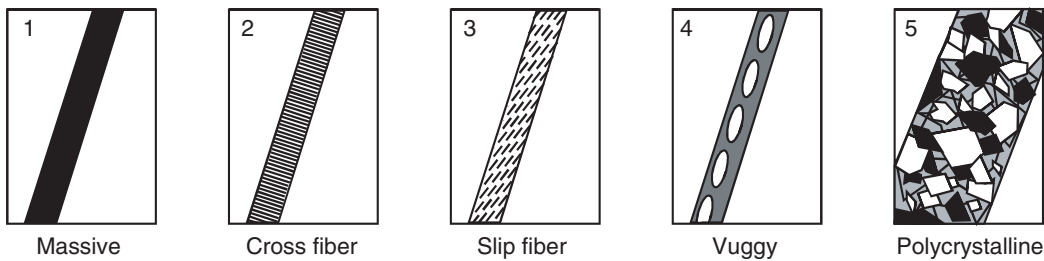
Vein shape



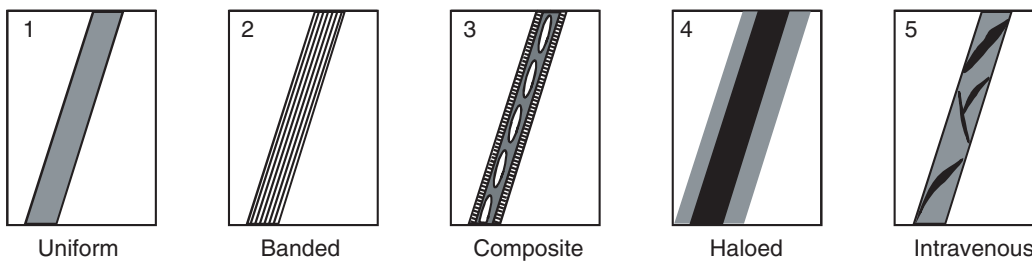
Vein connectivity



Vein texture



Vein structure



Particular vein geometries

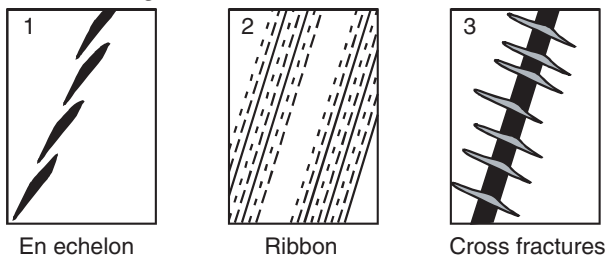


**Figure F10.** Core reference frame used for orienting structures. **A.** Three-dimensional perspective of core. **B.** Cut face.

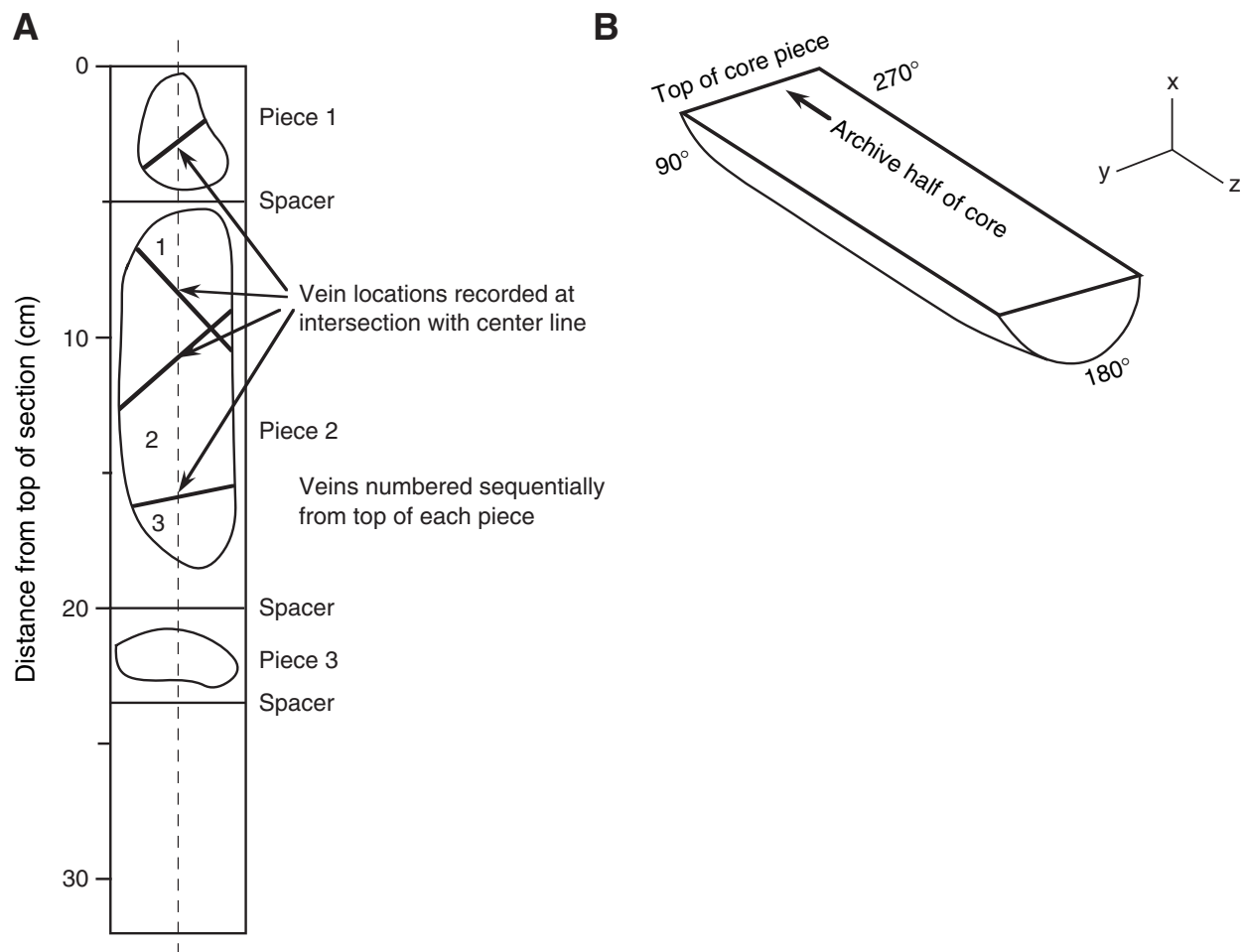
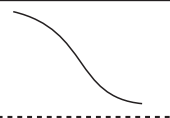
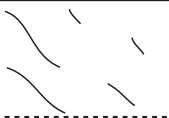
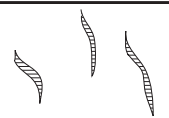
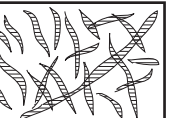
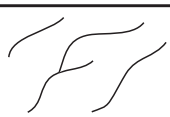
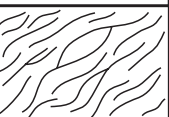
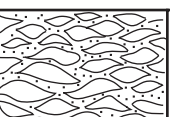
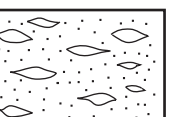
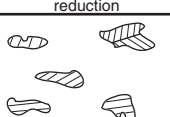
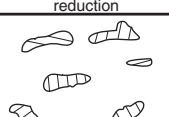
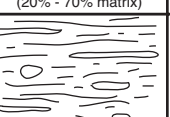
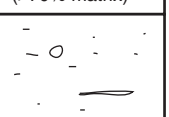
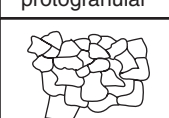
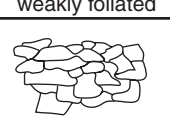
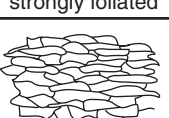
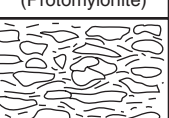
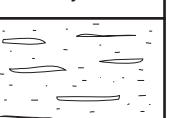
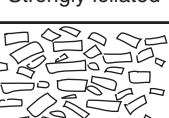
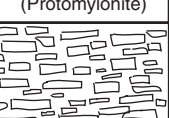


Figure F11. Symbols used in VCDs.

## Structure symbols

	Breccia		Serpentine mesh texture
	Conjugate fracture		Striae
	Crystal/Mineral lineation		Vein conduit
	Crystal-plastic fabric		Vein network
	Dike		Vein set
	Fracture		Wide vein
	Fracture network		Sense of shear
	Fracture with brecciation		Vein 1 - intergranular alteration
	Fracture set		Microcracking
	Igneous contact (orientation, type)		Cataclastic breccia
	Magmatic foliation		Altered
	Magmatic vein		Mafic schist
	Primary ductile deformation		

Figure F12. Intensity scales used for structural identification. See text for detailed explanation. sig. = significant.

Feature	0	1	2	3	4	5
Joints/ Open fractures	 No open fractures	 <1 per 10 cm	 1-5 per 10 cm	 >5 per 10 cm		
Veins	 No veins	 <1 per 10 cm	 1-5 per 10 cm	 5-10 per 10 cm	 10-20 per 10 cm	 >20 per 10 cm
Serpentine foliation	 Massive	 Weakly foliated	 Moderately foliated	 Strongly foliated		
Cataclastic deformation	 Undeformed	 Minor fracturing No sig. grain size reduction	 Moderate fracturing No sig. grain size reduction	 Dense anastomosing fracturing and incipient brecciation (<20% matrix)	 Well-developed fault brecciation; clast rotation (20% - 70% matrix)	 Cataclasite (>70% matrix)
Peridotite crystal-plastic deformation	 Undeformed protogranular	 Porphyroclastic weakly foliated	 Porphyroclastic strongly foliated	 Porphyroclastic (Protomylonite)	 Mylonite	 Ultramylonite
Gabbro crystal-plastic deformation	 Undeformed	 Weakly foliated	 Strongly foliated	 Porphyroclastic (Protomylonite)	 Mylonite	 Ultramylonite
Magmatic foliation	 Isotropic: no shape fabric	 Weak shape fabric	 Moderate shape fabric	 Strong shape fabric		

**Figure F13.** Calibration of the noncontact resistivity (NCR) instrument using ~15 cm long core liners filled with NaCl solution as marked. Note that the peak response to each sample occurs some 8 cm from the edge of the sample. Calibration run was made on 24 November 2004 at 1600 GMT.

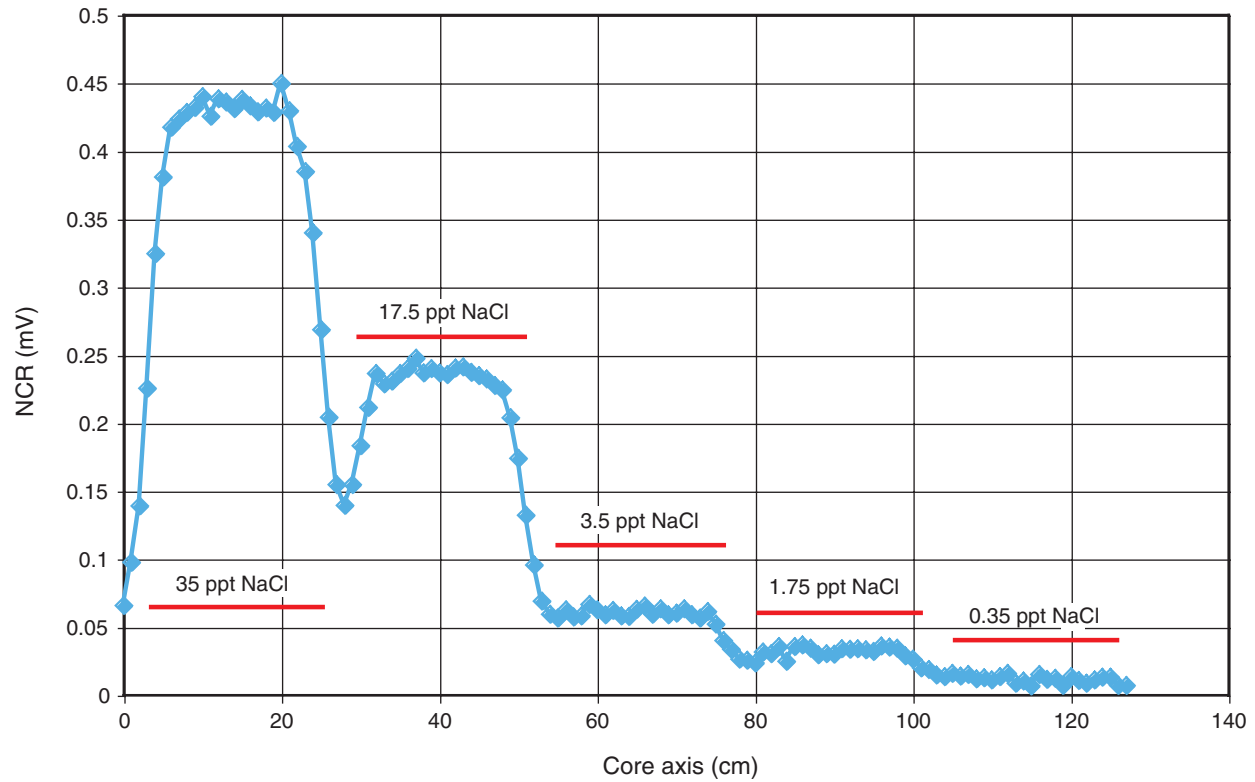


**Figure F14.** Resistivity of standard solutions of NaCl versus average peak instrument response (red dots) from Figure F13. Black line shows best-fit curve used to convert volts to resistivity. NCR = noncontact resistivity.

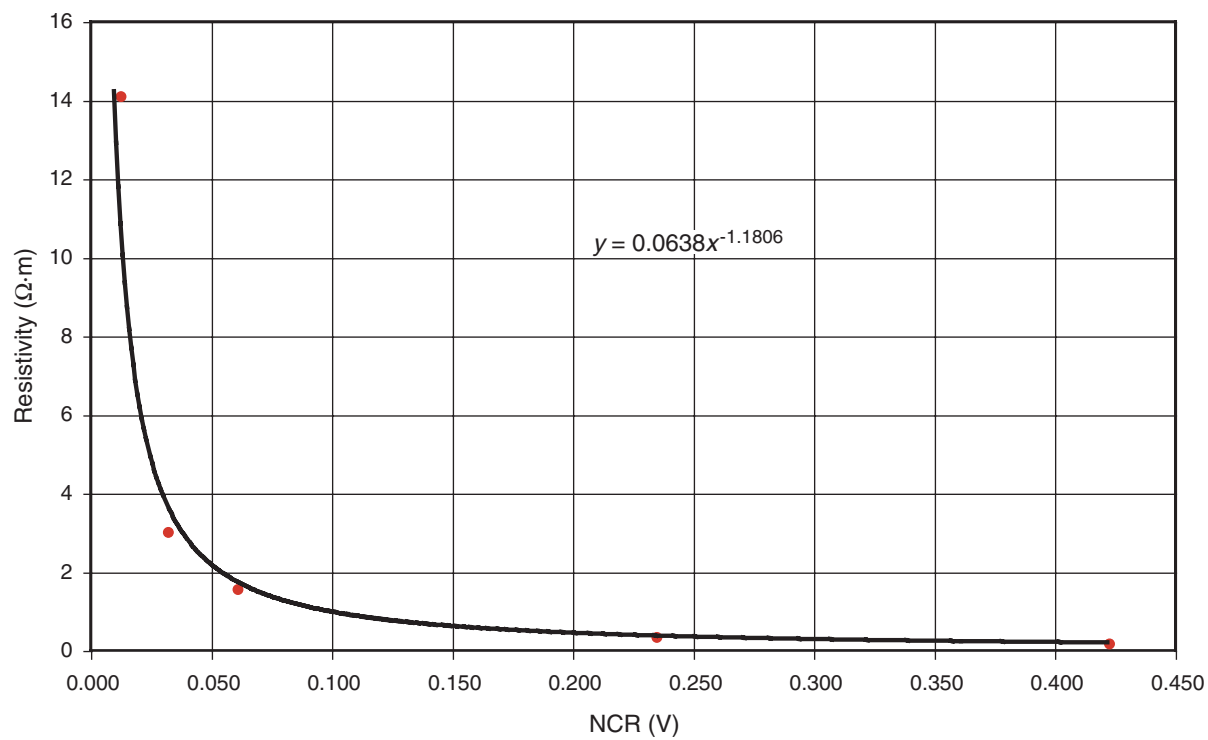


**Figure F15.** Noncontact resistivity (NCR) for Core 304-U1309D-38R, second uncurated liner, curated Section 2 and part of Section 3, measured (A) ~15 min after the core came on board, and (B) ~2.5 h later.

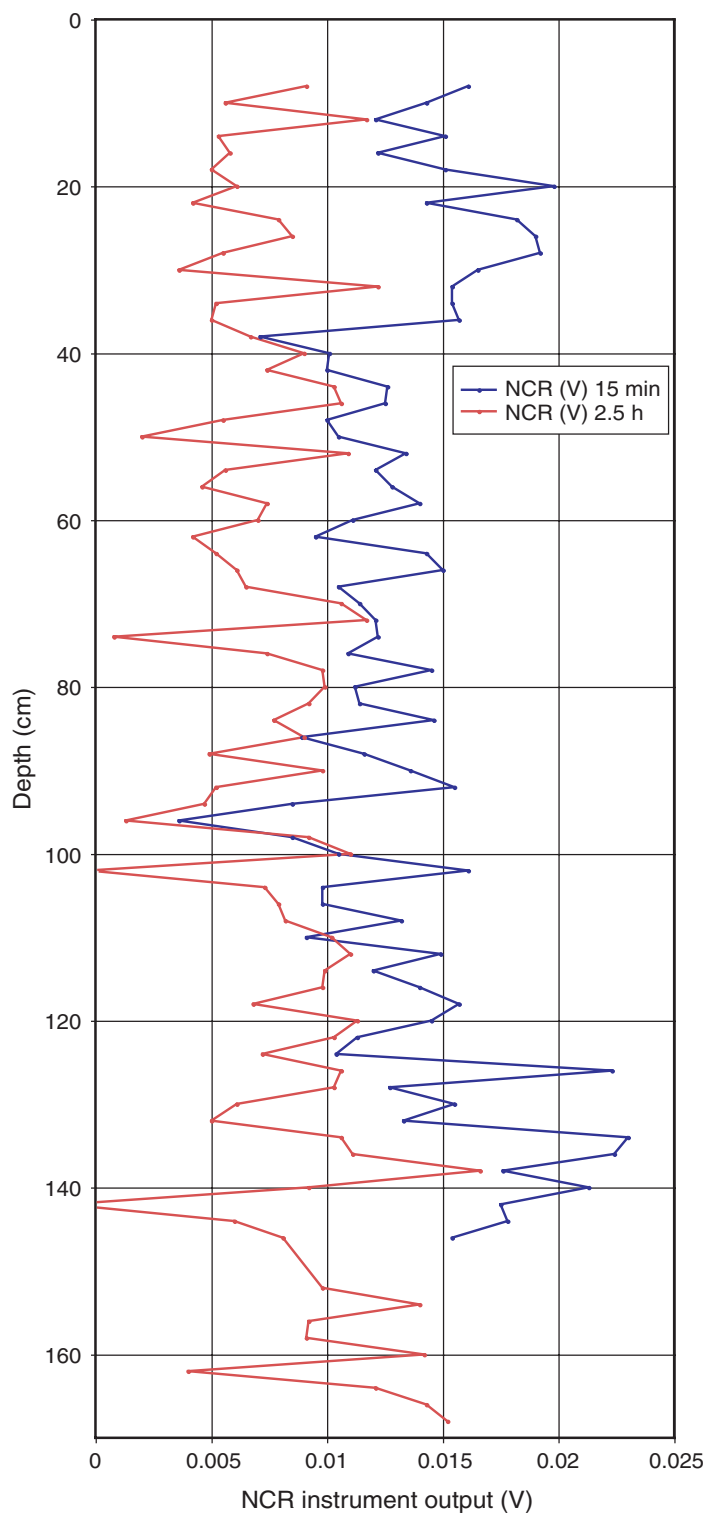


**Figure F16.** Noncontact resistivity (NCR) measured on Section 304-U1309D-36R-1 (Pieces 1 and 2), dry and after saturation in seawater for varying times.

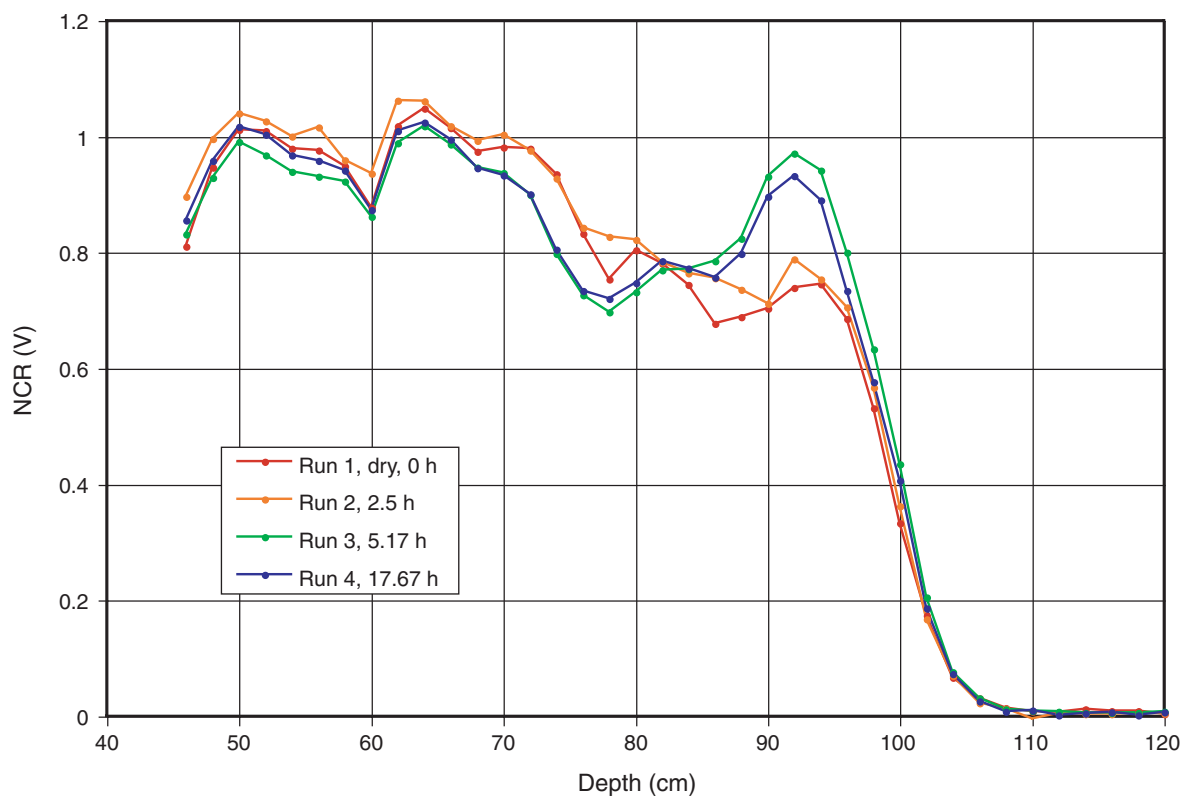


**Figure F17.** Test magnetic susceptibility (MS) curve for the MST loop magnetometer, showing response to a test sample in which magnetic material is confined to a 3 cm interval at 51 cm alongcore. Note that the effective along-core resolution is ~4 cm.

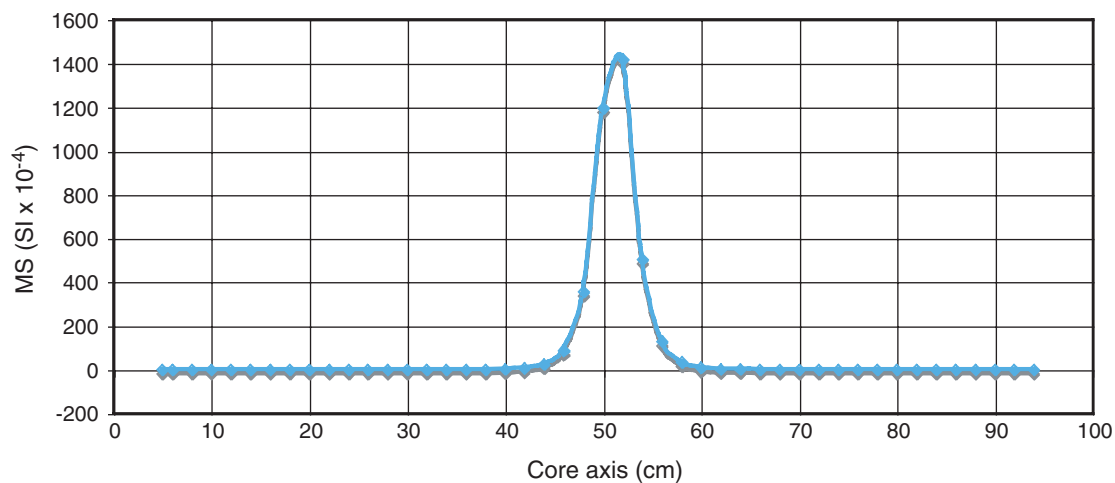


**Figure F18.** Measurements of magnetic susceptibility using the MST compared with electrical conductivity from the NCR on Sections 304-U1309D-35R-1 through 36R-1, lithologic Unit 88 (oxide gabbros). **A.** Raw measurements. Note apparently noisy susceptibility signal. **B.** After application of an arbitrary additive constant of either 10,000 SI or 20,000 SI (one or two times full range). Following this correction, the susceptibility signal is much less noisy and correlates well with the conductivity signal. However, it is not possible to know a priori the number of times 10,000 must be added to the recorder value.

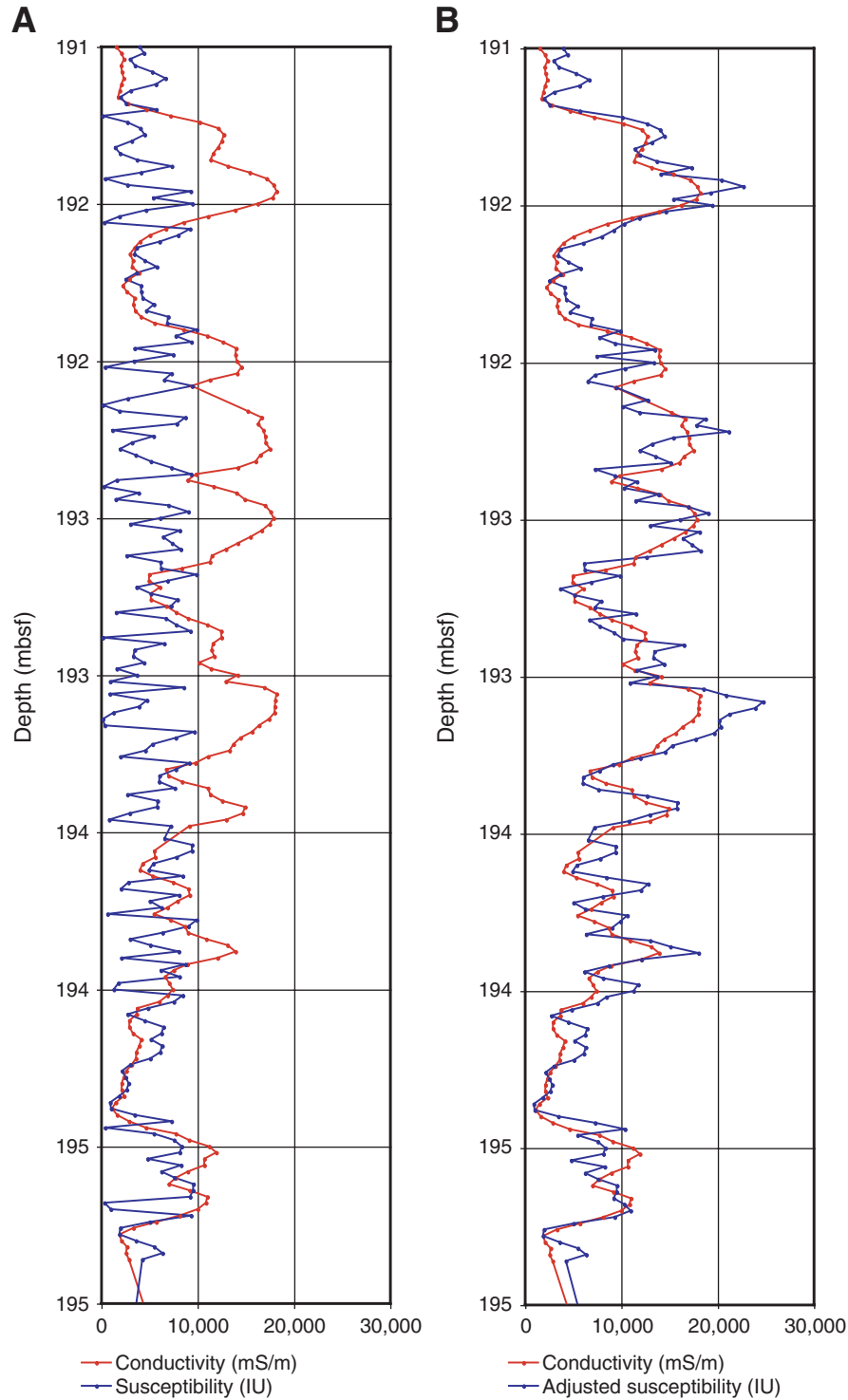


**Figure F19.** Comparison of magnetic susceptibility (MS) measured on the MS2C sensor of the multisensor track (MST) and the MS2E1 sensor of the archive MST (AMST). Data are from Cores 304-U1309B-1R through 20R.

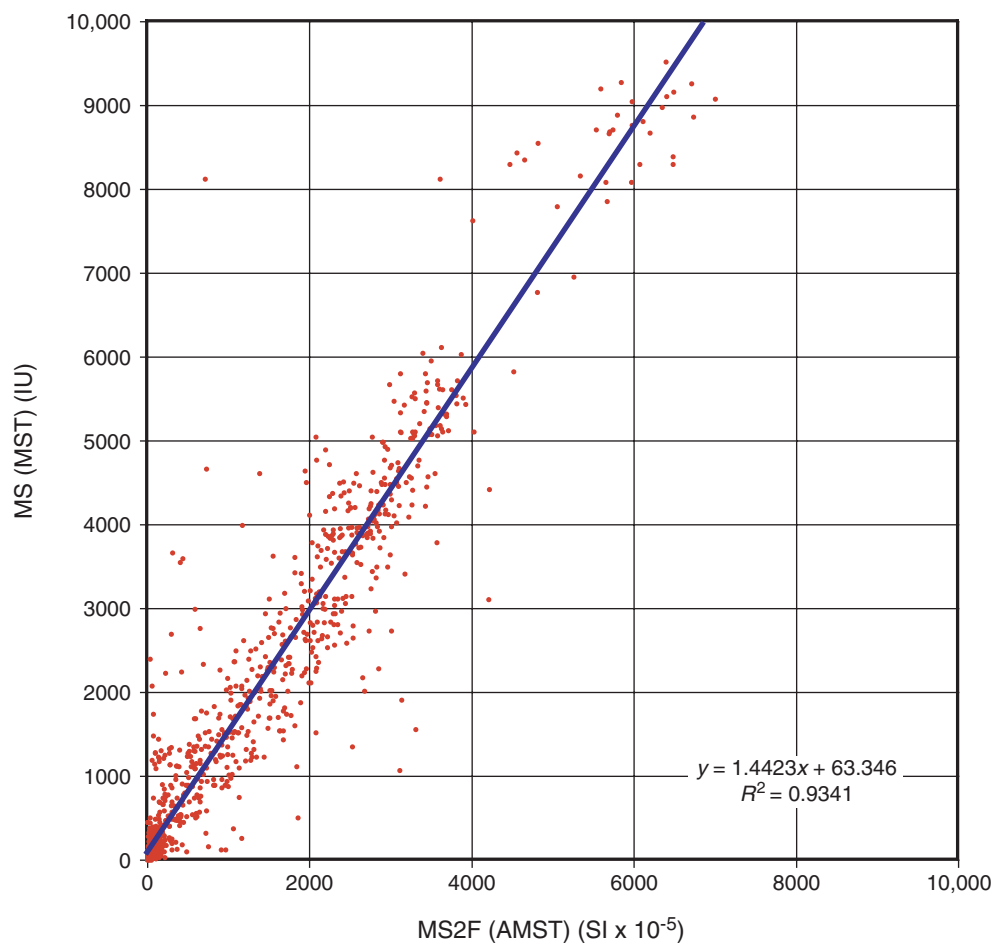


**Figure F20.** Comparison of susceptibilities measured on the MS2F point sensor and the Kappabridge. AMST = archive multisensor track.

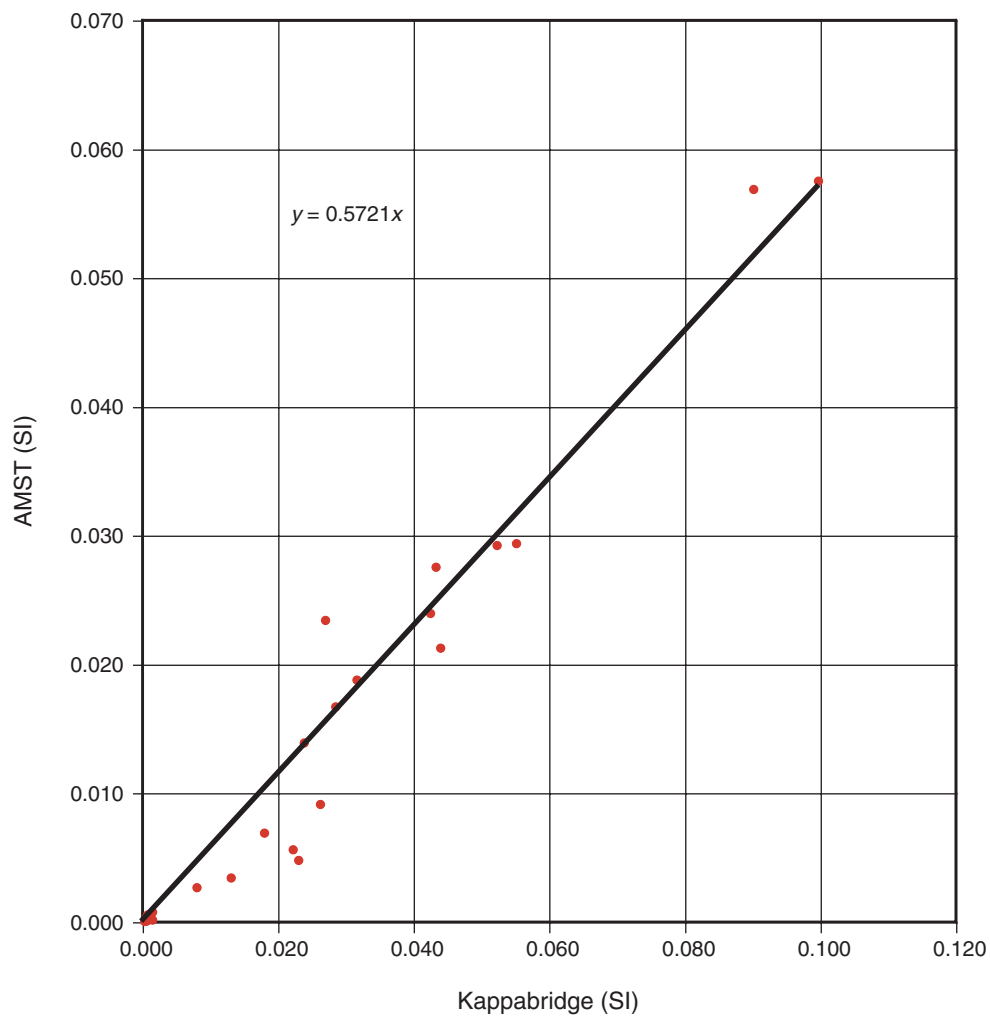
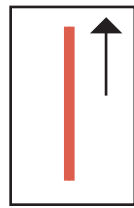
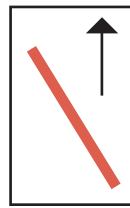


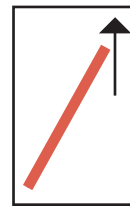
**Figure F21.** Convention notation (0, 1, or 2) used for the orientation of the needle probe in thermal conductivity measurement data tables during Expedition 304. The arrow points to the top of the core.



0 - parallel  
to core axis



1 - oblique  
to core axis



2 - oblique  
to core axis

Figure F22. Seismogram produced by the PWS3 instrument showing the automatic pick of the first arrival.

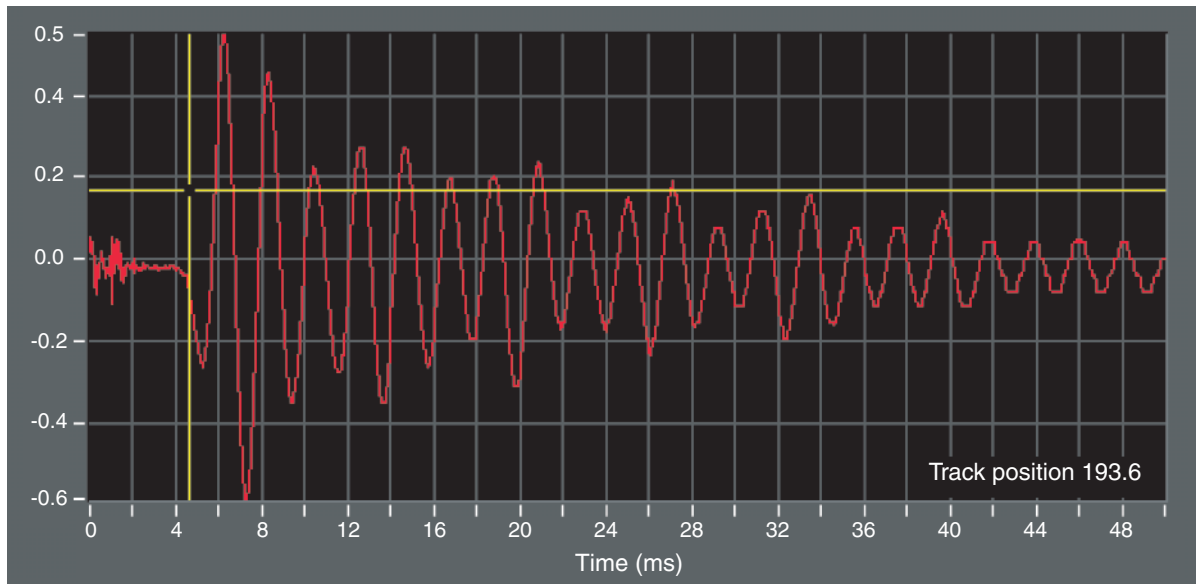


**Figure F23.** Configuration of the wireline logging tool strings used during Expeditions 304 and 305. Triple combo = triple combination, FMS = Formation MicroScanner, GBM = Goettingen Borehole Magnetometer.

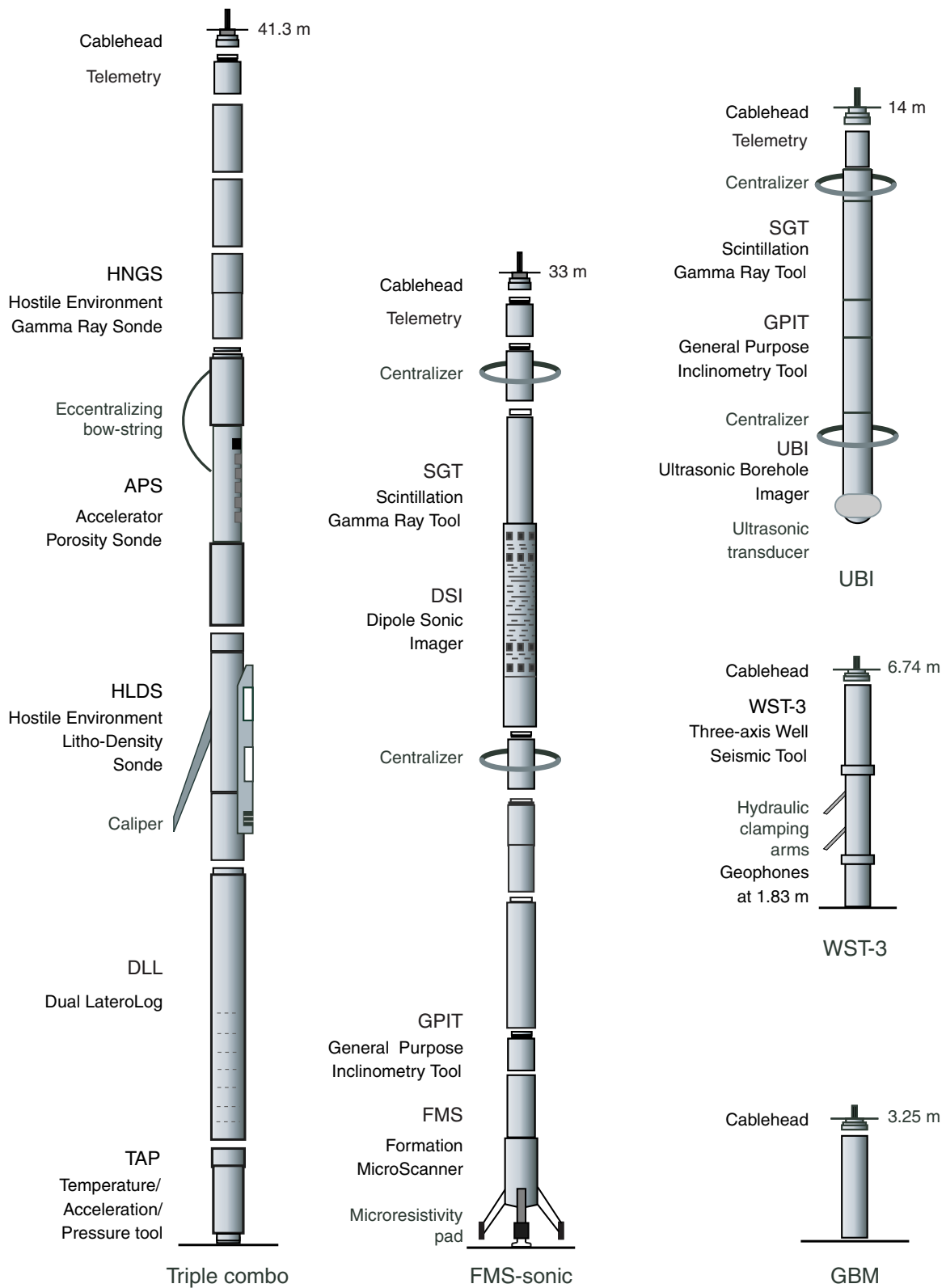


Figure F24. Schematic diagram of the Formation MicroScanner pad.

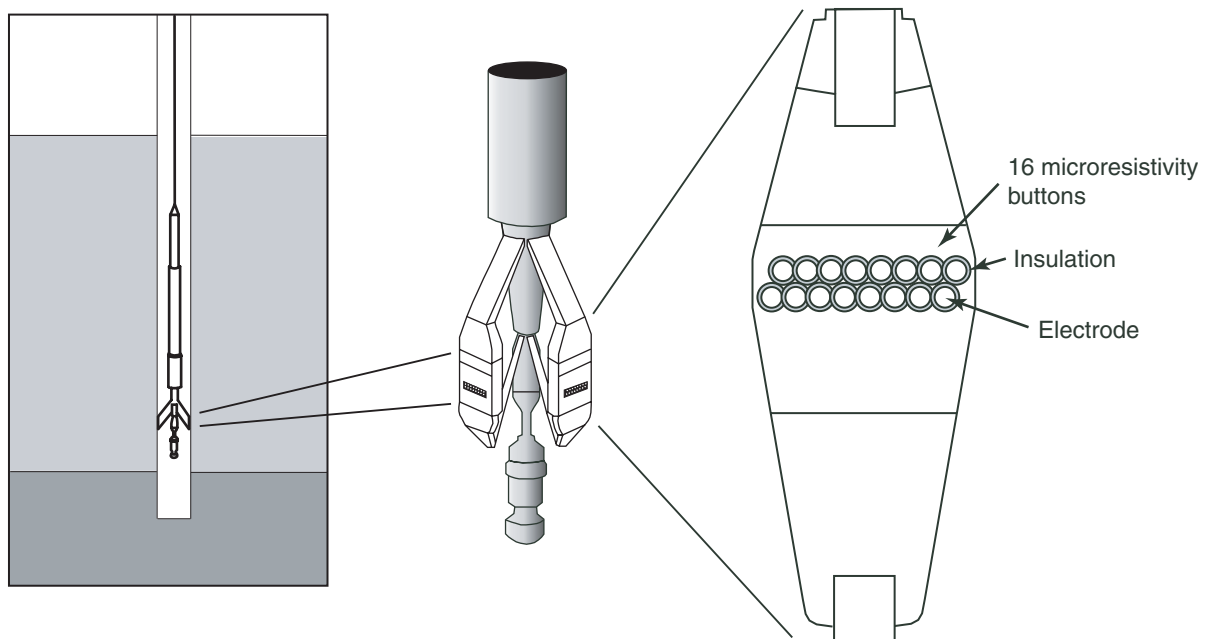
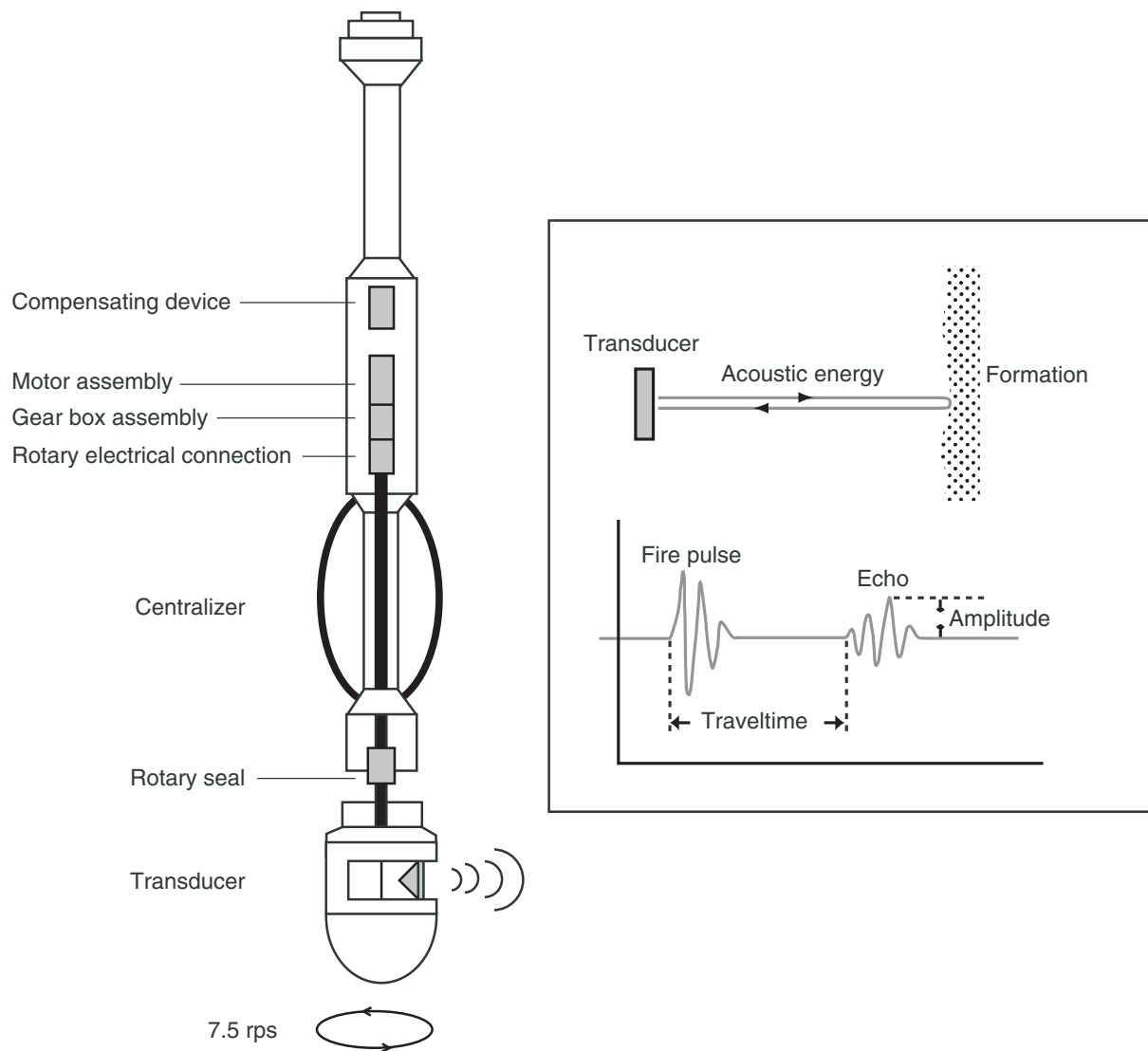


Figure F25. Schematic diagram of the Ultrasonic Borehole Imager.



**Figure F26.** Schematic diagram of the Goettingen Borehole Magnetometer. A/D = analog to digital. P/T = pressure/temperature.

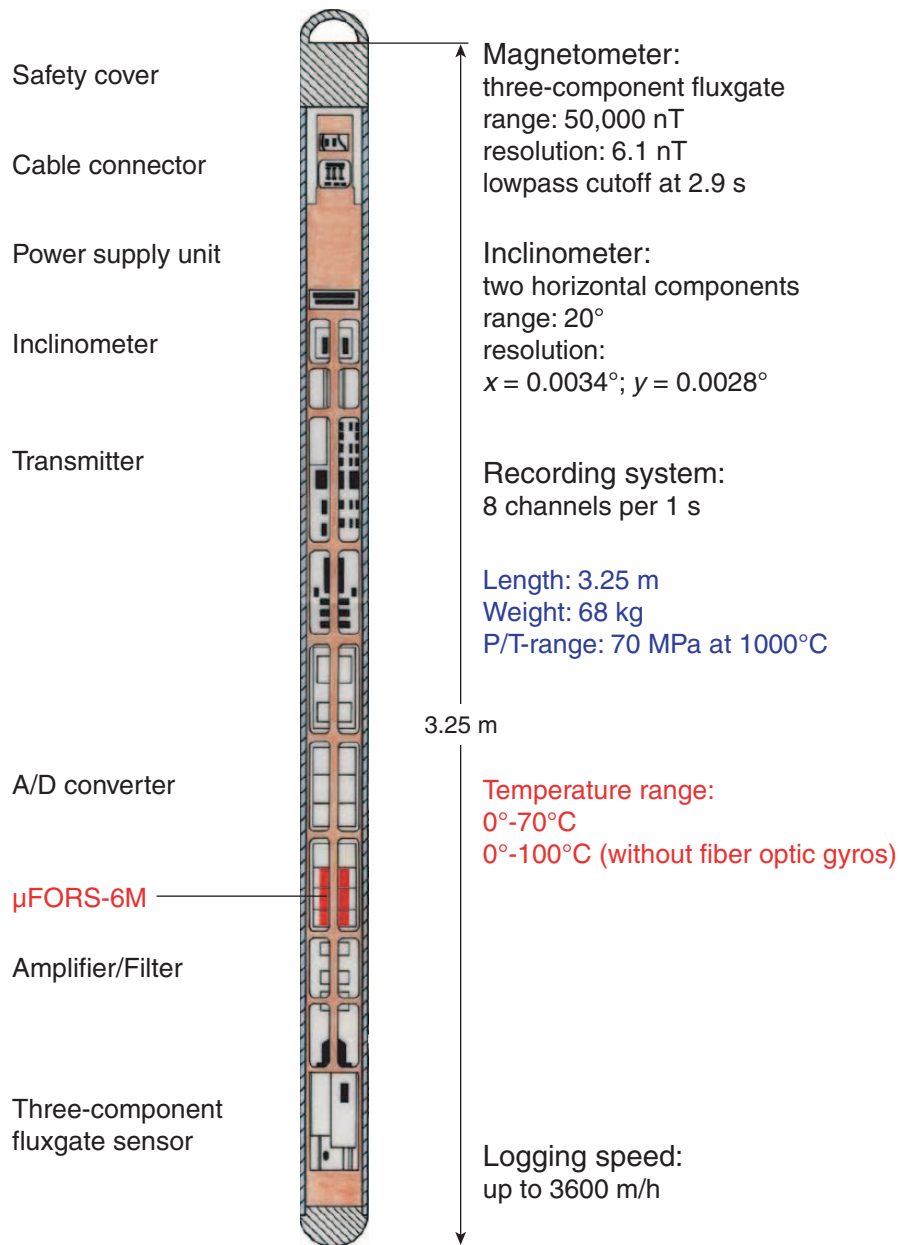


Table T1. Glossary of metamorphic petrology terms.

Term	Definition
Apparent fibers	Cross sections of serpentine plates that look fibrous in thin section.
Asbestiform	Crystals (chrysotile, tremolite) are thin hairlike fibers that are mechanically separable.
Background alteration	Alteration has pervasively affected the entire rock and is not primarily bound to veins or foliation planes.
Banded vein	Vein with rhythmic layering parallel to the vein walls.
Bastite	Serpentine texture after chain and layer silicates preserving important features of the protolith (e.g., plastic deformation) and preserpentine alteration assemblages.
Brucite	Brucite was tentatively identified by anomalous cream-brown interference colors, by yellow color in plane-polarized light (if weathered), and by shape (more bladed or prismatic than serpentine).
Chrysotile	White asbestiform serpentine, usually in veins with magnetite; most common in paragrular veins.
Composite vein	Compositionally zoned vein containing different mineral assemblages that may or may not represent different generations.
Cross-fiber vein	Asbestiform or pseudofibrous vein in which the fibers (or apparent fibers) are oriented perpendicular to the vein walls.
Fault vein	Vein material within a fault or cataclastic zone interpreted to be genetically related to the fault movement but lacking clear pull-apart geometries.
Fibrous	Single crystals resembling organic fibers or crystalline aggregates that look like they are composed of fibers. If fibers are mechanically separable (e.g., by probing the sample with a needle), they are asbestiform. If they are not separable, they are pseudofibrous. If the fibers have the normal strength and brittleness of the mineral, they are acicular.
Hourglass texture	Similar to mesh texture, but a distinction between mesh rim and mesh center is not possible. This texture is related to fractures in the mineral grains of the protolith and is, hence, not strictly a pseudomorph texture.
Interlocking texture	More or less equant serpentine grains and/or serrate serpentine veins replace pseudomorph serpentine.
Interpenetrating texture	Elongate, interpenetrating blades of $\gamma$ -serpentine replace pseudomorph serpentine.
Intravenous vein	Veins that are entirely or almost entirely restricted to the interior of previous veins, without penetrating the matrix. Generally referred to as composite if parallel to the previous veins.
Massive vein	Veins that are homogeneous and completely filled, with no identifiable internal texture.
Mesh texture	Pseudomorph texture resembling a fisherman's net. The mesh rim represents the cord of the net and the mesh centers represent the empty areas between the cords of the net. The outer edge of a mesh cell coincides either with the edge of a mineral grain or with a fracture within the mineral grain of the protolith.
Nonpseudomorph texture	Does not preserve the texture of the protolith. Can only be recognized under cross-polarized light. Includes interpenetrating and interlocking textures.
Patch	Polycrystalline domain, more or less isolated and surrounded by host rock, that is compositionally distinct from the host rock. Patches can be secondary features (i.e., as a consequence of patchy alteration) or primary igneous features where the differences may have been enhanced by alteration.
Picrolite	Vein-filling serpentine that is white, cream, or pale yellow to apple green in color and may be either massive or pseudofibrous in habit. Picrolite can be lizardite, chrysotile, or antigorite.
Polycrystalline vein	Vein clearly containing separate mineral grains. Can be mono- or polymineralic.
Pull-apart vein	Veins developed in extensional jogs on faults. Can be used to identify the direction of fault slip.
Pseudofibrous	Crystals or crystalline aggregates that have fibrous appearance but are not composed of separable fibers.
Pseudomorph texture	Preserves the texture of the protolith. Includes mesh and hourglass textures. Can be recognized in plane-polarized light.
Ribbon texture	Special form of transitional texture. Mesh rims extend over several grains of the protolith, creating a set of irregular bands.
Rodingite	A calcium metasomatized rock in which the primary igneous composition and texture have been destroyed to an extent that the nature of the protolith is uncertain. If the nature of the protolith can be discerned but calcium metasomatism is obvious, the rock is described as rodingitized.
Selvages	Wallrock along a vein that is completely altered to secondary minerals and has a sharp contact with the host rock.
Slip-fiber vein	Asbestiform or pseudofibrous vein in which the fibers (or apparent fibers) are oriented more or less parallel to the vein walls.
Transgranular vein	Vein or vein network at any angle to the foliation planes that crosscut porphyroclasts and/or other large crystals.
Transitional texture	Preserves some of the texture of the protolith. May appear pseudomorph in plane-polarized light but without mesh or hourglass texture in cross-polarized light. Includes mesh textures with isotropic mesh centers and ribbon textures.
Type 1 hourglass texture	Extinction sweeps continuously across mesh center.
Type 2 hourglass texture	Recrystallization of serpentine has produced a mottled extinction pattern.
Vein halos	Zones (1 mm–1 cm wide) along a vein in which the rock is more intensely altered, or altered in a different style, than the host rock. A halo can have a sharp or diffuse contact with the host rock.
Vuggy vein	Incompletely filled vein.
$\alpha$ -Serpentine	Length-fast fibers.
$\gamma$ -Serpentine	Length-slow fibers.

Table T2. Mineral abbreviations.

Minerals	
Ol	Olivine
Opx	Orthopyroxene
Cpx	Clinopyroxene
Spi	Spinel
Amph	Amphibole
Liz	Lizardite
Ant	Antigorite
Chry	Chrysotile
Srp	Serpentine (group)
Brc	Brucite
Trm	Tremolite
Act	Actinolite
Ath	Anthophyllite
Cum	Cumingtonite
Chl	Chlorite
Tlc	Talc
Mt	Magnetite
Sulf	Sulfides
Carb	Carbonates
Zeo	Zeolite (group)
Plag	Plagioclase
Preh	Prehnite
Qtz	Quartz
Ep	Epidote

Note: After Kretz (1983).

Table T3. Alteration codes used in the alteration log.

Code	Definition
Alteration mineral abundance:	
1	<1%
2	<10%
3	10%–50%
4	50%–90%
5	>90%
?	Tentative identification
Alteration assemblage:	
1	Serpentine
2	Talc/Tremolite/Chlorite
3	Greenschist facies mafic
4	Amphibolite facies mafic
5	Rodingite
6	Talc alteration
7	Low-grade alteration (clays, zeolites, etc.)
9	Other (described as comment)

Notes: Alteration mineral abundance is used in columns W to AI of the alteration log (see “[Supplementary material](#)”). Alteration assemblage is used in column L of the alteration log. See also % confidence column; a high degree of confidence normally indicates thin section observation.

**Table T4.** Vein types used in the vein log.

Type	Definition
Expedition 304:	
1	Hornblende/Dark amphibole
2	Green/Brown/Yellow actinolite veins, often brecciated, often with secondary plagioclase halos. Includes late magmatic leucocratic dikelets where affected by actinolite/secondary plagioclase alteration
3	Late actinolite $\pm$ chlorite, albite, sphene veins
4	Late veins/Fractures with clay minerals/Hydroxides/Zeolites
5	Carbonate veins
6	Tremolite veins in peridotite
7	Talc veins, sometimes with amphibole
8	Chrysotile/Serpentine veins. 8A denotes high aspect ratio veins; 8B denotes low aspect ratio veins
9	Composite talc/Tremolite veins
10	Quartz veins
11	Other (comment)
Expedition 305:	
1	Magmatic veins
2	Serpentinite veins
3	Dark green fibrous (rarely tabular) amphibole veins
4	Pale green amphibole veins, most with slip-fiber textures
5	White veins. These include carbonate, zeolite, anhydrite, prehnite, and, in the upper core, quartz veins
6	Clay rich veins. Clay (possibly saponite) commonly with calcite or zeolites (below 700 mbsf)

Note: Vein logs are found in [“Supplementary material.”](#)

**Table T5.** Structural identifier checklist used for spreadsheet comments associated with each structural identifier. (See [table notes](#). Continued on next page).

Structural identifier	Observations included
Subhorizontal microcracks (Shm)	Drilling-induced fractures
Joints (J)	Joint density Orientation Plume structures on joint surface
Veins (V)	Hydrothermal (Vh), fault with fibrous mineral (Vf), with cataclasis (Vc) Orientation of veins and vein-array boundaries Width and length Magnitude and nature of offset: n = normal, r = reverse, ss = strike slip Density of vein network (N/10 cm) Array characteristics Sense of shear: d = dextral, s = sinistral Angle between new vein segments and array boundary (measure of array dilatation) Internal structure of fibers Crack-seal structures and number of vein-opening events Wallrock alteration and shape—sharp or diffuse boundaries Vein terminations (splayed or tapered) Vein mineralogy Magmatic vein (Vm) Alteration vein (Va)
Faults (F)	Fault-zone thickness, orientation, and density Movement sense: r = reverse, n = normal, d = dextral, s = sinistral Movement offset (displacement, millimeters) Intensity of cataclastic fabric (Cf) Cataclastic foliation (Scc) Matrix material (gouge or secondary minerals) Overprinting of preexisting fabric Semibrittle

Table T5 (continued).

Structural identifier	Observations included
Breccias (B)	Hydrothermal (Bh), Magmatic (Bm), Cataclastic (Bc) Clast size and shape, matrix composition, relative proportions
Serpentinization foliation (S)	Strength of foliation Orientation of foliation in core reference frame
Brittle-plastic fabrics (Bp)	Intensity of fabric Orientation of foliation Intensity of fabric
Crystal-plastic fabrics (Cpf)	Intensity of fabric in retrograde assemblage Orientation of foliation (Sp) and lineation (Lp) L-, LS-, and S-tectonite Shear sense indicators: block-rotated porphyroclasts, asymmetric augen, SC fabrics, discrete shear bands, mica-fish, and tension gash arrays: r = reverse, n = normal, d = dextral, s = sinistral Mineralogical segregation or banding Intensity and orientation of foliations (Sm) and lineations (Lm)
Magmatic fabrics (Mf)	Minerals that define the shape and/or crystallographic preferred orientations Angle between crystallographic and shape fabrics Orientation of subfabrics
Compositional layering (Cl)	Type of layering (e.g., igneous cumulate, alteration, etc.); orientation, thickness, and density of layers Grain size layering (Gs), compositional "modal" layering (Cl) Orientation and density
Igneous contacts (Ic)	Concordant or discordant
Crosscutting relationships	Intrusive relationships, relative chronology of the different fabrics Angle between compositional layering and magmatic or crystal-plastic fabric

Notes: This checklist notes structural characteristics that were searched for in macroscopic core samples. These characteristics supplement the information required by the spreadsheet and were noted in the comments section of the spreadsheet. The abbreviations for these features were used to document crosscutting relationships on the structure section of the visual core descriptions.

Table T6. Microstructure of gabbroic rock.

Textural group	Plagioclase	Olivine	Pyroxene	Physical state
1	No or minor crystal-plastic deformation microstructures (e.g., deformation twins, undulose extinction)	No deformation microstructures ± local undulose extinction and/or local subgrain development	No deformation microstructures	Primarily magmatic
a	Random shape orientation			
b	Preferred shape orientation			
2	<30% fine-grained recrystallized matrix; deformation twins and subgrain boundaries may be present	Common subgrain boundaries and undulose extinction	No deformation microstructures ± minor crystal-plastic deformation microstructures	Crystal-plastic ± magmatic
3	>30% recrystallized matrix; deformation twins, subgrain boundaries, and undulose extinction common; moderate shape-preferred orientation; strong crystallographic-preferred orientation	Elongated aggregates of neoblasts	Kinked grains; common to extensive recrystallization	Crystal-plastic
4	Strongly bimodal grain size distribution; localized fine-grained neoblasts, polygonal neoblasts, sutured neoblasts	Closely spaced subgrain boundaries; pervasive undulose extinction; extensive neoblasts	Bent/kinked porphyroclasts; localized recrystallization	Crystal-plastic
5	Common intracrystalline microfractures associated with very fine grained neoblasts; extensive kinked and deformation twinned grains; pervasive undulose extinction; may contain hydrothermal alteration mineral assemblages	Same as plagioclase	Same as plagioclase	Semibrittle
6	Intra-/intercrystalline microfractures and cataclastic bands; extensive kinked and deformation twinned grains; pervasive undulose extinction	Same as plagioclase	Same as plagioclase	Brittle/Cataclastic

Table T7. Analytical conditions for ICP-AES analyses.

Element	Wavelength (nm)	Integration time per calculation point (s)	Photomultiplier voltage (V)	Photomultiplier gain	Increment between points (nm)	Number of calculation points	Limit of detection (ppm)
Al <sup>†</sup>	396.152	0.5	720	1	0.002	7	0.109
Ba	455.403	0.5	730	10	0.002	7	10
Ca <sup>†</sup>	393.366	0.5	350	1	0.002	7	0.084
Co	228.616	0.5	990	100	0.002	7	39
Cr	267.716	0.5	860	100	0.002	7	22
Cu	324.754	0.5	690	10	0.002	7	112
Fe <sup>†</sup>	259.940	0.5	560	10	0.002	7	0.328
K <sup>†</sup>	766.490	0.5	990	100	0.002	7	0.014
Mg <sup>†</sup>	285.213	0.5	600	10	0.002	7	0.220
Mn <sup>†</sup>	257.610	0.5	580	100	0.002	7	0.016
Na <sup>†</sup>	589.592	0.5	610	10	0.002	7	0.086
Ni	231.604	0.5	990	100	0.002	7	55
P <sup>†</sup>	178.229	0.5	990	100	0.002	7	0.143
Si <sup>†</sup>	251.611	0.5	570	10	0.002	7	0.522
Sr	407.771	0.5	560	10	0.002	7	2
V	292.402	0.5	960	100	0.002	7	3
Y	371.029	0.5	620	100	0.002	7	2
Zr	343.823	0.5	640	100	0.002	7	6
Ti <sup>†</sup>	334.941	0.5	570	10	0.002	7	0.021
Sc	361.384	0.5	660	100	0.002	7	1

Notes: ICP-AES = inductively coupled plasma-atomic emission spectrometry. † = Limit of detection reported as oxide weight percent. Detection limits of the instrument represent three times the instrumental blank (See “Analysis” in “ICP-AES analyses of major and trace elements”).

Table T8. Analytical reproducibility and accuracy of ICP-AES data during Expedition 304. (This table is available in an [oversized format](#).)

Table T9. Analytical reproducibility and accuracy of ICP-AES data during Expedition 305. (See table notes. Continued on next two pages.)

Standard	Date (2005)	Sample	Major element oxides (wt%)										Total
			SiO <sub>2</sub>	Al <sub>2</sub> O <sub>3</sub>	Fe <sub>2</sub> O <sub>3</sub>	MgO	MnO	CaO	Na <sub>2</sub> O	K <sub>2</sub> O	P <sub>2</sub> O <sub>5</sub>	TiO <sub>2</sub>	
DTS-1	23 Jan	1	40.83	0.18	8.74	48.10	0.12	0.10	BDL	BDL	BDL	BDL	98.08
		2	41.23	0.19	8.39	50.62	0.12	0.10	BDL	BDL	BDL	BDL	100.64
	25 Jan	1	39.77	0.18	8.67	49.74	0.12	0.09	BDL	BDL	BDL	BDL	98.61
		2	40.22	0.18	9.51	50.50	0.11	0.09	BDL	BDL	BDL	BDL	100.67
	27 Jan	1	39.51	0.28	8.34	51.33	0.12	0.11	BDL	BDL	BDL	BDL	99.70
		2	39.85	0.20	8.32	47.36	0.11	0.10	BDL	BDL	BDL	BDL	96.01
	30 Jan	1	40.27	0.15	8.52	48.29	0.12	0.08	BDL	BDL	BDL	BDL	97.48
		2	40.14	0.20	8.49	49.86	0.12	0.12	BDL	BDL	BDL	BDL	98.95
	2 Feb	1	41.65	0.17	8.76	49.62	0.12	0.07	BDL	BDL	BDL	BDL	100.41
		2	41.10	0.18	8.51	49.20	0.12	0.08	BDL	BDL	BDL	BDL	99.22
	3 Feb	1	40.91	0.18	8.64	50.51	0.12	0.07	BDL	BDL	BDL	BDL	100.42
		2	40.46	0.18	8.67	49.60	0.12	0.07	BDL	BDL	BDL	BDL	99.11
	9 Feb	1	41.64	0.19	8.57	50.78	0.12	0.10	BDL	BDL	BDL	BDL	101.45
		2	40.64	0.18	8.50	49.70	0.11	0.10	BDL	BDL	BDL	BDL	99.28
	11 Feb	1	40.39	0.17	8.78	49.59	0.12	0.08	BDL	BDL	BDL	BDL	99.16
		2	39.91	0.18	8.54	48.11	0.12	0.08	BDL	BDL	BDL	BDL	96.95
	13 Feb	1	40.27	0.19	8.51	48.99	0.12	0.06	BDL	BDL	BDL	BDL	98.18
		2	39.48	0.18	8.33	49.01	0.12	0.05	BDL	BDL	BDL	BDL	97.18
	15 Feb	1	40.74	0.19	8.78	49.39	0.12	0.07	BDL	BDL	BDL	BDL	99.29
		2	39.92	0.19	8.50	49.74	0.12	0.07	BDL	BDL	BDL	BDL	98.54
17 Feb	1	40.01	0.19	8.50	49.60	0.12	0.10	BDL	BDL	BDL	BDL	98.60	
	2	39.45	0.19	8.52	48.49	0.12	0.10	BDL	BDL	BDL	BDL	96.95	
	Averages:	40.38	0.18	8.60	49.46	0.12	0.09	BDL	BDL	BDL	BDL	98.86	
	Certified values:	40.74	0.19	8.75	50.00	0.12	0.17	0.01	0.01	0.00	0.01	100.00	
	Precision:	0.64	0.01	0.25	0.94	0.00	0.02	—	—	—	—	—	
		1.58%	5.4%	2.9%	1.9%	3.1%	10.7%	—	—	—	—	—	
	Accuracy:	0.36	0.01	0.15	0.54	0.00	0.09	—	—	—	—	—	
		0.88%	4.6%	1.8%	1.1%	1.7%	49.9%	—	—	—	—	—	
JGb-1	23 Jan	1	41.87	18.22	15.18	8.31	0.19	11.88	1.23	0.23	BDL	1.51	98.67
		2	46.29	18.23	15.89	8.08	0.19	11.55	1.24	0.23	BDL	1.60	103.34
	25 Jan	1	45.01	17.46	13.66	7.58	0.20	11.85	1.28	0.22	BDL	1.59	98.93
		2	45.03	19.31	17.35	7.62	0.19	10.24	1.40	0.45	BDL	1.76	103.43
	27 Jan	1	44.59	17.69	14.87	8.36	0.20	12.03	1.24	0.23	BDL	1.57	100.82
		2	46.45	18.03	16.05	8.22	0.20	11.78	1.25	0.24	BDL	1.65	103.89
	30 Jan	1	44.43	18.10	15.98	8.05	0.19	11.92	1.25	0.24	BDL	1.61	101.80
		2	44.53	17.61	15.34	8.18	0.19	11.85	1.23	0.23	BDL	1.59	100.79
	3 Feb	1	44.01	17.43	15.77	7.94	0.19	12.25	1.27	0.24	BDL	1.60	100.71
		Averages:	44.07	17.75	15.13	8.07	0.19	11.96	1.25	0.23	BDL	1.58	100.29
		Certified values:	43.66	17.49	15.06	7.85	0.19	11.90	1.20	0.24	0.06	1.60	100.00
		Precision:	1.13	0.33	0.82	0.29	0.00	0.16	0.02	0.01	—	0.04	1.22
			2.58%	1.9%	5.5%	3.7%	2.0%	1.3%	1.7%	2.2%	—	2.4%	1.2%
		Accuracy:	-0.41	-0.26	-0.07	-0.22	-0.01	-0.06	-0.05	0.01	—	0.02	-0.29
		-0.9%	-1.5%	-0.5%	-2.8%	-3.0%	-0.5%	-4.2%	3.5%	—	1.3%	-0.3%	
JB-3	10 Feb	1											
		2											
	11 Feb	1	51.17	17.00	11.61	5.15	0.18	9.48	2.76	0.76	0.36	1.38	99.86
		2	48.46	16.99	11.99	5.16	0.18	9.87	2.76	0.79	0.31	1.40	97.92
	13 Feb	1	50.95	16.75	11.66	5.21	0.18	9.83	2.70	0.75	0.51	1.40	99.94
		2	51.16	16.73	11.78	5.07	0.18	9.77	2.75	0.75	0.46	1.40	100.05
	15 Feb	1	51.50	17.30	11.68	5.18	0.18	9.77	2.72	0.77	0.24	1.42	100.75
		2	50.75	16.81	11.53	5.21	0.18	9.69	2.71	0.78	0.32	1.45	99.44
	17 Feb	1	50.44	17.38	11.70	5.22	0.18	9.39	2.79	0.76	0.44	1.34	99.64
		2	49.49	16.65	11.94	5.04	0.18	9.72	2.76	0.77	0.42	1.44	98.42
		Averages:	50.49	16.95	11.74	5.15	0.18	9.69	2.74	0.77	0.38	1.40	99.50
		Certified values:	50.96	17.20	11.82	5.19	0.18	9.79	2.73	0.78	0.29	1.44	100.00
		Precision:	1.03	0.27	0.16	0.07	0.00	0.17	0.03	0.01	0.09	0.03	0.92
			2.01%	1.6%	1.3%	1.3%	1.4%	1.7%	1.1%	1.7%	30.5%	2.3%	0.9%
	Accuracy:	0.47	0.25	0.08	0.04	0.00	0.10	-0.01	0.01	-0.09	0.04	0.50	
		0.92%	1.4%	0.7%	0.7%	-1.6%	1.0%	-0.5%	1.8%	-30.6%	2.6%	0.5%	
305-U1309D-171R-4,18-30 cm	23 Jan	1	52.66	16.75	5.33	8.36	0.10	14.00	2.63	0.03	0.03	0.52	100.40
		2	52.31	16.79	5.33	8.16	0.10	13.90	2.64	0.03	0.04	0.52	99.82
		3	51.57	16.77	5.36	8.34	0.11	14.02	2.66	0.03	0.02	0.48	99.34
		Averages:	52.18	16.77	5.34	8.28	0.10	13.97	2.64	0.03	0.03	0.51	99.85
		Precision:	0.56	0.02	0.02	0.11	0.00	0.07	0.01	0.00	0.01	0.02	0.53
		1.07%	0.1%	0.3%	1.3%	1.2%	0.5%	0.5%	1.3%	39.5%	4.5%	0.5%	

Table T9 (continued).

Standard	Date (2005)	Sample	Trace elements (ppm)										
			Y	Ba	Cr	Ni	Sc	Co	Sr	Cu	V	Zr	
DTS-1	23 Jan	1	BDL	BDL	4059	2175	3.51	124	BDL	BDL	BDL	BDL	
		2	BDL	BDL	4059	2272	3.39	122	BDL	BDL	BDL	BDL	
	25 Jan	1	BDL	BDL	3503	2284	3.80	134	BDL	BDL	BDL	BDL	
		2	BDL	BDL	3495	2206	3.66	124	BDL	BDL	BDL	BDL	
	27 Jan	1	BDL	BDL	3688	2323	3.36	131	BDL	BDL	BDL	BDL	
		2	BDL	BDL	3613	2233	3.64	130	BDL	BDL	BDL	BDL	
	30 Jan	1	BDL	BDL	3653	2372	3.59	151	BDL	BDL	BDL	BDL	
		2	BDL	BDL	3582	2353	3.56	109	BDL	BDL	BDL	BDL	
	2 Feb	1	BDL	BDL	3659	2431	3.20	129	BDL	BDL	BDL	BDL	
		2	BDL	BDL	3582	2381	3.22	137	BDL	BDL	BDL	BDL	
	3 Feb	1	BDL	BDL	3662	2312	3.52	128	BDL	BDL	BDL	BDL	
		2	BDL	BDL	3602	2336	3.47	125	BDL	BDL	BDL	BDL	
	9 Feb	1	BDL	BDL	3814	2361	3.47	115	BDL	BDL	BDL	BDL	
		2	BDL	BDL	3876	2374	3.70	108	BDL	BDL	BDL	BDL	
	11 Feb	1	BDL	BDL	3709	2507	3.67	126	BDL	BDL	BDL	BDL	
		2	BDL	BDL	3707	2398	3.72	121	BDL	BDL	BDL	BDL	
	13 Feb	1	BDL	BDL	3724	2329	3.34	126	BDL	BDL	BDL	BDL	
		2	BDL	BDL	3729	2285	3.63	119	BDL	BDL	BDL	BDL	
	15 Feb	1	BDL	BDL	3817	2442	3.51	129	BDL	BDL	BDL	BDL	
		2	BDL	BDL	3743	2349	3.43	124	BDL	BDL	BDL	BDL	
17 Feb	1	BDL	BDL	3683	2291	3.60	128	BDL	BDL	BDL	BDL		
	2	BDL	BDL	3558	2339	3.41	125	BDL	BDL	BDL	BDL		
	Averages:		BDL	BDL	3705	2334	3.52	126	BDL	BDL	BDL	BDL	
	Certified values:		0.04	1.70	3990	2360	3.50	140	0.32	7.10	11.00	4.00	
	Precision:		—	—	149.59	76.94	0.16	8.95	—	—	—	—	
			—	—	3.75%	3.26%	4.49%	6.39%	—	—	—	—	
	Accuracy:		—	—	284.68	25.89	-0.02	14.29	—	—	—	—	
			—	—	7.13%	1.10%	-0.53%	10.21%	—	—	—	—	
JGb-1	23 Jan	1	9.70	63.9	37.2	BDL	37.60	63.4	326.7	83.9	672.2	26.2	
		2	9.31	66.5	39.6	BDL	36.09	62.0	325.3	80.1	659.4	26.6	
	25 Jan	1	10.21	66.8	52.3	BDL	36.71	72.0	344.2	84.8	620.9	31.2	
		2	10.71	71.4	47.9	BDL	36.10	64.9	359.2	81.1	625.1	27.4	
	27 Jan	1	11.00	67.5	48.9	BDL	36.21	73.2	339.3	86.5	618.0	25.7	
		2	10.67	66.6	45.3	BDL	36.25	73.6	333.4	85.5	643.6	27.7	
	30 Jan	1	10.42	66.3	46.1	BDL	36.73	63.0	330.8	81.8	641.6	29.6	
		2	10.45	67.9	50.4	BDL	36.15	51.2	336.1	86.4	643.2	29.7	
	3 Feb	1	10.70	67.6	53.3	BDL	34.50	69.5	352.7	88.7	638.8	30.3	
		Averages:		10.35	67.2	46.8	BDL	36.26	65.9	338.6	84.3	640.3	28.3
		Certified values:		10.40	64.3	57.8	25.40	35.80	60.1	327.0	85.7	635.0	32.8
		Precision:		0.54	1.97	5.44	—	0.82	7.15	11.55	2.85	17.70	1.97
				5.2%	3.1%	9.4%	—	2.3%	11.9%	3.5%	3.3%	2.8%	6.0%
		Accuracy:		0.05	-2.85	11.01	—	-0.46	-5.78	-11.64	1.37	-5.32	4.52
			0.5%	-4.4%	19.0%	—	-1.3%	-9.6%	-3.6%	1.6%	-0.8%	13.8%	
JB-3	10 Feb	1	27.49	240.4	51.0	BDL	33.90	39.4	428.2	225.1	368.7	93.9	
		2	28.17	231.1	55.5	BDL	34.92	40.0	425.5	222.5	383.8	91.9	
	11 Feb	1	27.40	238.6	54.2	BDL	35.45	44.3	380.2	207.7	378.9	96.3	
		2	26.08	236.3	58.2	BDL	34.53	43.0	388.1	180.4	378.1	94.1	
	13 Feb	1	27.02	242.0	50.0	BDL	35.50	46.6	410.1	226.2	376.1	97.6	
		2	27.25	239.9	52.8	BDL	33.98	43.8	405.0	213.2	368.5	94.5	
	15 Feb	1	27.77	242.1	57.0	BDL	34.04	40.9	405.3	206.0	368.0	94.9	
		2	28.05	243.0	54.3	BDL	34.87	44.1	410.7	219.2	373.9	101.4	
	17 Feb	1	26.19	241.9	57.2	BDL	35.19	50.2	415.1	223.3	377.3	92.7	
		2	28.62	244.8	58.1	BDL	34.68	44.9	403.2	227.5	367.7	90.2	
		Averages:		27.41	240.0	54.8	BDL	34.70	43.7	407.1	215.1	374.1	94.8
		Certified values:		26.90	245.0	58.1	36.20	33.80	34.3	403.0	194.0	372.0	97.8
		Precision:		0.82	3.92	2.90	—	0.59	3.22	14.82	14.37	5.67	3.13
				3.0%	1.6%	5.0%	—	1.8%	9.4%	3.7%	7.4%	1.5%	3.2%
	Accuracy:		-0.51	4.98	3.27	—	-0.90	-9.40	-4.14	-21.11	-2.07	3.05	
			-1.9%	2.0%	5.6%	—	-2.7%	-27.4%	-1.0%	-10.9%	-0.6%	3.1%	
305-U1309D-171R-4,18-30 cm													
	23 Jan	1	12.40	BDL	114.25	64.07	40.82	20.42	93.64	BDL	183.70	BDL	
		2	12.19	BDL	118.26	76.57	45.16	26.54	99.35	BDL	196.04	BDL	
		3	12.51	BDL	125.44	67.97	45.12	30.72	97.88	BDL	201.64	BDL	
	Averages:		12.36	BDL	119.32	69.54	43.70	25.89	96.96	BDL	193.79	BDL	
	Precision:		0.16	—	5.67	6.40	2.50	5.18	2.97	—	9.18	—	
			1.3%	—	4.8%	9.2%	5.7%	20.0%	3.1%	—	4.7%	—	

Table T9 (continued).

Notes: All runs completed on the Meinhart nebulizer. JB-3, JGb-1, DTS-1, GSJ-2003, and USGS-2003 are international rock reference materials and samples. — = not applicable. BDL = below detection limit.

Table T10. Analytical reproducibility and accuracy of volatile analyses, Expedition 304.

Standard	Date	Sample	Average		Standard deviation		
			CO <sub>2</sub>	H <sub>2</sub> O	CO <sub>2</sub>	H <sub>2</sub> O	
JP-1	26 Nov 2004	1	0.29	2.48	0.011	0.298	
	3 Dec 2004	1	0.31	2.27	0.004	0.032	
	4 Dec 2004	1	0.28	2.65	0.007	0.024	
	11 Dec 2004	1	0.30	2.42	0.009	0.076	
	12 Dec 2004	1	0.23	2.29	0.024	0.140	
	14 Dec 2004	1	0.30	2.18	0.009	0.029	
		2	0.32	2.80	0.058	0.406	
	16 Dec 2004	1	0.26	2.00	0.006	0.072	
	23 Dec 2004	1	0.29	2.40	0.008	0.186	
	26 Dec 2004	1	0.29	2.12	0.011	0.079	
	28 Dec 2004	1	0.28	2.22	0.010	0.028	
	29 Dec 2004	1	0.27	2.44	0.004	0.127	
	31 Dec 2004	1	0.31	2.29	0.009	0.029	
	1 Jan 2005	1	0.30	2.32	0.000	0.065	
	3 Jan 2005	1	0.30	2.56	0.016	0.125	
	4 Jan 2005	1	0.28	2.57	0.004	0.226	
		Averages:		0.29	2.38		
		Certified values:		0.28	2.39		
		Standard deviation:		0.02	0.21		
		Precision:		7.58%	8.67%		
	Accuracy:		2.91%	-0.60%			
BAS-140	26 Nov 2004	1	0.10	0.87	0.009	0.090	
	3 Dec 2004	1	0.10	0.76	0.016	0.124	
	4 Dec 2004	1	0.08	0.94	0.012	0.075	
	11 Dec 2004	1	0.10	0.66	0.003	0.096	
	12 Dec 2004	1	0.02	0.88	0.008	0.446	
	14 Dec 2004	1	0.13	0.61	0.033	0.045	
		2	0.10	0.84	0.006	0.021	
	16 Dec 2004	1	0.08	0.72	0.018	0.047	
	23 Dec 2004	1	0.10	0.87	0.006	0.090	
	26 Dec 2004	1	0.09	0.71	0.000	0.150	
	28 Dec 2004	1	0.09	0.98	0.009	0.124	
	29 Dec 2004	1	0.09	0.93	0.014	0.012	
	31 Dec 2004	1	0.11	0.78	0.017	0.060	
	1 Jan 2005	1	0.10	0.83	0.006	0.083	
	3 Jan 2005	1	0.09	0.75	0.003	0.079	
	4 Jan 2005	1	0.08	0.91	0.006	0.000	
		Averages:		0.09	0.81		
		Certified values:		0.05	1.12		
		Standard deviation:		0.02	0.11		
		Precision:		23.58%	13.01%		
	Accuracy:		45.28%	-37.46%			

Table T11. MST sampling intervals.

Measurement	Magnetic susceptibility	Noncontact resistivity	Natural gamma radiation
Sampling period (s)	—	—	30
Data acquisitions (N)	3	3	—
Sampling interval (cm)	2	2	10

Note: Time for section processing = 18 min, 56 s.

**Table T12.** Noncontact resistivity, Sections 305-U1309D-38R-2 to 38R-3.

	0.25 h after arrival on deck		2.7 h after arrival on deck		Difference	
	V	$\Omega\cdot\text{m}$	V	$\Omega\cdot\text{m}$	V	$\Omega\cdot\text{m}$
Mean	0.0136	11.4	0.0079	27.4	-0.0057	16.0
Standard deviation	0.0037	5.6	0.0034	36.5	-0.0003	30.9

**Table T13.** Measurements made by wireline tool strings.

Tool string	Tool	Measurement	Sampling interval (cm)	Approximate vertical resolution (cm)
Triple combination	HNGS	Spectral gamma ray	15	51
	APS	Porosity	5 and 15	43
	HLDS	Bulk density	2.5 and 15	46
	DLL	Resistivity	15	61
	TAP	Temperature	1 per s	NA
	TAP	Tool acceleration	4 per s	NA
Formation MicroScanner (FMS)-sonic combination		Pressure	1 per s	NA
	FMS	Microresistivity	0.25	0.5
	GPIT	Tool orientation	0.25 and 15	NA
	SGT	Total gamma ray	15	NA
Ultrasonic Borehole Imager	DSI	Acoustic velocity	15	107
	UBI	Ultrasonic imaging	Variable	0.5–2
	GPIT	Tool orientation	0.25 and 15	NA
WST-3	SGT	Total gamma ray	15	NA
WST-3	WST-3	Sonic travelttime	NA	NA
Goettingen Borehole Magnetometer	GBM	Magnetic field	5	NA
		Tool orientation		

Notes: All tool and tool string names (except the TAP and GBM) are trademarks of Schlumberger. For the complete list of acronyms used in IODP and for additional information about tool physics and use consult IODP-USIO Science Services, LDEO, at [iodp.ldeo.columbia.edu/TOOLS\\_LABS/tools.html](http://iodp.ldeo.columbia.edu/TOOLS_LABS/tools.html). See Table T14 for explanation of acronyms used to describe tool string and tools. NA = not applicable.

Table T14. Acronyms and units used for wireline logging tools.

Tool	Output	Tool name/Explanation of output	Unit
APS	APLC	Accelerator Porosity Sonde Near array porosity (limestone calibrated)	%
	SIGF	Formation capture cross section ( $\Sigma_p$ )	Capture units
	STOF	Tool standoff (computed distance from borehole wall)	in
DLL	LLD	Dual Laterolog Deep resistivity	$\Omega m$
	LLS	Shallow resistivity	$\Omega m$
DSI	DTCO	Dipole Sonic Imager Compressional wave delay time ( $\Delta t$ )	ms/ft
	DTSM	Shear wave delay time ( $\Delta t$ )	ms/ft
	DTST	Stoneley wave delay time ( $\Delta t$ )	ms/ft
FMS	C1, C2	Formation MicroScanner Orthogonal hole diameters	in
	PIAZ	Pad 1 azimuth	Degrees
		Spatially oriented resistivity images of borehole wall	
GPIT	DEVI	General Purpose Inclinerometer Tool Hole deviation	Degrees
	HAZI	Hole azimuth	Degrees
	$F_x, F_y, F_z$	Earth's magnetic field (three orthogonal components)	Oersted
	$A_x, A_y, A_z$	Acceleration (three orthogonal components)	$m/s^2$
HLDS	RHOM	Hostile Environment Litho-Density Sonde Bulk density (corrected)	$g/cm^3$
	PEFL	Photoelectric effect	b/e <sup>-</sup>
	LCAL	Caliper (measure of borehole diameter)	in
	DRHO	Bulk density correction	$g/cm^3$
HNGS	HSGR	Hostile Environment Gamma Ray Sonde Standard (total) gamma ray	gAPI
	HCGR	Computed gamma ray (HSGR minus uranium contribution)	gAPI
	HFK	Potassium	wt%
	HTHO	Thorium	ppm
	HURA	Uranium	ppm
SGT	ECGR	Scintillation Gamma Ray Tool Environmentally corrected gamma ray	gAPI
TAP	Temperature/Acceleration/Pressure tool	$^{\circ}C, m/s^2, psi$	
UBI		Ultrasonic Borehole Imager Spatially oriented acoustic images of borehole wall	
		Acoustic arrival times and amplitude	ms
		Borehole diameter	in
		Borehole azimuth	Degrees
WST-3		Three-component Well Seismic Tool Acoustic arrival time	ms
GBM	$F_x, F_y, F_z$	Goettingen Borehole Magnetometer Earth's magnetic field (three orthogonal components)	nT
	$N_x, N_y$	Inclination	Degrees
	T1, T2	Telemetry and gyro temperature	$^{\circ}C$